Dissertation zur Erlangung des Doktorgrades der Fakultät
für Chemie und Pharmazie der
Ludwig-Maximilians-Universität München

Simultaneous dual-color 3D stimulated emission depletion microscopy: from design to applications

Christian Osseforth

aus

München, Deutschland

2014

Erklärung

Diese Dissertation wurde im Sinne von § 7 der Promotionsordnung vom 28. November 2011 von Herrn Prof. Dr. Jens Michaelis betreut.

Eidesstattliche Versicherung

Diese Dissertation wurde eigenständig und ohne unerlaubte Hilfe erarbeitet.

München, den .....

(Christian Osseforth)

Dissertation eingereicht am:	26.09.2014
1. Gutachter:	Prof. Dr. Jens Michaelis
2. Gutachter:	Prof. Dr. Christof Gebhardt
Mündliche Prüfung am:	28.10.2014

Abstract

Super-resolution imaging, the ability to resolve structures well below the diffraction limit, has changed fluorescence microscopy as we know it. Diffraction-unlimited microscopy, termed nanoscopy, is able to image deep inside the cell with a resolution approaching that of electron microscopes. A variety of different methods currently exist, the first proposed and demonstrated technique being stimulated emission depletion (STED) microscopy. In STED microscopy, the resolution limit of a laser scanning microscope is overcome by transiently silencing fluorescence in parts of the focus. Practical implementations of this method are limited by optical aberrations and the characteristics of the fluorophores used. In this thesis, I present a fully working, custom built, 3D dual-color STED microscope. A super-continuum source is used to provide all spectral bands necessary for excitation and efficient depletion to achieve a lateral and axial resolution of $\sim$ 35 nm and $\sim$ 90 nm, respectively. I characterize the system's performance by imaging colloidal particles and single fluorescent molecules. Its biological applicability is demonstrated by imaging of nuclear pore complexes in U2OS and yeast cells, replication complexes in C2C12 cells, C2 toxin component C2I in HeLa cells and scaffold proteins in chemical synapses of hippocampal neurons. Advice on how to build such a microscope is given in the appendix. In addition, a theory is presented which demonstrates that the resolution of STED microscopes can be further enhanced by using the arrival time of spontaneous emission by time-gating the detection.

Contents

Chapter 1

Introduction

Ever since the first scientific publication by Robert Hooke depicting a microorganism as viewed through the first light microscope [Hooke, 1665], microscopy grew to be an important tool in the life sciences [Gest, 2004]. It became clear at the end of the 19th century that the resolution of conventional light microscopes cannot be improved indefinitely simply by manufacturing better lenses [Ernst Abbe, 1873]. The wave nature of light itself sets the limit in resolution of a classical microscope, the so-called diffraction limit:

$$d \approx \frac{\lambda}{2\,n\,sin\alpha} \tag{1.1}$$

where d is the achievable resolution in terms of the minimum distance between two lines in a grid at which they are still resolvable as individual lines. λ denotes the wavelength of the light used, n the index of refraction of the immersion medium and α the half opening angle of the objective lens. The term $n\,sin\alpha$ is also called the numerical aperture (NA) of the objective lens used. From Abbe's insight it becomes apparent that to increase resolution, the wavelength needs to be decreased and/or the numerical aperture increased. The theoretical maximal opening angle of the objective lens is limited to 180° yielding a $sin\alpha$ of 1 (for an indefinitely large lens). To increase the NA the refractive index of the immersion medium is maximized to match that of the glass used. Thus, high-end oil immersion objective lenses typically have a NA of 1.4 whereas water-immersion and air-immersion ob-

jectives have a NA of typically 1.3 and 0.9, respectively. As a result, the only viable parameter to tune the achievable resolution in classical microscopy is the wavelength[1]. However, this also poses numerous technical problems such as the high energy of short wavelength radiation and the limited spectral sensitivity of the human eye and cameras.

A milestone in the development of more powerful microscopes was the invention of the electron microscope [Knoll and Ruska, 1932, Knott and Genoud, 2013]. Due to the shorter wavelength of the electron beam in the range of picometers, its resolution greatly surpasses that of conventional light microscopes while still being limited by diffraction. However, especially for biological samples, electron microscopy has its drawbacks. Imaging is done in vacuum thus precluding live cell microscopy. Furthermore, the specific and quantitative staining of proteins of interest utilizing gold nanoparticles remains a challenge in electron-dense material such as the postsynaptic density in chemical synapses.

In 1957 Marvin Lee Minsky filed a patent on a light microscope design which greatly reduced the problem of scattered light deteriorating image quality in light microscopy, the confocal microscope [Marvin Lee Minsky, 1961]. It was not, however, until the 1980's that this design really had an impact on the life sciences [Amos and White, 2003]. The concomitant increase in fluorescence imaging at the end of the 1970's using specific labeled antibodies is brought forth as one reason for the delayed impact of the confocal fluorescence microscope in life sciences [Amos and White, 2003, Masters, 2001]. Nowadays, confocal laser scanning microscopes are found in labs throughout the world. The technique has emerged as a standard tool in cell biology. However, many biological structures remain smaller than the resolution of ~ 250 nm achievable with confocal fluorescence microscopes - the diffraction limit is not overcome by this technique.

In the mid-1990's Stefan Hell first proposed an approach named stimulated emission depletion (STED) microscopy on how to fundamentally break

[1] Additionally, the effective NA of a microscope - and thus its resolution - can be further increased beyond that of the common single objective lens implementation by using two objective lenses in a 4π configuration. For details see Section 2.5.3 and 5.2.4

the diffraction limit by stimulated emission [Hell and Wichmann, 1994]. Experimentally, the feasibility of STED microscopy was first demonstrated in 1999 [Klar and Hell, 1999]. Breaking the diffraction limit in the far-field as opposed to near-field approaches such as near-field scanning optical microscopy [Dickenson et al., 2010, Pohl et al., 1984] has sparked many new developments especially in biology as the technique is not limited to surfaces but can image deep down into tissue. Since these early days of so called super-resolution fluorescence microscopy further methods have been implemented using switching of single molecules to yield sub-diffraction images such as stochastic optical reconstruction microscopy (STORM, [Rust et al., 2006]) and photoactivated localization microscopy (PALM, [Betzig et al., 2006]) to name but a few (also see [van Oijen et al., 1998]). All these novel approaches are not fundamentally limited to imaging fixed samples in stark contrast to electron microscopy.

The advent of diffraction-unlimited fluorescence microscopy will undoubtedly revolutionize the field of biological microscopy. Improvements and variations of the original ideas are being published at a considerable rate underlining the importance of this novel field. The initially proposed designs have been successfully commercialized and are expected to find rapid use in laboratories throughout the world.

While early STED microscopes were rather complex and utilized expensive laser systems, novel super-continuum laser sources were recently shown to be a promising alternative [Wildanger et al., 2008]. This approach sparked our interest in setting up such a system in the lab due to reduced cost, flexibility in terms of suitable fluorophores and a better temporal stability through inherently synchronized pulses. A first version was soon built but lacked applicability to real biological questions as it could only detect one fluorescent species and had an improvement in resolution only in the sample plane similar to other published experiments by the group of Stefan Hell. It became evident during initial experiments that questions regarding localization of proteins of interest in a cellular environment are best answered when related to the position of known structures. To this end, the microscope was extended to provide super-resolution imaging in two channels simultaneously

while still using the same super-continuum laser source. This version greatly expanded its use and was successfully used to image a variety of epitopes in the nuclear pore complexes.

In the complex setting of a three-dimensional object such as a cell, the diffraction unlimited imaging in two dimensions as achieved with dual-color STED microscopy already constitutes a vast improvement over conventional confocal microscopy. However, the great disparity in resolution in the lateral and axial dimension creates artifacts when imaging three-dimensional structures. The low axial resolution sets the practical limit of resolving structures. To resolve this issue and make full use of the enhanced resolution the setup was further expanded to yield super-resolution imaging also along the optical axis. The design and implementation of the current version of the microscope featuring super-resolution imaging down to $\sim$ 35 nm laterally and 90 nm axially is described in detail in Chapter 4. Practical instructions on how to build and align the microscope are given in the appendix section along with a description of important hard- and software components.

This microscope was then used to image a variety of different objects including nuclear pore complexes in U2OS and yeast cells, replication complexes in C2C12 cells, C2 toxin component C2I in HeLa cells, scaffold proteins in chemical synapses of hippocampal neurons as well as non-biological nanoparticles (Chapter 5). Specifically, the ability to resolve nanoparticles 100 nm in diameter was utilized to successfully validate an absolute quantification algorithm based on fluorescence intensity in a diffraction limited confocal microscope (Section 5.1). Moreover, nuclear pore complexes serve as viable test samples to visualize the strong disparity in resolution when imaging in 2D mode and helps to explain the artifacts that come along with it. When the structure of interest is correctly oriented along the dimension of best resolution, two epitopes targeted by the same type of antibody can be resolved (Section 5.2). Three-dimensional imaging (z-stack recording) was performed in C2C12 myoblast cells resolving replication sites of nanometer dimension in 3D, thus emphasizing the need for 3D super-resolution techniques when imaging three-dimensional samples. Further experiments were designed to test the sensitivity of the microscope, both *in vitro* and of ob-

jects within a cellular environment. To this end, immobilized DNA molecules labeled with single chromophores were imaged as well as nuclear pore complexes in yeast cells employing a novel indirect immunostaining approach using nanobodies. Even in low labeled yeast cells, imaging a single optical slice in 3D mode allowed to confine the structure of interest to the nuclear membrane; a view which differed from recordings done in diffraction-limited confocal or 2D STED mode (Section 5.2.3). Another potential biological application of the instrument was highlighted by a first trial to visualize C2 toxin component C2I in fixed HeLa cells. The improved resolution in STED mode allowed to rule out false positive co-localization events with labeled cyclophilins, important proteins in the translocation pathway of the toxin into the cytosol (Section 5.3). Furthermore, initial data from experiments conducted labeling synaptic scaffold proteins in hippocampal synapses prove that individual synapses are resolved and the pre- and postsynaptic areas can be easily distinguished. In the future we plan to image mutated scaffold proteins of the ProSAP/Shank family and attribute changes in their appearance to altered function using super-resolution imaging (Section 5.4).

In addition to practical work, a theoretical model is proposed which shows that spatial resolution in STED microscopes can be further increased by taking the arrival times of detected photons into account (Chapter 3). This approach constitutes a novel option for STED microscopes either operating in pulsed or continuous wave (CW) mode. The importance of this finding is underlined by its use in commercial STED microscopes these days.

To conclude, super-resolution fluorescence microscopy enables the three-dimensional imaging of transparent biological specimens with unsurpassed resolution down to a few nanometers. Achieving such a resolution with a (far field) light microscope was deemed impossible until recent times. I present a fully working 3D dual-color STED nanoscope and successfully prove its superiority over diffraction-limited microscopy on a variety of different samples. This break-through in imaging technology will tremendously stimulate research across the disciplines while it is being made available to the community outside of specialized optics labs.

In the following chapter the basic photophysical processes exploited in flu-

orescence and stimulated emission depletion microscopy are explained laying the basis for the subsequent chapters of this thesis.

Chapter 2

Microscopy and photophysical processes

2.1 Diffraction patterns and resolution

As mentioned in the introduction, the wave nature of light sets a limit on the achievable resolution in microscopes. Light is subject to diffraction due to its wave nature. As a result, an infinitesimally small three-dimensional object imaged with a microscope will be considerably broadened in all dimensions to what is known as the point-spread function (PSF). The shape of the intensity diffraction pattern in two dimensions is described by the so-called Airy pattern [Airy, 1835]. It appears as concentric rings around a central maximum when a plane wave incident on a lens acting as a circular aperture is focused onto a screen and is of finite size (Fig. 2.1 A). It is given by [Hecht, 2002]

$$I(\theta) = I(0)\left[\frac{2J_1(ka\,sin\theta)}{ka\,sin\theta}\right]^2 \tag{2.1}$$

where J_1 is the Bessel function of the first order, k is the wavenumber $2\pi/\lambda$, a the radius of the aperture i.e. lens and θ the angle of observation. When two objects are located close together the two resulting Airy patterns can partially overlap. When brought even further together the Airy pattern will overlap to a degree which makes it impossible to distinguish the two

objects. Information regarding the position of objects small with respect to λ is thus hidden in the large diffraction pattern. How close two Airy disks can be brought together and still be considered resolvable has been defined in various ways [den Dekker and van den Bos, 1997]. The two most common definitions are explained in more detail, namely the Rayleigh limit [Strutt, 1899] and the full-width-at-half-maximum criterion (FWHM, (Fig. 2.1 B).

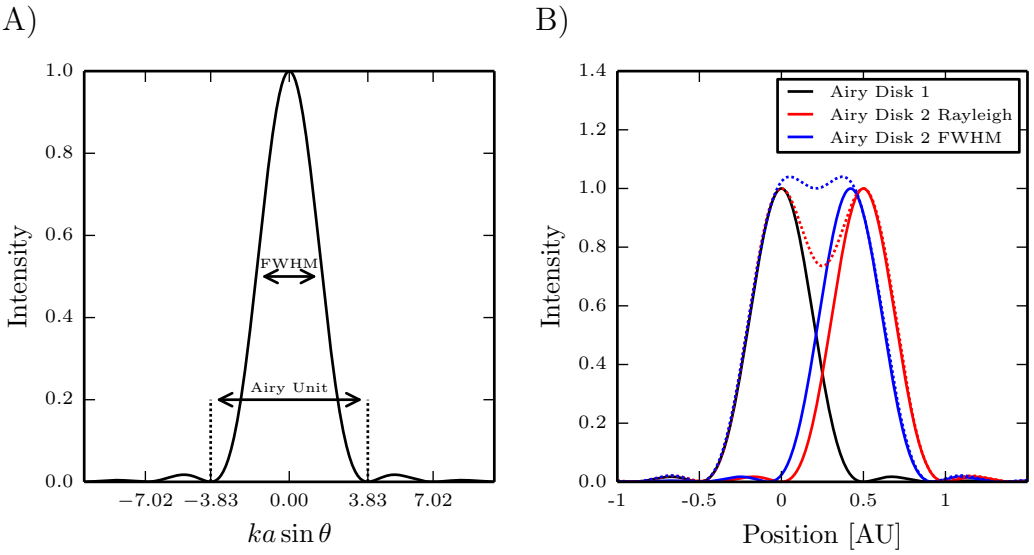

Figure 2.1: The Airy pattern and the definition of resolution according to the Rayleigh limit and the FWHM criterion. A) The Airy pattern shows a prominent main peak alongside smaller side lobes. The first minimum is located at $ka \sin\theta = \pm 3.83$. The distance between the first minima is called one Airy unit (AU) and amounts to $1.22\frac{\lambda}{NA}$. B) Two Airy disks positioned such that the maximum off the first pattern (black) coincides with the first minimum of the second pattern (red, Rayleigh limit) or is displaced by the FWHM (blue). The dotted lines show the corresponding total intensities of the two neighboring intensity diffraction patterns.

The Rayleigh limit states that two objects are resolvable when the corresponding diffraction patterns are at least 0.5 Airy units offset with respect to each other. This is the case when the maximum of one pattern coincides with the first minimum of the second pattern. A more modern definition of resolution is simply the use of the FWHM of the Airy pattern as the minimal distance between two diffraction patterns to render them resolvable (Fig. 2.1 B, [Lauterbach, 2012]). These definitions are somewhat arbitrarily

chosen as the resolution can be severely hampered in real images by the presence of noise and non-equal intensities of the objects under investigation. In scanning microscopy such as stimulated emission depletion microscopy, the FWHM of an object can be readily measured. To this end, a Gaussian function is fitted to the image of a small object as it approximates the central maximum of the Airy pattern very well [Kubitscheck, 2013]. Therefore, when discussing the resolution achievable with the herein presented setup it is measured by using the FWHM (Chapter 4).

The actual image recorded by a microscope will be a convolution of the actual objects with the PSF. This does not pose a problem if the object and its features are large compared to the point-spread-function. However, in biology many objects are small compared to the resolution limit and thus detail is lost in the imaging process. For a standard fluorescence wide field microscope, in which the sample is simultaneously illuminated and signal detected over the whole field-of-view using a camera, the lateral resolution is most commonly given by [Stender et al., 2013]

$$\delta_{Wide\,field,lateral,Rayleigh} \approx \frac{0.61\lambda_{Emission}}{NA} \tag{2.2}$$

where $\delta_{Widefield,lateral,Rayleigh}$ denotes the distance between two objects which are considered to be resolvable according to Rayleigh in a wide field microscope. $\lambda_{Emission}$ is the wavelength of emission in the case of fluorescence microscopy. In the case of the FWHM criterion, the resolution of a wide field microscope is given by [Stender et al., 2013]

$$FWHM_{Wide\,field,lateral} \approx \frac{0.51\lambda_{Emission}}{NA}. \tag{2.3}$$

The axial resolution is lower when only one objective lens is used. For numerical apertures larger than 0.5, commonly used in modern fluorescence microscopy, axial resolution is given by [Stender et al., 2013]

$$\delta_{Wide\,field,axial,Rayleigh} \approx \frac{\lambda_{Emission}}{n - \sqrt{n^2 - NA^2}} \tag{2.4}$$

according to the Rayleigh limit. In the case of the FWHM criterion,

Equation 2.4 changes to [Stender et al., 2013]

$$FWHM_{Wide\,field,axial} \approx \frac{0.88\lambda_{Emission}}{n - \sqrt{n^2 - NA^2}} \tag{2.5}$$

Equations 2.2 - 2.5 describe the limit of resolution for wide field fluorescence microscopes. Features in a sample which are substantially smaller in their lateral and/or axial dimensions will be blurred and appear as the above introduced diffraction pattern.

A particular problem in wide field fluorescence microscopy is the presence of out-of-focus light. In thick samples such as a layer of eukaryotic cells the whole sample is flooded with excitation light. Emission of fluorescence will thus occur throughout the thickness of the sample and will contribute to the signal recorded by the microscope detector. This can considerably worsen the effective resolution achieved as the signal-to-noise ratio (SNR) decreases and the theoretical Airy diffraction pattern is lost in background noise. In such a setting the use of the above mentioned resolution criteria will most likely fail.

2.2 Confocal microscopy

The motivation for the design of a new type of microscope by Marvin Lee Minsky in the 1960's was the problem of out-of-focus and scattered light deteriorating the image in conventional wide field microscopes (Section 2.1, [Minsky, 1988]). These issues can be alleviated by focusing light to a diffraction limited spot (Airy pattern, Section 2.1) instead of to a whole field-of-view as in wide field microscopy (Fig. 2.2). Additionally, a second microscope path is built which detects light only from a diffraction limited spot in the focal plane by the use of a pinhole in front of the detector. Those two focal spots, the excitation diffraction pattern and the detection focal point are co-aligned thus forming a confocal focal point. In its most common form, one objective lens is used to create the two foci making up the confocal spot. To actually form an image, the confocal spot is raster-scanned across the sample and signal is recorded at each point. The scanning can either be performed by

scanning the sample underneath the fixed objective or by scanning the laser beams across a fixed sample (laser scanning microscope, LSM).

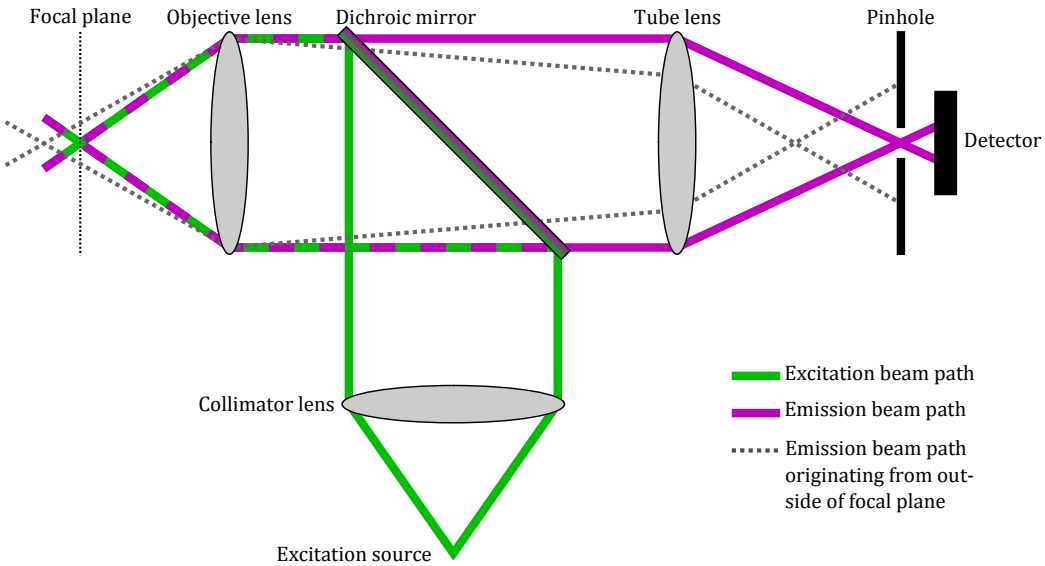

Figure 2.2: Simplified schematic of a confocal fluorescence microscope. Excitation light (green) of suitable wavelength is coupled into the optical axis using a dichroic mirror and focused to a diffraction limited spot in the focal plane using an objective lens. The fluorescence emitted from the excitation spot in the focal plane (magenta) is focused onto a pinhole of size $\sim$ 1 AU and is detected after passing the pinhole aperture. Emitted or scattered light from out-of-focus points (dashed grey) is largely blocked by the pinhole depending on its distance from the focal excitation spot. The pinhole thus acts as a spatial filter and rejects out-of-focus light leading to much improved optical sectioning capabilities over wide field microscopy. Excitation and emission filters omitted for sake of clarity.

The resolution of a confocal microscope can be superior to that of a wide field microscope. This is due to the pinhole which needs to be small compared to the diffraction pattern impinging on it in order to have any effect on lateral and axial resolution ($\lesssim 0.25\,AU$). For such a small pinhole size, the total PSF of the system is given by the square of the diffraction pattern accounting for the two Airy patterns, the illuminating PSF and the detection PSF. The FWHM of the total confocal PSF is smaller by $\sim 1/\sqrt{2}$ compared to the wide field Airy pattern assuming the width of the two individual PSFs are equal. To this end, the FWHM for the confocal case is given by

$$FWHM_{Confocal,lateral,pinhole \lesssim 0.25\,AU} \approx \frac{0.37\lambda}{NA} \tag{2.6}$$

Note that the Rayleigh criterion is not applicable to describe the increase in resolution as the position of the minima of the Airy intensity diffraction pattern stays the same upon squaring it in the confocal case. The axial FWHM employing a small pinhole is given by [Kubitscheck, 2013]

$$FWHM_{Confocal,axial,pinhole \lesssim 0.25\,AU} \approx \frac{0.64\lambda}{n - \sqrt{n^2 - NA^2}} \tag{2.7}$$

Equations 2.6 and 2.7 describe the improvement of resolution in comparison to the wide field microscope when a small pinhole $\lesssim 0.25\,AU$ is used. However, in fluorescence microscopy, a pinhole diameter of ~ 1 AU is usually used to improve the detection efficiency of the microscope since nearly 84% of the total intensity arrives within the main maximum of the Airy disk [Born and Wolf, 1999]. Further increasing the pinhole diameter does not improve the collection efficiency much, but reduces the ability to reject out-of-focus light. It becomes clear that using a pinhole of a fraction of one Airy unit will thus deteriorate the detection efficiency. Using a pinhole diameter corresponding to ~ 1 AU in front of the detector will yield the following equations for the lateral and axial resolution [Stender et al., 2013]

$$FWHM_{Confocal,lateral,pinhole \sim 1\,AU} \approx \frac{0.51\lambda_{Excitation}}{NA} \tag{2.8}$$

and

$$FWHM_{Confocal,axial,pinhole \sim 1\,AU} \approx \frac{0.88\lambda_{Excitation}}{n - \sqrt{n^2 - NA^2}} \tag{2.9}$$

respectively. These are very similar to Equations 2.3 and 2.5 but differ in that the excitation wavelength is used instead of the emission wavelength. Since the excitation wavelength is shorter than the emission wavelength in fluorescence microscopy due to the Stokes shift, an (ever so) slight improvement in resolution in confocal microscopy is achieved. Thus, confocal microscopy is not applied in the realm of fluorescence microscopy simply because of its resolution improvement. As initially stated, the real benefit of confocal over

wide field microscopy is its greatly improved optical sectioning capability by using a pinhole in front of the detector (Fig. 2.2). As such, the optimal pinhole diameter is a trade-off between better detection efficiency but less out-of-focus light suppression (Pinhole diameter $\gg 1\,AU$) or low detection efficiency and good out-of-focus light rejection (Pinhole $\ll 1\,AU$).

2.3 Fluorescence

While spontaneous emission was first described as far back as the 16th century, the optical phenomenon was first called fluorescence by George Gabriel Stokes [Stokes, 1852]. It describes the emission of a photon from an electronically excited state in fluorescent molecules, named fluorophores.

The process of fluorescence is best explained by the use of a Jablonski diagram (Fig. 2.3). It illustrates the singlet ground and first electronic state (S_0 and S_1, respectively) as well as the first triplet state, T_1, along with the vibronic states that a molecule exhibits for each electronic state (denoted by *).

A variety of state transitions can occur in fluorophores. The actual fluorescence rate observed will be governed by a combination of these processes. At thermodynamic equilibrium molecules occupy the lowest vibrational level of the ground state according to the Boltzmann distribution (S_0, [Sauer et al., 2011]). Upon excitation an orbital electron makes a state transition from the relaxed ground state, S_0, to a vibrational excited higher electronic state (S_1^*) dependent on the energy of the excitation ($h\nu_{Exc} + S_0 \rightarrow S_1^*$). The actual duration for this stimulated absorption is on the order of femtoseconds and therefore is one of the fastest photochemical processes [Turro et al., 2010]. If excitation to higher electronic states $S_n > S_1$ takes place, rapid non-radiative conversion to the S_1 state occurs in most compounds, termed internal conversion ($S_n \rightarrow S_1^*$, within 10^{-10} to 10^{-14} seconds). Thus, it is sufficient in the following discussion to only consider state transitions from the S_1 state [Turro et al., 2010].

The excited state quickly relaxes to the lowest vibrational level of the electronic state S_1 in $\sim$ picoseconds ($S_1^* \rightarrow S_1$). The S_1 state can be depop-

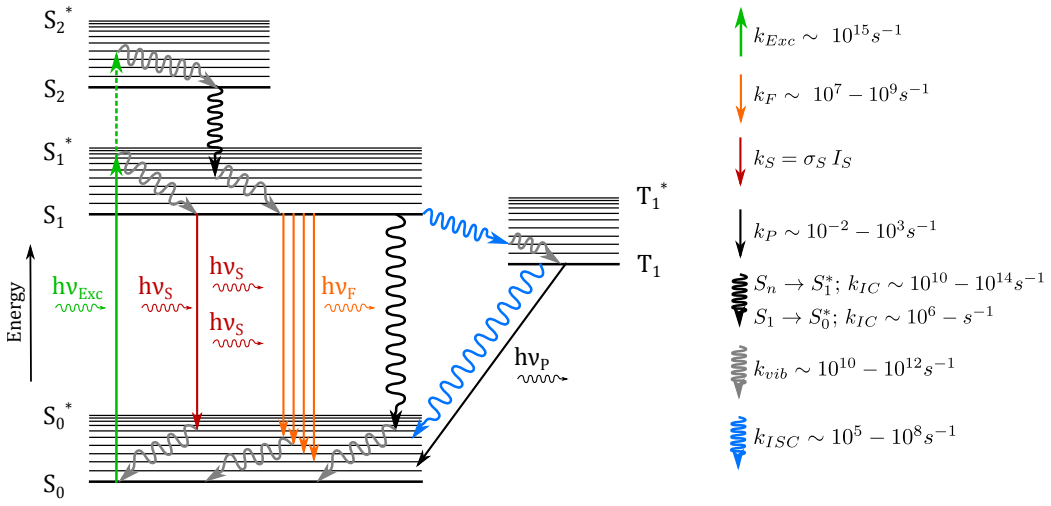

Figure 2.3: Jablonski diagram depicting the various electronic singlet (S_n) and triplet states (T_n) involved in photophysical transitions when fluorophores interact with light. These include radiative transitions such as fluorescence/spontaneous emission $h\nu_F$, stimulated emission $h\nu_S$ and phosphorescence $h\nu_P$ as well as non-radiative transitions such as internal conversion, intersystem crossing and quenching (not shown).

ulated in several ways. First, the energy can be dissipated by radiationless conversion through internal conversion ($S_1 \rightarrow S_0^*$). The rate k_{IC} of this transition is very low compared to other, more favorable transitions and depends on the energy gap between the S_1 and S_0 states [Turro et al., 2010]. Usually it is on the order of $\sim 10^6$ s^{-1}. A much more favorable transition from the relaxed S_1 state is the spontaneous emission of a photon, $h\nu_F$, termed fluorescence ($S_1 \rightarrow S_0^* + h\nu_F$) followed by fast vibrational relaxation to the relaxed ground state S_0. The fluorescence rate k_F varies from $\sim 10^7$ to $10^9 s^{-1}$.

A competing process which also yields a depopulation of the S_1 state is intersystem crossing from the singlet electronic S_1 state to the triplet T_1 excited state. Energy from the T_1 can be lost by non-radiative transition to the singlet ground state, S_0^*, or by the emission of a photon, $h\nu_P$, in a process called phosphorescence ($T_1 \rightarrow S_0^* + h\nu_P$). In the process of intersystem crossing and the following emission of phosphorescence the spin of the excited electron flips. Since these transitions are forbidden the associated rates are rather low. The rate of intersystem crossing k_{ISC} is on the order of $\sim 10^5$

to $10^8 s^{-1}$ and the rate of phosphorescence is $\sim 10^{-2}$ to $10^3 s^{-1}$. Fluorescence is thus the most favorable transition competing with radiationless processes.

The ability of a molecule to fluoresce when excited is expressed as the quantum yield of fluorescence,

$$\Phi_F = \frac{k_F}{k_F + k_{IC} + k_{ISC}} \tag{2.10}$$

where k_F denotes the rate of fluorescence, k_{IC} the rate of internal conversion and k_{ISC} the rate of intersystem crossing. The actual rate of fluorescence is thus dependent on the individual contribution of each process depopulating the excited electronic state S_1. The excited state lifetime, τ_{S_1}, is given by

$$\tau_{S_1} = \frac{1}{k_F + k_{IC} + k_{ISC}}. \tag{2.11}$$

and can be experimentally measured by the arrival time of spontaneously emitted photons after a short excitation light pulse. It is dependent on all radiative and non-radiative processes depopulating the excited state. The depopulation of the excited state via fluorescence follows an exponential decay given by

$$N_{S_1}(t) = N_{S_1}(0)e^{-k_F t} \tag{2.12}$$

were $N_{S_1}(t)$ is the number of molecules in the S_1 state at time t and $N_{S_1}(0)$ is the initial number of molecules in the S_1 state immediately after excitation. It becomes apparent that any process which competes with the depopulation of the excited S_1 state through fluorescence will lower the quantum yield of fluorescence, Φ_F, and will also lower the lifetime of the excited state S_1. The implications of these characteristics for STED microscopy are the topic of Chapter 3.

2.4 Stimulated emission

In addition to the processes described above, the excited state can be depopulated by stimulated emission. As the name suggests, this transition is stimulated by a photon, $h\nu_S$. This stimulating photon causes the energy of the excited state S_1 to be lost in form of a photon in the same mode as the stimulating photon, i.e. the phase, wavelength and polarization of the stimulating photon and the stimulated photon are the same ($S_1 + h\nu_S \rightarrow S_0^* + h\nu_S + h\nu_S$). The rate of this forced transition is given by

$$k_S = \sigma_S I_S \tag{2.13}$$

were σ_S denotes the cross-section for stimulated emission and I_S the intensity of the stimulating beam in photons per area per unit time. To account for the process of stimulated emission, Equation 2.11 needs to be extended to

$$\tau_{S_1} = \frac{1}{k_F + k_{IC} + k_{ISC} + k_S}. \tag{2.14}$$

Consequently, under exposure of stimulating light, Equation 2.10 is rewritten as

$$\Phi_F = \frac{k_F}{k_F + k_{IC} + k_{ISC} + k_S} \tag{2.15}$$

Two important conclusions can be drawn from Equations 2.14 and 2.15. First, increasing k_S will decrease the excited state lifetime, τ_{S_1}, and concomitantly decrease Φ_F. Second, as the process of stimulated emission is stimulated and not spontaneous, k_S is easily experimentally modified by its dependence on σ_S and I_S. In other words, by applying stimulating light to a sample with fluorophores in their excited state, fluorescence can be rendered very improbable if $k_S \gg k_F$. In this case, most energy absorbed by fluorophores will not be released spontaneously but via stimulated emission, assuming that other routes of decay are negligible. The decay rate of the excited state at time t assuming only fluorescence and stimulated emission as possible decay channels is given by

$$dN_{S_1}/dt = -(k_F + k_S)N_{S_1} \tag{2.16}$$

where N_{S_1} is the population of the state S_1. Assuming $N_{S_1} = 1$ at $t = 0$ and $N_{S_1} = 0$ at $t \to \infty$ the solution of Equation 2.16 is

$$N_{S_1}(t) = e^{-(k_F+k_S)t} \tag{2.17}$$

In a pulsed configuration in which a depletion pulse with a rectangular time profile of duration t_S immediately follows a short excitation pulse the population of state S_1 right after the depletion pulse is a function of the STED beam intensity, I_S, given by

$$N_{S_1}(I_S) = e^{-k_S t_S - k_F t_S} \tag{2.18}$$

Now the time information is no longer relevant since the whole de-excitation pulse has passed and thus we have switched to a dependency on the STED beam intensity, I_S. This further reduces to

$$N_{S_1}(I_S) = e^{-k_S t_S} = e^{-\sigma_S I_S t_S} \tag{2.19}$$

assuming $k_S \gg k_F$ and $t_S \ll \tau_F$. Equation 2.19 can be evaluated for increasing I_S relative to the saturation intensity, I_{Sat} (Fig. 2.4). The saturation intensity is a fluorophore specific characteristic at which the rates of stimulated emission and fluorescence are equal ($k_S = k_F$).

It becomes apparent that the process of stimulated emission quickly saturates for high depletion beam intensities rendering fluorescence impossible if $I_S \gg I_{Sat}$. It is important to note that this forced transition via a stimulating beam is reversible. Upon recurrent excitation the molecule is excited and can again emit via fluorescence or stimulated emission (neglecting photobleaching which ultimately limits the number of photons emitted by a molecule). Stimulated emission cross-sections of fluorophores are typically on the same order of magnitude as single-photon absorption. In the case of the fluorophore Atto 647N, which is used in later experiments in this thesis, the stimulated emission cross-section was measured to be $\sigma_S \sim 10^{-16} cm^2$ at

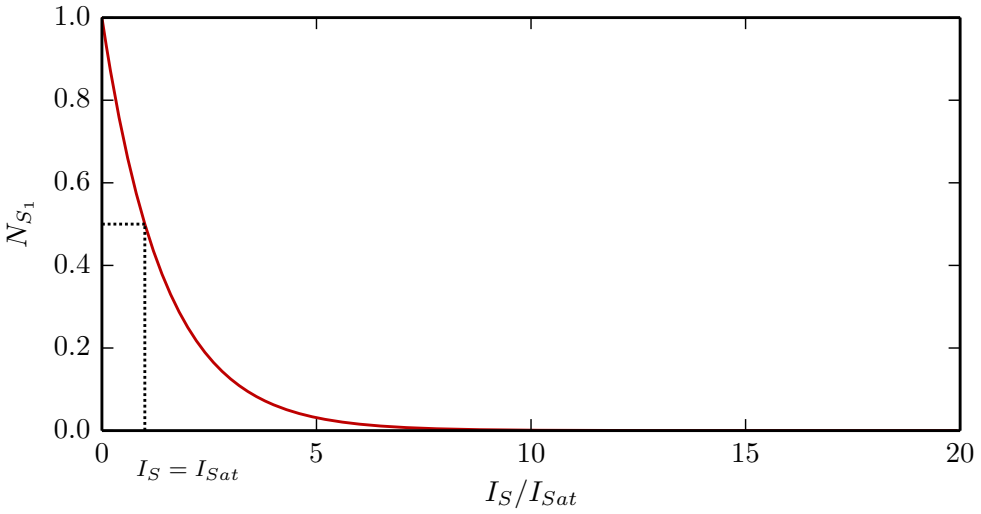

Figure 2.4: Depopulation of the excited state S_1 as a function of increasing depletion beam intensities relative to the saturation intensity I_{Sat}. Assuming a simplistic model in which the excited state can only be depleted by either fluorescence or stimulated emission, the curve describes the probability of a molecule to reside in the excited state after a pulse of stimulating light of infinitesimally short duration with an intensity of I_S/I_{Sat} has passed. At $I_S/I_{Sat} = 1$, the probability to emit via fluorescence or stimulated emission is equal and thus $k_S = k_F$. Increasing I_S above I_{Sat} saturates stimulated emission and quickly diminishes the ability of the molecule to fluoresce.

a stimulating beam wavelength of 750 nm [Rittweger et al., 2007]. The data sheet of Atto 647N lists a molar absorption coefficient ϵ of $1.5 \cdot 10^5 M^{-1} cm^{-1}$. The cross-section for absorption is then given by

$$\sigma_{Abs} = 1000 \ln 10 \frac{\epsilon}{N_A} \tag{2.20}$$

where N_A is the Avogradro constant [Lakowicz, 2006]. Thus, the cross-section for absorption for Atto 647N amounts to $\sigma_{Abs} \sim 5.7 \cdot 10^{-16} cm^2$, very similar to the cross-section for stimulated emission. I_{Sat} can be approximated by k_F/σ_S following from $I_{Sat} = I_S$ and $k_F = k_S$ at the saturation intensity and Eq. 2.13 [Hell et al., 2006, Leutenegger et al., 2010]. With a typical fluorescence rate $k_F \approx 10^9$, I_{Sat} is on the order of 10^{25} photons per square centimeter and second. This is equivalent to $\sim$ 10's MW/cm^2 [Leutenegger

et al., 2010, Hell et al., 2006]. The exact values can be experimentally measured and are specific properties of the particular dye [Rittweger et al., 2007]. Given these typical values, fluorescence emission can be prevented when a stimulating beam with an intensity of $I_S \gg I_{Sat} \approx 10\ MW/cm^2$ concomitantly depletes the excited state even when the rate of excitation is saturated $k_{Exc} \approx 10^{15} s^{-1}$. In this condition the process of stimulated emission saturates as the excited state of a molecule is depleted solely by stimulated emission.

To yield an optimal depletion efficiency via stimulated emission the photophysical processes described earlier (Fig. 2.3) set certain limits on the characteristics of the stimulating beam. In stimulated emission depletion microscopy, pulsed and continuous wave depletion lasers are commonly used. For a given time-averaged power a pulsed laser exhibits a higher pulse energy than continuous wave beams. As we have seen before stimulated emission competes with fluorescence and the rate k_S depends on I_S. Taking into consideration that fluorescence lifetime is on the order nanoseconds it becomes clear that using a pulsed excitation and depletion source will be most efficient to induce stimulated emission. In this configuration we can derive that the pulse duration of the stimulating beam should be short relative to the fluorescence lifetime to yield a high pulse energy and thus many photons inducing stimulated emission in a short time. However, one must also consider vibrational relaxation from $S_0^* \rightarrow S_0$, k_{vib_0}. This actually sets a lower limit to the stimulating beam duration. If $k_S^{-1} \approx k_{vib_0}^{-1}$ the stimulating beam will re-excite molecules from S_0^* to S_1 as the energy gap between the two states matches the photon energy of the stimulating beam. This renders the process of stimulated emission very inefficient albeit desirable high pulse energies are used. Consequently, it must be ensured that S_0^* can be efficiently depopulated by vibrational relaxation to the ground state and thus $k_S^{-1} \gg k_{vib_0}^{-1}$. To conclude this line of thought we can state that optimal depletion pulse durations range from a few picoseconds to a few hundred picoseconds given by $k_{vib_0}^{-1} \ll k_S^{-1} \ll k_F^{-1}$. One can also estimate the optimal timing between the excitation and depletion pulse to optimize stimulated emission. According to the Franck-Condon principle transitions to the S_0^* state occur from the vibrationally relaxed excited electronic state S_1. As a consequence the de-

pletion pulse can only enforce stimulated emission in excited molecules once they relax from higher vibrational level to the first excited state and should thus follow a short excitation pulse with a delay corresponding to the rate of vibrational relaxation $k_{vib} \sim 10^{10} - 10^{12} s^{-1}$.

2.5 Stimulated emission depletion microscopy

In the last sections we have seen how a scanning confocal fluorescence microscope works and how fluorescence can be suppressed by the use of depletion light of suitable intensity. Stimulated emission depletion microscopy makes use of these techniques and combines them into a microscope.

Resolution in confocal microscopy is ultimately limited by the finite size of the excitation beam. To further decrease the effective size of the fluorescence spot beyond the diffraction limit the process of stimulated emission is applied. To this end, a spatially varying intensity distribution of stimulating light is overlaid onto the excitation spot (Fig. 2.5). This depletion pattern - called the STED beam - is shaped such that its intensity is zero in the center and increases towards the periphery of the pattern. It resembles a donut and is thus often termed “donut beam” in the literature. If the STED beam intensity is high enough to induce stimulated emission, fluorescence is suppressed in areas coinciding with a high STED beam intensity. At the same time, fluorescence is left to emit in the center of the STED beam pattern as its intensity is zero at that position. Stimulated emission is thus used to selectively silence fluorescence in the periphery of the excitation spot in a STED microscope. The residual fluorescence emitted from the central area not affected by the STED beam is detected while the stimulated emission is discerned by color using optical filters and selectively discarded.

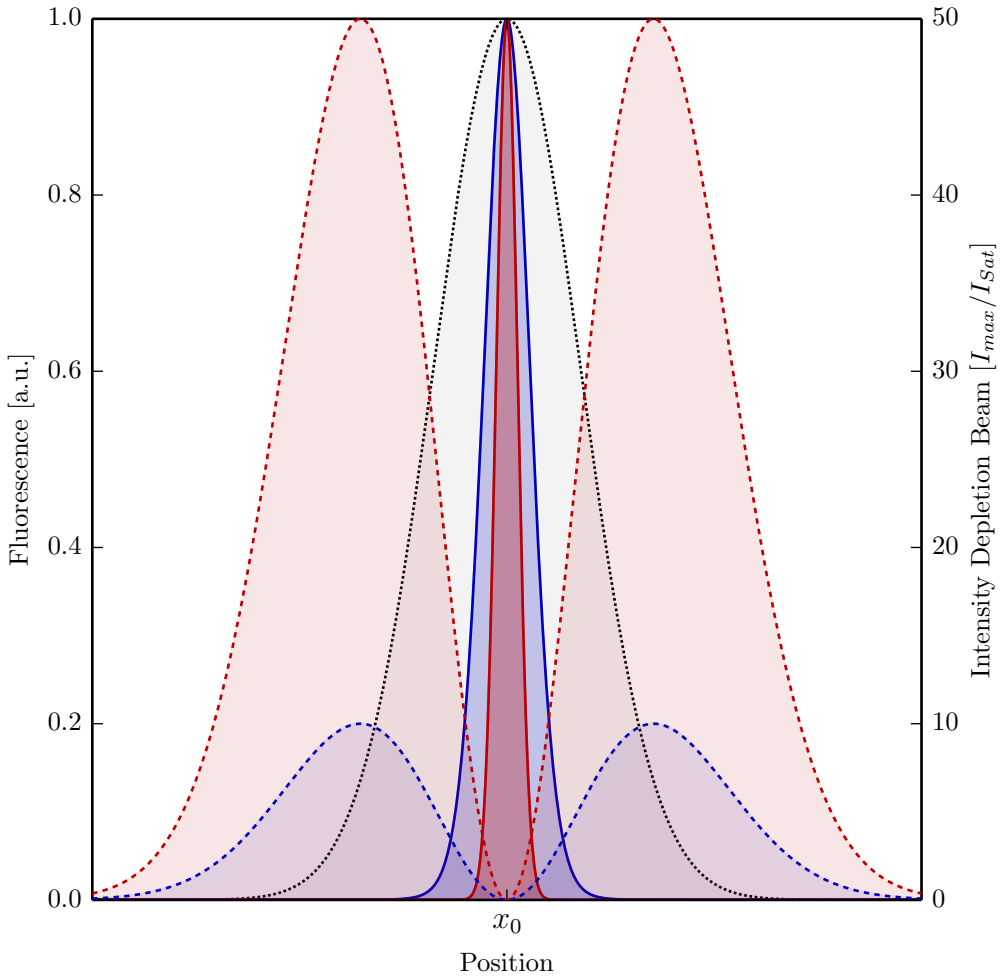

Figure 2.5: STED microscopy - the principle. The diffraction limited excitation spot of finite size (black dots, Gaussian intensity distribution, Eq. 3.11) and a spatially varying depletion beam with an intensity distribution given by the Laguerre-Gaussian, LG_{01} (Eq. 3.9) are co-aligned (blue and red dashes). Using a depletion beam with a maximum intensity corresponding to $I_{max}/I_{Sat} = 10$ (blue dashes), the width of the spot which can still fluoresce (solid blue) decreases to $\sim 31\%$ of the initial width of the excitation spot (black dots). Further increasing the STED beam intensity to $I_{max}/I_{Sat} = 50$ (red dashes) shrinks the effective spot which can still emit fluorescence (solid red) to $\sim 14\%$ of the initial width of the excitation spot (black dots). The position at which the depletion beam reaches an intensity of I_{Sat} is shifted towards the center with increasing STED beam intensities. This sharpens the effective spot and thus increases resolution arbitrarily while the excitation spot and the depletion beams are still diffraction limited. Values simulated for an infinitesimally short STED pulse duration as introduced in Equation 2.19. Note that intensities of fluorescence are displayed using the left axis and those of the STED beam using the right axis.

It becomes apparent that the resolution scales with the intensity of the depletion beam as depicted in Fig. 2.5. Lateral resolution in a STED microscope is commonly given as the FWHM by [Wildanger et al., 2008]

$$FWHM_{STED,lateral} \approx \frac{\lambda}{2NA\sqrt{1 + I_{max}/I_{Sat}}}. \tag{2.21}$$

This equation is very similar to equation 1.1 first postulated by Ernst Abbe with the additional square root term indicating the scaling of resolution with the intensity of the STED beam. As the term I_{max}/I_{Sat} can in theory be driven to infinity, resolution is not limited by diffraction anymore. Equation 2.21 does not account for the depletion beam shape, however. The spatial width and steepness of the central minimum of the depletion pattern will affect the resolution in a STED microscope. To this end, Harke et al. [2008] derived a more useful equation describing the resolution of a STED microscope not limited to the two dimensional/lateral case as in equation 2.21. The attainable resolution is given by

$$FWHM_{STED} \approx FWHM_{confocal}/\sqrt{1 + FWHM^2_{confocal} a^2 \zeta} \tag{2.22}$$

where $FWHM_{confocal}$ is the resolution obtained with the microscope in diffraction limited confocal mode, a describes the STED pattern steepness approximated by a parabola in the central minimum and ζ is the saturation factor I_{max}/I_{Sat}. With this equation at hand the importance of the shape of the depletion pattern as well as the depletion intensity on the resolution in a STED microscope becomes apparent.

2.5.1 Spectral considerations

We have learned in the last sections that in order to saturate stimulated emission, the depletion beam needs to have a high intensity relative to the excitation beam. In order to prevent excitation from the ground state by the strong depletion beam its wavelength is commonly chosen in the far end of the emission spectrum of the particular dye in use (Fig. 2.6). This

will prevent excitation (i.e. stimulated absorption) by the depletion beam. Additionally, the emission spectrum is still available for detection in between the excitation and the depletion spectra. To this end, the depletion beam wavelength is a trade-off between a high cross-section for stimulated emission at a wavelength close to the emission maximum and low re-excitation of the fluorophores.

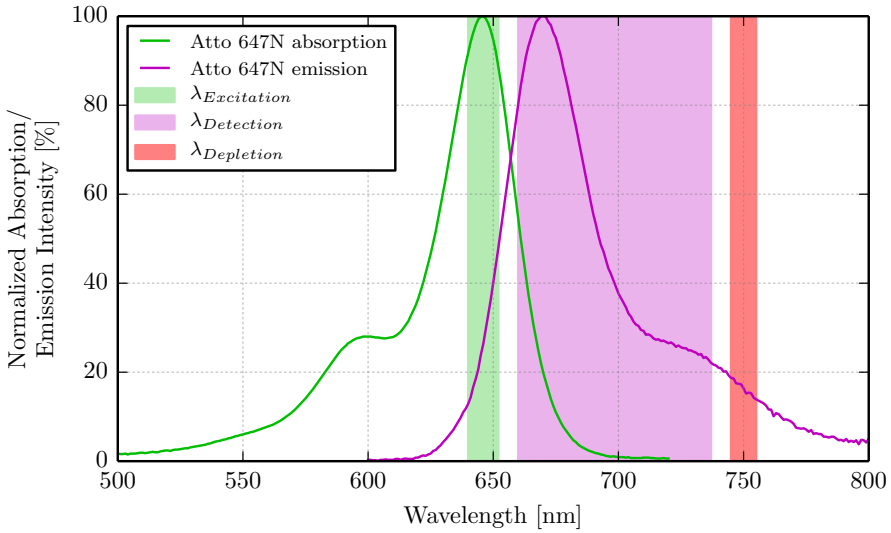

Figure 2.6: STED microscopy - spectral design. Exemplary absorption (green line) and emission (magenta line) spectra for the dye Atto 647N (data by Attotec GmbH) and the wavelength ranges typically used for efficient excitation (green fill), detection (magenta fill) and depletion through stimulated emission (red fill). This scheme allows a wide detection and prevents re-excitation of the fluorophore by the strong depletion beam as the dye practically does not absorb photons of such low energy ($\lambda_{Absorption\ spectrum} \ll \lambda_{Depletion}$).

The interested reader is directed to two studies of Hotta et al. [2010] and Rittweger et al. [2007] which focus in detail on the spectral dependency of the cross-section for stimulated emission of typical fluorophores.

2.5.2 Depletion patterns

In STED microscopy two different depletion patterns for lateral and axial resolution improvement are typically employed (Fig. 2.7). The depletion patterns are created by imprinting a spatially varying phase pattern on the

depletion beam before being focused onto the sample by the objective lens. The phase mask used to create the "donut" beam to increase lateral resolution has the shape of a vortex with a helical phase ramp of 2π. Opposing rays are rendered out of phase by π creating the prominent minimum in the center and a rim in the periphery (Fig. 2.7, upper half). The pattern in the focus will quench fluorescence from the outside towards the minimum with increasing STED beam intensity. As a result, the lateral resolution is enhanced. However, this intensity distribution is not capable of providing depletion above or below the focal plane. Consequently, axial resolution is not altered and the PSF becomes highly inhomogeneous resembling a laterally squeezed ellipsoid. The sole use of this depletion pattern using a vortex phase plate is the (currently) most common implementation of a STED microscope.

For axial resolution enhancement a different focal intensity distribution is necessary. This is achieved by employing a circular phase mask which causes a phase shift of π in the central part of the phase mask (Fig. 2.7, lower half). This effectively produces negative interference in the focal point and as a result two depletion spots above and below the focal plane. The depletion beam thus acts in the axial dimension to create a smaller effective axial spot which is left to emit fluorescence. Incoherent co-alignment of the two patterns will quench fluorescence through stimulated emission from the periphery towards the central minimum in all three dimension thus breaking the diffraction limit in 3D space. The microscope built as part of this thesis uses a combination of these two different phase masks and is described in Chapter 4.

Measured intensity distributions of the aforementioned simplified types are presented in Chapter 4 Section 4.2.5. STED microscopy is not limited to these two main types of focal intensity distributions. Phase masks to increase resolution in one dimension have been used reaching a one-dimensional resolution of $\sim$ 16 nm [Westphal and Hell, 2005, Klar et al., 2001, Heller et al., 2013] as well as a parallelized approach providing essentially four donut beams grouped together [Bingen et al., 2011]. The phase patterns are imprinted onto the beam either by means of spatial light modulators or sputtered optical elements.

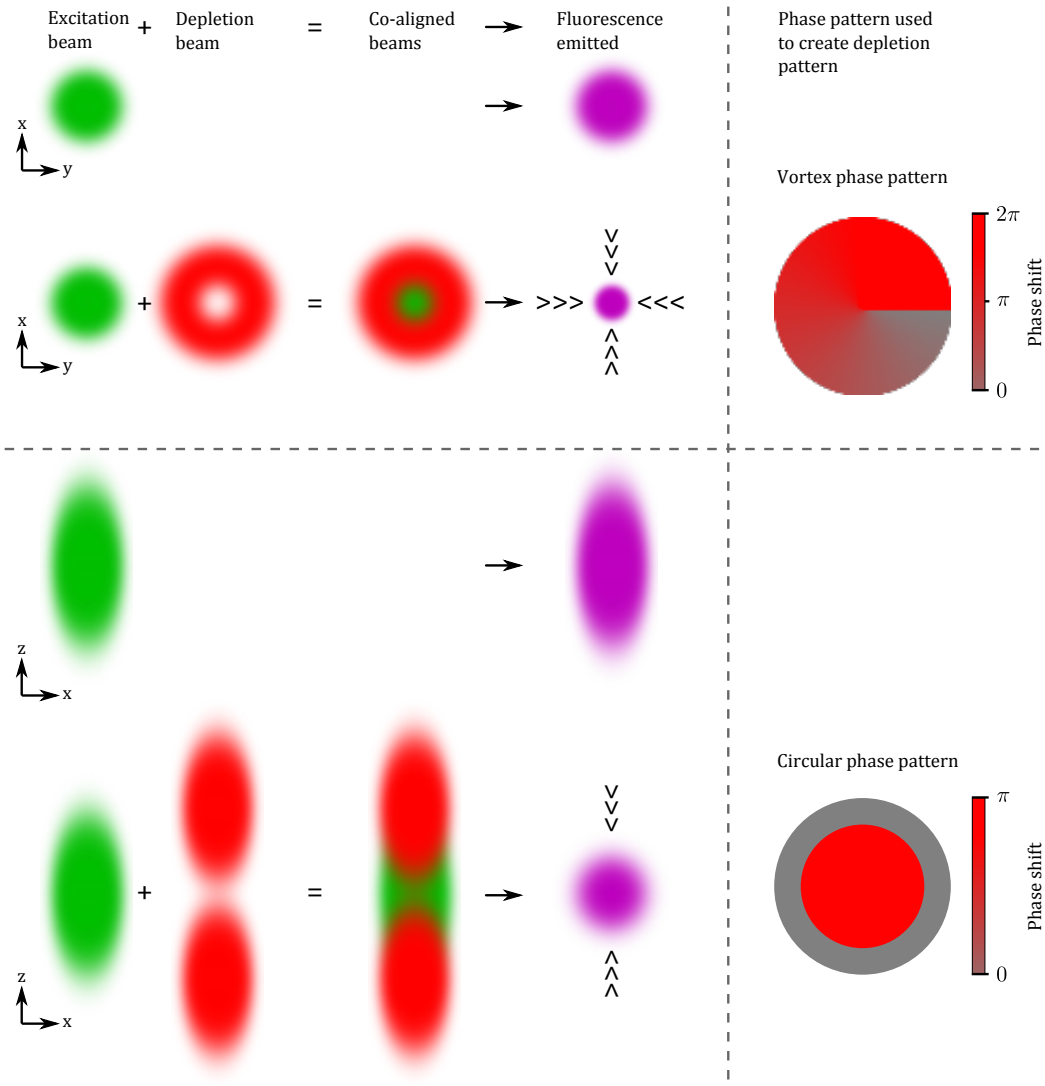

Figure 2.7: STED microscopy - schematic overview of the excitation and the two depletion patterns used for lateral (upper half) and axial (lower half) resolution enhancement in a STED microscope. For each pattern type, the confocal diffraction limited case is presented. The lateral "donut" beam acts only in the x and y while the axial depletion pattern acts along the optical axis z (as indicated by arrow heads). The vortex phase pattern imprints a phase ramp of 0 to 2π creating a central minimum in the focus. The circular phase pattern creates a minimum in the focal plane with a maximum above and below. The absolute size of the excitation, detection and depletion beams are limited by diffraction. The increase in resolution is solely due to saturating stimulated emission in areas coinciding with a large depletion beam intensity and constraining fluorescence to the lateral and axial central minimum. These sketches are limited in detail for the sake of clarity. Images of the actual focal intensity distributions are discussed in Chapter 4 Section 4.2.5

2.5.3 Variations of STED microscopy

Since the initial idea of STED microscopy by Stefan Hell in 1994, a tremendous variety of the implementation of STED microscopy has emerged. A lateral resolution down to $\sim$ 20 nm has been achieved in biological specimens using pulsed laser sources [Donnert et al., 2006, Göttfert et al., 2013]. In fluorescent nitrogen vacancies in diamond, Rittweger et al. [2009] demonstrated PSFs with a width as small as 5.8 nm.

STED microscopes have been built using a CW laser source for excitation and depletion [Willig et al., 2007] or only depletion [Vicidomini et al., 2011] with a pulsed excitation. The use of CW lasers enables better counting statistics as the sample is continuously illuminated. This comes at the cost of higher depletion intensities as compared to pulsed setups being required to achieve the same resolution. However, in a pulsed STED microscope, only one photon per laser pulse and fluorophore can be counted leading to reduced count rates. This is caused by the short excitation pulses (on the order of 100's picoseconds) relative to the lifetime of fluorophores ($\sim 5\,ns$) thus exciting a fluorophore only once per laser pulse. Additionally, when using avalanche photodiodes with a dead time of many 10's of nanoseconds only one photon per laser pulse can be detected. The implications of CW and pulsed STED microscopy with regard to the resolution attained is discussed in detail in Chapter 3 [Moffitt et al., 2011].

While most STED microscopes are implemented as one channel microscopes, the technique itself does not set this limit. Indeed, Neumann et al. [2010] and Meyer et al. [2008] showed the feasibility of dual-color STED microscopy. While these publications work on the principle of separating the necessary excitation, detection and depletion wavelength by the use of optical filters, Bückers et al. [2011] discriminates a third fluorophore by lifetime analysis in a setup similar as the one used by Neumann et al. [2010].

Wildanger et al. [2009] describe a STED microscope which combines the lateral and axial depletion patterns presented in Section 2.5.2 to yield 3D super-resolution in a one channel microscope. In Chapter 4, I present a microscope design which provides 3D super-resolution in two channels using

a single super-continuum laser source.

A distinct advantage of STED microscopy over optical reconstruction techniques is its speed (see Section 2.6 for details). Fluorescence and stimulated emission are very fast processes hardly limiting image acquisition time. To this end, video rate STED microscopy at 28 frames per second on living neurons was shown by Westphal et al. [2008].

As mentioned before, axial resolution in a standard confocal microscope which uses one objective lens is worse than lateral resolution. 4π microscopy resolves this by coherent superposition of two excitation foci using two counter-propagating beams focused by two opposing objective lenses [Hell and Stelzer, 1992]. This significantly increases the effective NA and thus resolution to about 150 nm in all dimensions [Nagorni and Hell, 1998]. This approach was shown in conjunction with depletion beams to yield superior resolution of $\sim$ 30 nm in all dimensions, a technique termed 4π-STED microscopy or IsoSTED [Schmidt et al., 2008].

2.5.4 RESOLFT

In the last section we have seen how resolution in the far-field can be pushed below the diffraction limit by transiently switching fluorescence off by the process of stimulated emission. Since the initial conception of STED microscopy, other ways to temporarily silence spontaneous emission have been employed to increase resolution. The common ground of all these methods is a targeted read-out of spatially confined fluorescence brought about by transiently quenching fluorescence in parts of the focus. The acronym RESOLFT stands for reversible saturable optical fluorescent transition and was termed by Stefan Hell to accommodate the various implementations of this approach under one roof [Hell, 2007, 2009]. A member of this family, ground state depletion microscopy (GSD), uses the metastable triplet dark state, T_1, to temporarily silence fluorescence [Hell and Kroug, 1995, Hofmann et al., 2005]. It utilizes a pump beam of the same beam shape as the depletion beam in STED microscopy to optically transfer dye molecules to T_1 rendering molecules unresponsive to further excitation by the follow-

ing Gaussian probe beam. The benefit of using the triplet state instead of stimulated emission lies in the lifetimes of the associated states. Stimulated emission competes with the lifetime of $\tau_{S_1} \approx 5\ ns$ and thus high depletion intensities are necessary to render stimulated emission the dominant process. In GSD microscopy, the pumping beam intensities are reduced by three orders of magnitude because the triplet state has a long lifetime on the order of μs [Hofmann et al., 2005]. Populating the T_1 state can thus be accomplished by less photons per unit time to transiently silence fluorescence. The increase in resolution is brought about by saturating the transition to the T_1 state thus creating a smaller effective area in which fluorescence can occur equivalent to the STED counterpart. The obvious advantage of GSD is the reduced focal intensities alleviating possible phototoxic effects on the sample. This advantage is lost to some degree since triplet states present first steps in photobleaching, a prominent side effect in GSD microscopy. The lower intensities required allow for the use of cheaper, low intensity laser sources.

Switching fluorescence can also be brought about by exploiting photochemical processes instead of photophysical state transitions discussed so far. To this end, Hofmann et al. [2005] used cis-trans photoisomerization to switch the protein asFP595 into a non-fluorescent trans state. The lifetime of the dark state in the presence of light bringing about fluorescence is on the order of $\sim$ ms which effectively reduces the necessary beam intensities to bring about the switch to minute levels of only $\approx 10\ W/cm^2$, up to $\sim$ six orders of magnitude lower as in STED microscopy [Jensen et al., 2014]. Due to the relatively slow kinetics involved, pixel dwell times have to be relatively long in order to collect enough signal. While this seems like a drawback, the scheme can be massively parallelized by scanning multiple donut beams across the sample at once. This is not so straightforward to do in STED microscopy because of the tremendous power put into the sample in such a case. With novel reversibly switchable fluorophores at hand [Grotjohann et al., 2012], Chmyrov et al. [2013] demonstrated the parallelization approach by recording images with 116022 donuts in parallel cutting down imaging time to seconds for a 50 μm field of view instead of 10's of minutes for a 10 μm field as in the case of single beam implementations. Recently,

Lavoie-Cardinal et al. [2014] successfully extended this approach to two colors using the reversibly switchable proteins rsCherryRev1.4 and rsEGFP2 or Dronpa-M159T.

Further RESOLFT techniques have been demonstrated such as saturated patterned excitation microscopy (SPEM, [Heintzmann et al., 2002]) and saturated structured illumination microscopy (SSIM, [Gustafsson, Mats G L, 2005]) but are not discussed here in detail.

2.6 Optical reconstruction microscopy

All methods described in the last section are so-called targeted read-out techniques in which the location of fluorescence emission is precisely controlled by a single zero such as the central minimum in the donut beam in STED microscopy or multiple zeroes in parallelized versions (Section 2.5.4). In a sequential manner the zero is scanned across the sample to record an image while the sharp effective PSF is able to discriminate fluorophores closer together than the diffraction limit. In 2006, Rust et al. [2006], Betzig et al. [2006] and Hess et al. [2006] validated another approach implemented in a wide field fluorescence microscope. The similar techniques record sub-diffraction images by stochastically switching fluorophores on or off by light. One must ensure that only a small subset of all fluorophores are able to fluoresce at a point in time and that their distance is greater than the diffraction limit. If this is the case the center of the appearing Airy patterns can be localized by fitting with great precision on the order of a few tens of nanometers dependent on the photons counted per blob. Recording many thousand frames with a different subset of fluorophores in the on state allows the reconstruction of a super-resolved image which basically consists of the fitted center positions of all fluorophores. The image thus does not represent raw data as in the case of STED microscopy. A few variations of the initial idea exist [Deschout et al., 2014, Thompson et al., 2012, Shtengel et al., 2009, Sauer, 2013] but this short introduction should suffice for this work .

To conclude, in contrast to RESOLFT microscopy, optical reconstruction microscopy is markedly different in that the position of fluorescence to be

recorded is not predetermined but varies randomly. The common ground of the two concepts is that fluorescence is in one way or the other switched off for some time. The advantages of optical reconstruction microscopy is the ease of implementation using essentially a standard epi-fluorescence microscope with a fast camera and the high resolution of < 20 nm that has been achieved [Requejo-Isidro, 2013, Toomre and Bewersdorf, 2010, Huang et al., 2009, Hell, 2009]. Disadvantages are its relatively slow imaging speed brought about by the necessity to collect as many photons as possible per fluorophore in order to be able to precisely locate its position. This is especially true for imaging densely labeled structures as during a single acquisition frame no two emitters are allowed to be in the on state within a distance smaller than the diffraction limit. Contrary, in RESOLFT microscopy, the position of a fluorophore is predetermined by the known position of the scanning laser beams and thus, in theory, only one photon per fluorophore needs to be detected (in the case of a background-free image).

With new fluorophores being engineered to the specific needs of super-resolution imaging and adaptive optics helping to create optimal focal spots, these restrictions will most likely be disappearing in the time to come.

Chapter 3

T-STED

In the last section I have introduced the reader to the general concept of STED microscopy. The core principle behind the resolution enhancement of STED is the ability to encode spatial information in the strength of a second decay channel brought about by a spatially varying depletion beam intensity distribution. This information is then extracted by selectively discarding photons emitted in the spectral range of the depletion beam from those emitted via spontaneous emission. However, when an excited fluorophore is subject to an additional decay channel, the probability of emitting via spontaneous emission is not the only physical property of the fluorophore that is modified. The lifetime of the excited state τ_{S_1} also changes, independent of the choice of decay channel because it depends on all radiative and non-radiative processes involved (Equation 2.14, Chapter 2). Therefore, areas coinciding with a high depletion beam intensity such as the outer periphery of the excitation spot (under illumination with a donut beam intensity distribution; Fig. 2.5 and 2.7) exhibit a shorter lifetime as fluorophores in the center of the depletion beam. Consequently, the spontaneous emission from the outer periphery will arrive at the detector earlier than fluorescence from the center of the excitation beam. Discarding early photon counts will sharpen the effective PSF from the periphery towards the center. Thus, spatial information is also encoded in the photon arrival times of the spontaneous emission, and it should be possible to improve the resolution of STED microscopy by

extracting this temporal information.

In this chapter, we consider the arrival times of the spontaneously emitted photons from excited fluorophores exposed to a spatially varying depletion beam. We show that spatial information is encoded in the fluorescent lifetimes of these fluorophores and that photon arrival times can be used to decrease the spatial extent of the effective PSF. We consider situations in which the STED beam is either pulsed or continuous wave, and show that in both situations time-gating the fluorescence emission signal, i.e. discarding photons that arrive before a specific time, increases the spatial resolution of the final image. However, this increase in resolution is accompanied by a reduction in image brightness. We term this technique time-gated STED microscopy (T-STED) and conclude by discussing the potential benefits of this type of measurement.

The work described in this chapter has been a collaborative effort between Dr. Jeffrey R. Moffitt and myself and has been published [Moffitt et al., 2011]. This chapter is adapted from the original publication with some minor changes. The final discussion also contains information about experimental findings after the publication of the theoretical paper.

3.1 Temporal dynamics in a STED measurement

To determine the spatial information encoded in excited fluorophore lifetimes, we consider a set of n_0 excited fluorophores at position r with unstimulated lifetimes of $\tau = 1/k$ in the presence of a stimulating beam with a spatially-varying intensity, $I(r)$. We start by assuming that this stimulating beam is pulsed with finite duration, t_S, immediately following an excitation pulse of much shorter duration, and, in later sections, we generalize these results to CW STED sources [Willig et al., 2007]. For simplicity, we also assume that vibrational relaxation times are negligible compared to the STED pulse duration or the fluorophore lifetime though this assumption can be relaxed if necessary [Leutenegger et al., 2010]. Finally, we also neglect alternative decay

routes for the excited fluorophores, i.e. triplet states or quenching, as the presence of these processes will only lower the effective number of excited fluorophores not change the temporal dynamics we discuss here assuming these processes do not show any spatial dependence. Thus, our analysis begins at $t = 0$ with all fluorophores in the same excited state with the same cross-section for stimulated emission, σ (the cross-section for the related absorption transition [Hell and Wichmann, 1994]).

Under these assumptions the number of excited fluorophores at position r, $n(r,t)$, decays in time as

$$\frac{d\,n(r,t)}{dt} = -kn(r,t) - \sigma I(r)(1-\Theta(t-t_s))n(r,t) \tag{3.1}$$

where $\Theta(t-t_S)$, the Heaviside step function, represents the finite duration of the STED pulse. We consider this pulse time-profile to simplify our analysis and allow analytic results; however, more complicated profiles can be considered, e.g. Gaussian profiles, with little effect on the dynamics we discuss here.

As time progresses the number of photons emitted from position r in the stimulated channel, N_S, and the spontaneous channel, N_F, grow as

$$\frac{dN_S(r,t)}{dt} = -\sigma I(r)(1-\Theta(t-t_s))n(r,t), \tag{3.2}$$

$$\frac{dN_F(r,t)}{dt} = kn(r,t). \tag{3.3}$$

These expressions can be solved via direct integration, yielding the number of excited fluorophores as a function of time

$$n(r,t) = n_0 \begin{cases} e^{-(k+\sigma I(r))t} & : t \leq t_S \\ e^{-\sigma I(r) t_S} e^{-kt} & : t > t_S \end{cases} \tag{3.4}$$

and the total number of photons in each of the two decay channels emitted during time t

$$N_F(r,t) = n_0 \begin{cases} \frac{k}{k+\sigma I(r)}(1 - e^{-(k+\sigma I(r))t}) & t \leq t_S \\ \frac{k}{k+\sigma I(r)} + \frac{\sigma I(r)}{k+\sigma I(r)} e^{-(k+\sigma I(r))t_S} - e^{-\sigma I(r) t_S} e^{-kt} & t > t_S \end{cases} \tag{3.5}$$

and

$$N_S(r,t) = n_0 \begin{cases} \frac{\sigma I(r)}{k+\sigma I(r)}(1 - e^{-(k+\sigma I(r))t}) & t \leq t_S \\ \frac{\sigma I(r)}{k+\sigma I(r)}(1 - e^{-(k+\sigma I(r))t_S}) & t > t_S. \end{cases} \tag{3.6}$$

The fraction of excited fluorophores that emit in each of the two channels from position r is derived from the infinite-time limit, yielding

$$\lim_{t\to\infty} N_F(r,t)/n_0 \equiv \eta_{STED}(r) = \frac{k}{k+\sigma I(r)} + \frac{\sigma I(r)}{k+\sigma I(r)} e^{-(k+\sigma I(r))t_S} \tag{3.7}$$

and

$$\lim_{t\to\infty} N_S(r,t)/n_0 = \frac{\sigma I(r)}{k+\sigma I(r)}(1 - e^{-(k+\sigma I(r))t_S}). \tag{3.8}$$

By constructing the final image only from photons emitted via spontaneous emission, i.e. Equation 3.7, the typical STED microscope exploits the spatial information encoded in the choice of decay channel - the $I(r)$ dependence in Eq. 3.7 - to improve the spatial resolution. Equation 3.7 is known as the STED depletion factor, η_{STED}. However, the presence of a spatial dependence of the decay rate of the excited state $k_{S_1} = k + \sigma I(r)$ in the exponent of Eq. 3.5 brought about by the stimulating beam also changes the arrival time of emitted photons, independent of the decay channel, confirming that spatial information is also encoded in the temporal dynamics of the fluorescence signal.

3.2 Spatial dependence of decay channels and arrival times

To illustrate the effects of a spatially varying STED beam on the choice of decay channel and on the photon arrival times, we consider a uniform field of

excited fluorophores exposed to a STED beam with an intensity distribution given by the Laguerre-Gaussian, LG_{01},

$$I(r) = \gamma r^2 e^{-2r^2/\omega^2} \tag{3.9}$$

where ω controls the spatial extent of this beam and γ sets its intensity (Fig. 3.1 A and B). γ is related to the total power of the STED beam, P, via $\gamma = 4P/(\pi\omega^4)$.

For pulsed STED measurements, the ability of the STED beam to deplete excited fluorophores can be characterized with the dimensionless number, the STED strength,

$$S = \sigma\gamma\omega^2 t_S = \sigma\epsilon. \tag{3.10}$$

To separate the effect of pulse duration from the total energy contained in the STED beam, it will be useful to redefine the STED strength in terms of the quantity, $\epsilon = \gamma\omega^2 t_S$, which is proportional to the total energy in the STED pulse. Thus, if the energy in the pulse is constant, varying the pulse duration will not vary the STED strength.

We consider a specific example where the pulse duration is equal to the unstimulated fluorophore lifetime and the STED strength is such that the FWHM of the effective PSF is reduced by a factor of 2 (Later we will derive explicit equations that allow one to determine the specific values for the STED strength required for reaching a certain resolution). Fig 3.1 B shows that the introduction of this STED beam creates two regions of depleted spontaneous emission in an otherwise uniform field of excited fluorophores. In this case, fluorophores located at the maximum STED intensity, r_{max}, will emit 80% less spontaneous emission. Nevertheless, these fluorophores will still emit $\sim$ 20% of their fluorescence via this channel, and these photons will ultimately degrade the resolution of the final image.

While the color of these photons cannot be used to discriminate the position of the fluorophore, Fig. 3.1 C and 3.1 D and Eq. 3.5 reveal that the arrival time of these photons can partially distinguish the fluorophore position. After a time of just 1/10 of the unstimulated lifetime, only 10% of

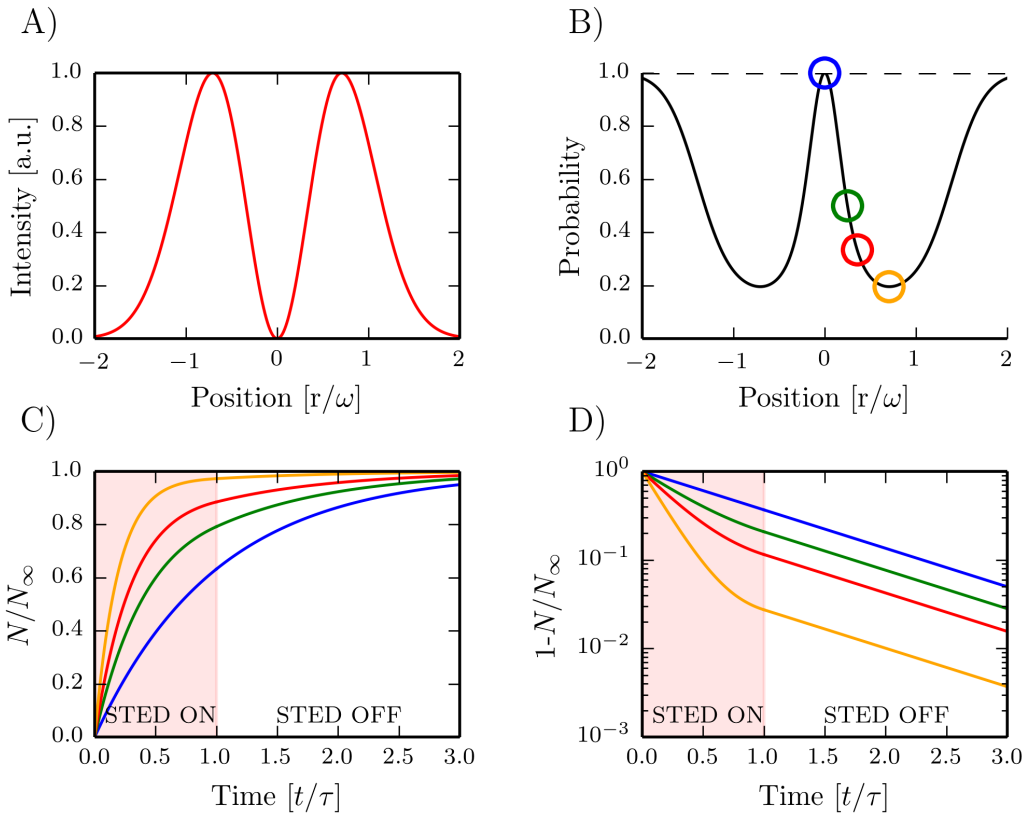

Figure 3.1: Fluorophore lifetimes in the presence of a stimulating beam. A) The intensity distribution for the stimulating beam. B) The probability of emitting in the fluorescent channel (solid) when a uniform field of excited fluorophores (dashed) are exposed to a STED beam with $t_S = \tau$ and $S = 23$ (Eq. 3.14). C) The number of fluorophores that have emitted via the spontaneous emission channel as a function of time, normalized by the total number of fluorophores that will emit in this channel ($N_\infty = N_F(t = \infty)$; Eq. 3.5). The different colors represent different locations along the STED beam corresponding to different probabilities of emitting via spontaneous emission (1, blue; 1/2, green; 1/3, red; 1/5, orange). These positions are circled in panel B. D) The fraction of fluorophores that will emit by spontaneous emission but have not yet done so at a given time. All distances are measured in units of spatial parameter of the STED beam, ω, and all times are measured in units of the unstimulated fluorophore lifetime, τ.

the spontaneous emission from the position of the central minimum of the STED beam ($r = 0$; the blue circle in Fig. 3.1 B) has been emitted, whereas 40% of the emission from position r_{max} (the orange circle in Fig. 3.1 B) has already arrived. Moreover, by the completion of the STED pulse, only 60%

of the emission from $r = 0$ while nearly all of the spontaneous emission emitted by fluorophores located at r_{max} has arrived. Thus, spontaneous emission from fluorophores located at regions of higher STED intensity arrive earlier on average than spontaneous emission from fluorophores exposed to smaller STED intensities, and it should be possible to better distinguish fluorophores located at the center of the STED beam from those located on the edges with time resolved measurements of the spontaneous emission.

3.3 STED resolution for pulses of finite duration

Before we discuss the use of temporal information to improve spatial resolution, it is first useful to determine the effect of pulses of finite duration on the effective PSF of a STED microscope. This section complements recent work by others [Leutenegger et al., 2010] in which a comprehensive analysis of STED depletion for pulses of finite duration in the presence of vibrational relaxation was conducted. However, for simplicity, we will continue to neglect vibrational relaxation here.

In the typical STED microscope, fluorophores are excited in a Gaussian profile and fluorescence emission is detected in a confocal configuration. This configuration produces a PSF well approximated by

$$PSF_C(r) \sim e^{-4r^2/\omega^2} \tag{3.11}$$

where ω corresponds to the 1/e waist of the electric field of the excitation beam. For simplicity, we use the same ω for both the STED beam and the confocal PSF though, in practice, the different wavelengths and initial beam sizes for both the excitation and stimulating beams will produce minor differences in ω. The amplitude of the PSF is set by the finite collection and detection efficiency of the optical setup. However, these properties are unaffected by the introduction of a STED beam and, thus, will not affect comparisons between the confocal PSF and the effective STED PSF, so we neglect finite detection efficiency here.

The final effective PSF of a STED microscope is the product of this confocal PSF with the depletion factor provided in Eq. 3.7 and illustrated in Fig. 3.1 B

$$\begin{aligned} PSF_{STED}(r) &= PSF_C(r)\eta_{STED}(r) \\ &= e^{-4r^2/\omega^2}\left(\frac{k}{k+\sigma I(r)} + \frac{\sigma I(r)}{k+\sigma I(r)}e^{-(k+\sigma I(r))t_S}\right). \end{aligned} \tag{3.12}$$

To understand the scaling of this PSF, it is useful to introduce dimensionless variables that allow the pulse duration to be varied without changing the total energy in the pulse

$$\alpha = t_S/\tau \text{ and } E(r) = \sigma I(r) t_S. \tag{3.13}$$

α sets the duration of the STED pulse while $E(r)$ determines the strength of the stimulated emission channel at position r, i.e. the energy density of the pulse, $I(r)t_S$, scaled by the cross-section for stimulated emission, σ. With these variables, the STED depletion factor becomes

$$\eta_{STED}(r) = \frac{\alpha}{\alpha + E(r)} + \frac{E(r)}{\alpha + E(r)}e^{-(\alpha+E(r))}. \tag{3.14}$$

The effective PSF for STED microscopy has been calculated previously [Harke et al., 2008] under the assumption of a STED pulse of negligible duration but fixed energy. Taking the infinitely short STED pulse limit, i.e. $\alpha \to 0$, we recover the previous depletion factor from Eq. 3.14 (equivalent to Eq. 2.19 in Chapter 2)

$$\lim_{\alpha\to 0} \eta_{STED}(r) = e^{-\sigma I(r)t_S} = e^{-E(r)}. \tag{3.15}$$

Comparison of these two expression reveals that for a given pulse energy the depletion produced by a pulse of longer duration is always less than the depletion provided by a pulse of shorter duration. Since less depletion will result in less squeezing of the final PSF, pulses of finite duration will degrade the resolution of the STED microscope. Thus, when vibrational relaxation

times are neglected, the best resolution for a given pulse energy will be for the pulse with the shortest duration. When vibrational relaxation times are included, it has been shown that a small but finite pulse duration produces the optimal resolution [Leutenegger et al., 2010] as discussed in Chapter 2 Section 2.4. Similar results are expected when re-excitation by the STED beam is considered.

3.4 Time-gated STED (T-STED) resolution

This loss in resolution may initially seem like a limitation to STED pulses of longer durations; however, Eq. 3.12 ignores the additional spatial information contained in the arrival times of the fluorescent photons (Fig. 3.1). To exploit this information, we propose that the fluorescence signal used to create the STED image should be time-gated. In other words, only photons arriving after a given time-window will be used to form the final image, as illustrated in Fig. 3.2 A. Assuming a time delay t_G, Eq. 3.5 provides the depletion factor for a time-gated STED (T-STED) measurement

$$\begin{aligned}\eta_{T-STED}(r;t_G) &= \lim_{t\to\infty}\frac{N_F(t)-N_F(t_G)}{n_0}\\ &= \frac{k}{k+\sigma I(r)}e^{-(k+\sigma I(r))t_G}+\frac{\sigma I(r)}{k+\sigma I(r)}e^{-(k+\sigma I(r))t_S}.\end{aligned} \tag{3.16}$$

Since fluorescence decay is a Markov process, arrival times are only modified during the duration of the STED pulse; thus, there is no benefit to time-gates longer than the STED pulse, and we restrict Eq. 3.16 to $t_G \leq t_S$. Equation 3.16 therefore reveals that the smallest value of $\eta_{T-STED}(r;t_G)$ and, thus, the smallest effective PSF for a given value of r occurs when the time-gate is equal to the STED pulse duration, i.e. $t_G = t_S$ in which case Eq. 3.16 simplifies significantly

$$\eta_{T-STED}(r;t_G=t_S) = e^{-kt_S}e^{-\sigma I(r)t_S}. \tag{3.17}$$

Remarkably, Eq. 3.17 differs from the factor derived in the infinitely short

pulse limit, Eq. 3.15, only in the term $exp(-kt_S)$. Since this term contains no spatial dependence, it will not affect the spatial extent of the effective PSF; thus, time-gating the fluorescence signal restores the maximum resolution derived in the infinitely-short pulse limit. The additional term, $exp(-kt_S)$, corresponds to the fraction of fluorophores that decay during the time-gate independent of their position. Rejection of these photons degrades the image brightness without changing the spatial resolution.

Figure 3.2 displays the factors $\eta_{STED}(r)$ and $\eta_{T-STED}(r; t_G = t_S)$ for the example considered in Fig. 3.1. By applying a time-gate equal to the STED pulse duration, the "depleted" region observed in Fig. 3.1 B (black) can be significantly increased (red, dotted). To better compare the increase in the depletion region, Fig. 3.2 B also plots this depletion factor without the $exp(-kt_S)$ prefactor. For this particular example, time-gating lowers the amount of accepted spontaneous emission nearly 40-fold from fluorophores located at r_{max}. This additional rejection results in a tighter effective PSF, as illustrated in Fig. 3.2 C. The 2-fold improvement in resolution afforded by the depletion of the spontaneous decay channel is increased to 2.5-fold simply by rejecting the spontaneous emission that arrives during the duration of the STED pulse.

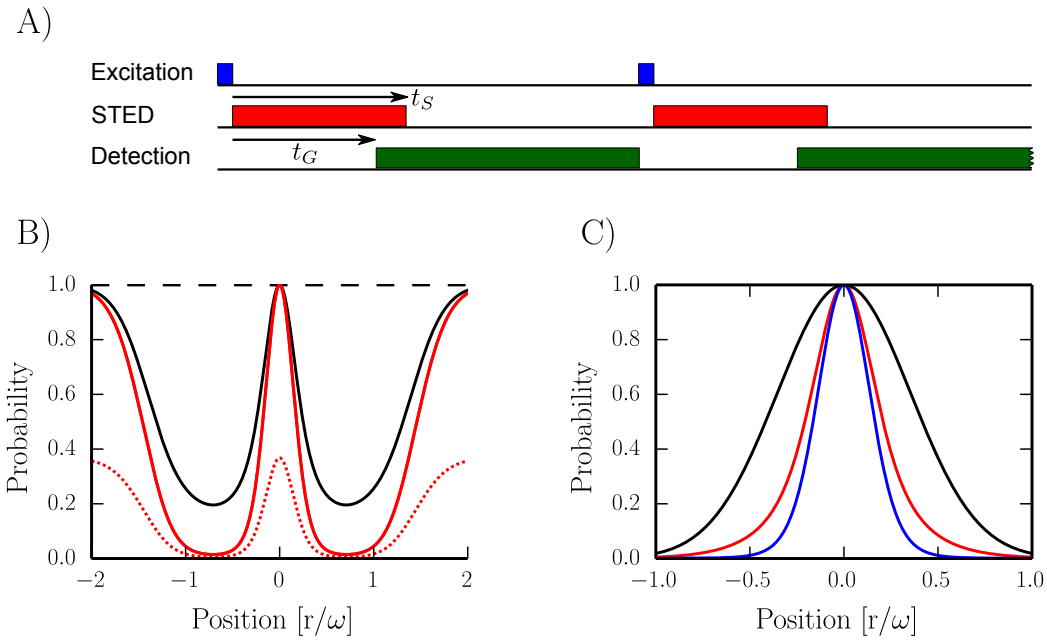

Figure 3.2: Improving spatial resolution with time-gating. A) Timing diagram for pulsed STED with time-gated detection. Immediately following an excitation pulse of negligible duration (blue), a STED pulse of duration t_S begins (red). The final image is created from the spontaneous emission that arrives during a time window starting t_G after the completion of one excitation pulse and lasting until the beginning of the next (green). B) The probability of emitting via normal fluorescence as a function of position (black) when a uniform field of excited fluorophores (dashed black) are exposed to the pulsed STED beam described in Fig 3.1. The probability of emitting via spontaneous emission after the STED pulse has completed (red, dotted), and this probability corrected for the decrease in image brightness (red, solid). C) The effective PSFs for confocal detection (black), normal STED microscopy (red), or time-gated STED microscopy (blue). Probabilities and PSF were calculated with a STED strength sufficient to produce a 2-fold decrease in the FWHM of the effective PSF compared to the confocal PSF and a STED pulse duration equal to the unstimulated fluorophore lifetime, i.e. $S = 23$ and $t_S = \tau$. All distances are measured in units of the 1/e waist of the electric field of the excitation beam. The T-STED PSF in panel C has been corrected for the decrease in image brightness.

3.5 T-STED resolution scaling

To illustrate how the resolution of a pulsed STED measurement is affected by pulses of finite duration, Fig. 3.3 A plots the N-fold decrease in the FWHM of the effective PSF relative to the confocal FWHM as a function of pulse

energy for different ratios of pulse duration to un-stimulated fluorophore lifetime ($\alpha = t_S/\tau$). As has been determined previously, the FWHM of the effective PSF decreases roughly as the square-root of the pulse energy, i.e. STED strength [Harke et al., 2008]. For increased STED pulse duration (i.e. increasing α) the effective PSF shows a similar dependence with STED strength, however, the resolving power of the STED instrument is clearly decreased.

To judge the benefit of time-gating in a pulsed configuration, we determine the percent decrease in the FWHM with time-gating relative to a measurement in which no time-gating is applied for a given STED strength and pulse duration. Figure 3.3 B illustrates that as the STED pulse strength is increased the benefit provided by time-gating also increases though this benefit saturates for large STED strengths. Figure 3.3 C demonstrates that the increase in resolution provided by T-STED also increases with pulse duration with no apparent saturation for long pulses.

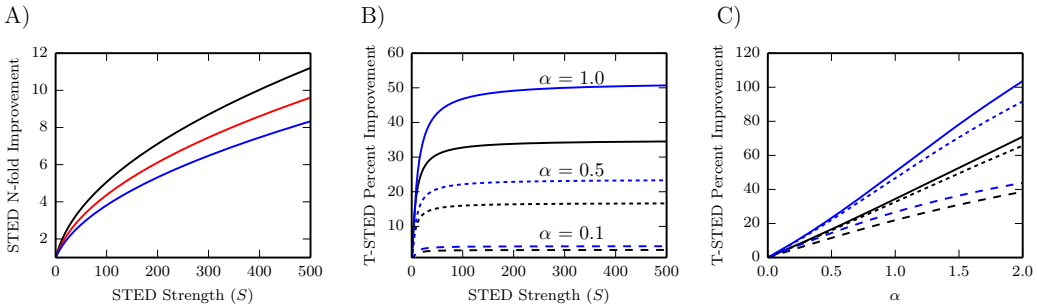

Figure 3.3: T-STED resolution for pulsed STED. A) The N-fold increase in the resolving power of a STED microscope over that of a confocal microscope as a function of the strength of the STED beam, S. Different pulse durations are plotted in different colors (instant; black; 0.5τ, red; τ, blue). Increase in resolving power is judged by the relative decrease of the FWHM of the effective PSF from that of the confocal PSF. B) T-STED resolution improvement over regular STED microscopy judged by the decrease in either the FWHM (black) or the FWQM (blue) for different STED beam strengths. Different pulsed durations are plotted ($\alpha = 0.1$, large dash; $\alpha = 0.5$; small dash; and $\alpha = 1.0$, solid.) C) Resolution improvement of T-STED over pulsed STED for different α determined with the FWHM (black) or the FWQM (blue). Different STED beam strengths are plotted corresponding to the STED strength required to produce a 2-fold (large dash,) 5-fold (small dash,) or 10-fold (solid) improvement in the FWHM with an instantaneous pulse (black trace in panel A). FWHM and FWQM values were calculated numerically from Eq. 3.12.

Time-gating is a non-linear process; thus, the effect of time-gating will not be a simple rescaling of the spatial extent of the PSF. Rather, the PSF will change shape, with different regions being rescaled to different extents. To estimate this change in the shape, Fig. 3.3 B and 3.3 C also plot the percent improvement in the effective width of the PSF at the full-width-at-quarter-maximum (FWQM). For all values of the total pulse energy and α, the improvement in the FWQM is always larger than that of the FWHM. Taken together, these results indicate that in addition to a general decrease in the spatial extent of the effective PSF, T-STED also provides a proportionally larger decrease in the spatial extent of the "tails" of the PSF. Thus, time-gating produces a "sharper" PSF.

To supplement the numerical results in Fig. 3.3, we also derive an analytical approximation to the waist of the PSF as a function of the experimental

parameters, e.g. pulse duration, fluorophore lifetime, and time-gate. We assume that the final PSF is well-approximated by a Gaussian, $\exp(-r^2/\omega_{eff}^2)$, with effective waist, ω_{eff}, and expand the natural logarithm of Eq. 3.17 in a Taylor series around $r = 0$. The coefficient of the second order term determines ω_{eff}. We find that the effective beam waist of the T-STED PSF is

$$\omega_{\mathit{eff}}/\omega = \left(4 + S\left(\frac{t_G}{t_S} + \frac{\tau}{t_S}\left(1 - e^{-\frac{t_S}{\tau}\left(1-\frac{t_G}{t_S}\right)}\right)\right)\right)^{-1/2}. \tag{3.18}$$

The initial factor of 4 originates from the distinction between the waist of the confocal PSF and that of the electric field of the excitation beam. Equation 3.18 simplifies in the absence of the time-gate, yielding

$$\omega_{\mathit{eff}}/\omega = \left(4 + S\frac{\tau}{t_S}(1 - e^{-t_S/\tau})\right)^{-1/2}. \tag{3.19}$$

Either in the limit of an infinitely short STED pulse (with constant STED strength) or of a time-gate equal to the STED pulse duration, Eq. 3.18 produces the inverse square-root dependence on the STED pulse energy derived previously [Harke et al., 2008]

$$\omega_{\mathit{eff}}/\omega = (4 + S)^{-1/2} \tag{3.20}$$

Comparison of Eqs. 3.19 and 3.20 reveals that the effect of pulses of finite duration is well approximated by decreasing the total STED strength, S, by $\frac{\tau}{t_S}(1 - e^{-t_S/\tau})$. Willig et al. [2007] have measured that increasing the STED pulse duration from 200 ps to an effective pulse of $\sim$ 13 ns with a 3.5 ns fluorophore lifetime requires a $\sim$3.6-fold increase in STED strength to produce the same depletion in the absence of time-gating. Under their experimental conditions, Eq. 3.19 predicts a ratio of STED strengths of 3.7, in excellent agreement with these measurements.

3.6 T-STED resolution with CW STED beams: theoretically unbounded resolution with finite laser power

In the above discussion, we considered pulsed STED beams; however, STED can also be accomplished with CW beams [Willig et al., 2007]. Here we expand our discussion to include time-gating with a CW STED source. We assume that the excitation occurs via a pulse with negligible duration and a repetition period, t_E, much larger than the unstimulated fluorophore lifetime, i.e. $t_E \gg \tau$. The temporal dynamics for this situation can be derived from the results for a pulsed system, Eq. 3.5 Section 3.1, in the limit that $t \ll t_S$ (i.e. $t_s \to \infty$). In this case, the number of fluorescent photons arriving as a function of time is

$$N_F(r,t) = n_0 \frac{k}{k+\sigma I(r)} \left(1 - e^{-(k+\sigma I(r))t}\right) \tag{3.21}$$

and the total number of fluorescent photons is

$$\lim_{t\to\infty} N_F(r,t) = n_0 \frac{k}{k+\sigma I(r)} \tag{3.22}$$

The spatial dependence in the choice of the decay channel, Eq. 3.22, is what provides the improved resolution in a previous demonstration of CW STED [Willig et al., 2007]. To exploit the additional spatial information encoded in the arrival times, we again propose that the fluorescence signal be time-gated. Fluorescence is collected starting a duration t_G after the completion of the excitation pulse and continues until the beginning of the next excitation pulse. See Fig. 3.4 A. Under the assumption that the excitation pulse repetition period is much larger than the fluorophore lifetime, i.e. $t_E \gg \tau$, Eq. 3.21 produces the time-gated CW STED depletion factor

$$\eta_{CW\ T-STED}(r;t_G) = \frac{N_F(r,\infty) - N_F(r,t_G)}{n_0} = \frac{k}{k+\sigma I(r)} e^{-kt_G} e^{-\sigma I(r) t_G}. \tag{3.23}$$

As was observed for the pulsed STED situation above, the final STED depletion factor has both a spatially dependent and independent component. The spatially independent portion, $\exp(-kt_G)$ represents the decrease in image brightness that occurs with increasing time-gates. Since this factor applies for all locations, it will not affect the spatial extent of the effective PSF of the microscope. The $I(r)$ terms in both the prefactor and the exponent, on the other hand, will improve the spatial resolution.

Figure 3.4 B illustrates the effect of time-gating with a CW STED beam on the effective PSF of the microscope. When a CW STED beam is applied without time-gating, the width of the effective PSF drops; however, the peak amplitude of the PSF - a measure of the probability of detecting emitted photons - remains constant. Thus, the brightness of a point-emitter will be unchanged. However, when a time-gate is applied, both the width and the maximum amplitude of the effective PSF decrease; thus, a point emitter will appear both sharper and dimmer. To better illustrate the decrease in the spatial extent of the PSF, Fig. 3.4 C plots these same PSFs but normalized to the maximum amplitude. Figures 3.4 D and 3.4 E quantify the decrease in the FWHM with different CW-STED parameters and reveal that increasing either the STED strength or the ratio of the time-gate to the fluorophore lifetime increases resolution.

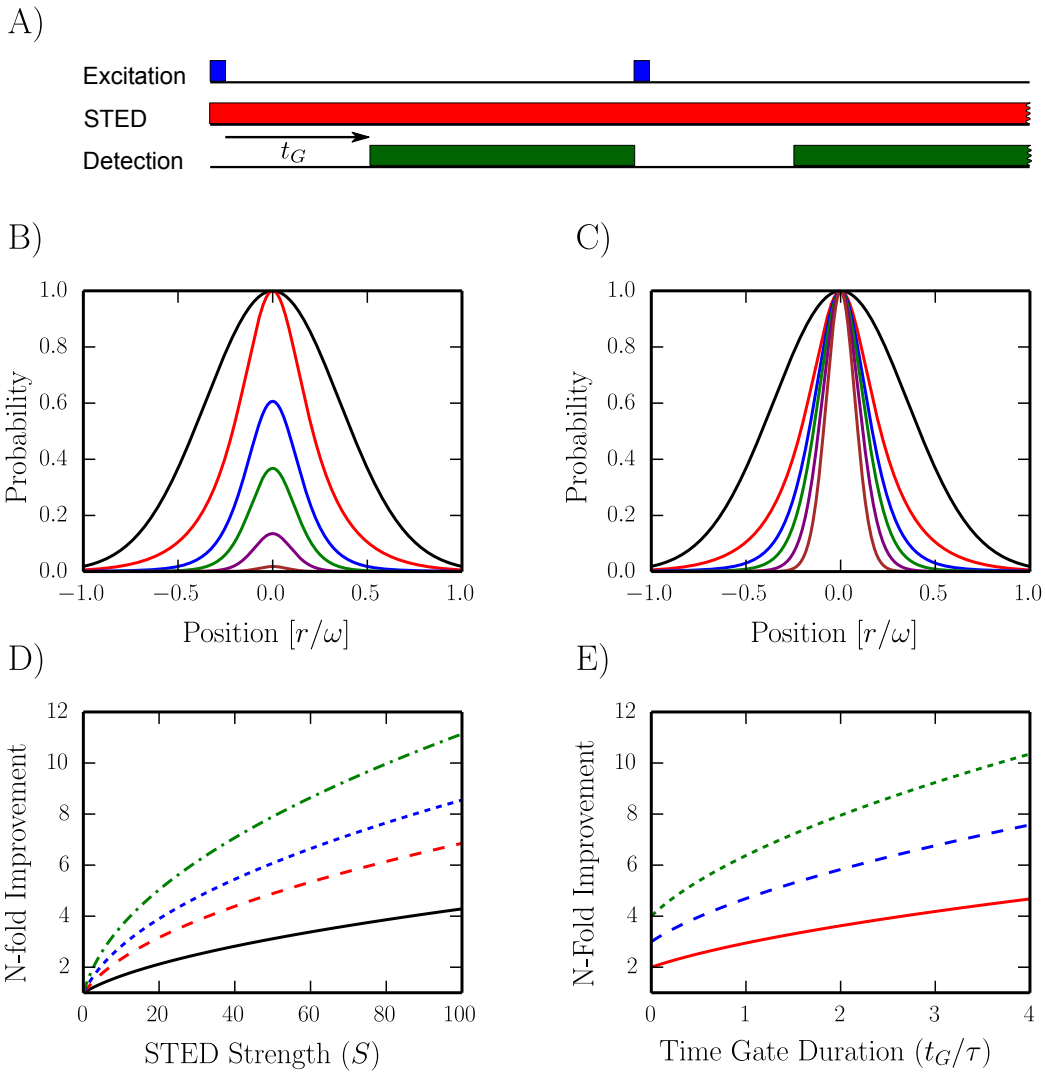

Figure 3.4: CW T-STED. A) Timing diagram for time-gating with a CW STED beam. B) The effective PSF for different CW T-STED parameters. Plotted are the confocal PSF (black); the effective PSF with a CW STED beam with STED power sufficient to reduce the FWHM to 1/2 that of the confocal PSF (red; $S = \sigma\gamma\omega^2\tau = 16.5$); the same STED beam with $t_G = 0.5\tau$ (blue); $t_G = \tau$ (green); $t_G = 2\tau$ (purple); and $t_G = 4\tau$ (brown). C) The effective PSF corrected for the decrease in image brightness. The color scheme is the same as in panel B. D) The N-fold improvement in the FWHM of the effective PSF with respect to the confocal PSF versus strength of the STED beam. $t_G = 0, 1, 2, 4\tau$ are plotted as solid black, dashed red, dashed blue, and dashed green respectively. E) The N-fold improvement in the FWHM due to CW T-STED as compared to the confocal PSF versus time-gate duration for different STED beam strengths. Red, blue, and green correspond to STED strengths that decrease the FWHM by 2, 3, and 4-fold in the absence of a time-gate. All distances are measured in units of the 1/e waist of the electric field of the excitation beam. FWHM values were calculated numerically from Eqs. 3.11 and 3.23.

As above, we complement the numerical results in Fig. 3.4 with an analytical estimate for the effective waist of a CW T-STED PSF. We Taylor expand the natural logarithm of the product of the CW T-STED depletion factor, Eq. 3.23, with the confocal PSF and use the second order coefficient to derive the effective waist

$$\omega_{\mathit{eff}}/\omega = (4 + \sigma\gamma\omega^2\tau(1 + t_G/\tau))^{-1/2} = (4 + S'(1 + t_G/\tau))^{-1/2} \qquad (3.24)$$

where we slightly modify the STED strength by replacing the pulse duration, undefined for a CW STED beam, with the unstimulated fluorophore lifetime, $S' = \sigma\gamma\omega^2\tau$.

Equation 3.24 bears a striking similarity to the improvement in spatial resolution derived previously [Harke et al., 2008] and above, in the limit of an infinitesimally short pulse, Eq. 3.20. The only distinction is that the effective STED strength is increased by the factor $(1 + t_G/\tau)$ in Eq. 3.24. Remarkably, the effective STED strength scales linearly with the time-gate duration for a CW T-STED measurement. Since this duration is bounded only by the repetition period of the excitation beam, which can be made as large as desired, the STED strength can be increased arbitrarily simply by increasing the time-gate, without increasing the power of the stimulating beam. In other words, the resolution of a time-gated STED measurement with a CW STED beam is theoretically unbounded for finite laser power. Of course this increase in resolution comes at a price. The prefactor $\exp(-kt_G)$ implies that images collected with time-gates of increasing duration will be exponentially dimmer.

This result is in sharp contrast to the results derived for a pulsed STED situation, in which time-gating cannot increase the resolution beyond the resolution achieved with an infinitesimally short pulse with the same total energy. The discrepancy between the performance of a pulsed measurement and a CW measurement highlights the physical origin of the increase in resolution: the effective energy of the STED beam. In a pulsed measurement, this energy is fixed by the duration of the pulse, time-gating can only use this

energy more effectively, not increase it; thus, resolution is bounded by the resolution achieved with an infinitesimally short pulse. However, in a CW measurement the effective STED energy can be increased simply by integrating the STED beam over larger time-gates, producing increased depletion and increased spatial resolution.

3.7 Discussion and conclusions

In this chapter we solve a simple kinetic model for the temporal dynamics of excited fluorophores in the presence of a spatially varying stimulating beam of variable duration and demonstrate that spatial information is contained in the arrival times of the spontaneous emission. To extract this extra information, we propose that the fluorescence signal should be time-gated, and we derive the increase in spatial resolution provided by time-gating for both pulsed and CW STED beams. In both cases, time-gating provides higher resolution but dimmer images. These findings have since been confirmed by experiments [Vicidomini et al., 2011, 2013a,b, Göttfert et al., 2013].

When might T-STED be a useful alternative to a STED measurement? The lifetimes of the fluorophores useful for STED measurements range from 100s of ps to a few ns. STED pulse durations, on the other hand, range from 10s of ps [Dyba and Hell, 2002] to $\sim$ 1 ns [Rankin et al., 2008, Göttfert et al., 2013]. Thus, for pulsed STED measurements, the range of α values is large, $\sim$ 0.01 - 10. For measurements with small α values, < 0.5, the resolution enhancement provided by time-gating will likely be negligible. In fact, the improvement may be so modest that it is not measurable - an observation that may explain why a change in STED depletion as a function of pulse duration was not observed in a previous study [Dyba and Hell, 2003]. However, for larger α values, the improvement in resolution is significant, and these measurements will likely benefit from time-gating. In a recent study, Vicidomini et al. [2013b] confirm the theory by imaging with time-gating in pulsed T-STED and CW T-STED mode. Interestingly, the dye Atto 647N with a lifetime (according to the datasheet of the manufacturer) of 3.5 ns exhibited a strong short lifetime component of 0.3 ns when labeling antibodies against

microtubuli with two or three dye molecules per antibody (intensity-weighted lifetime of 1.9 ns). Under these conditions, even when using a relatively short STED pulse duration of $\sim$ 300 ps, the resolution of the microscope improved significantly when using time-gating. The short lifetime component observed in those measurements can be attributed to concentration-quenching of the dye when the degree of labeling is high [Luchowski et al., 2008]. Thus, labeling conditions can render a time-gated detection useful even in a pulsed scheme using short depletion pulses.

Interestingly, the benefits of time-gating in a pulsed STED measurement are not limited to improved resolution. As has been widely recognized, time-gating can remove stray scattered light from the STED beam not removed by filters, decreasing background noise significantly in some situations [Vicidomini et al., 2013b]. However, beyond this concern, we have now revealed that pulse durations can be increased, with no loss in resolution, when time-gating is applied. The ability to spread the pulse power over longer durations, decreasing the instantaneous intensity of the pulse, may allow experimentalists to avoid known issues such as inefficient depletion during vibrational relaxation [Leutenegger et al., 2010], STED intensity-dependent photobleaching [Dyba and Hell, 2003, Göttfert et al., 2013] as well as polarization effects and synchronization jitter in a pulsed scheme [Vicidomini et al., 2013a]. STED measurements are often limited by the photostability of current dyes; thus, the ability to reduce photobleaching through longer pulses with no loss in resolution is an important additional benefit of T-STED.

The major benefit of T-STED with a CW laser source will likely be the ability to increase resolution significantly without the use of additional laser power. However, it is important to note that while, in theory, the resolution of a CW T-STED measurement is unbounded. In practice, there will likely be a maximum resolution given the specific STED laser, the fluorophore lifetime and photostability, and the background noise of the measurement. Image resolution increases slowly with the time-gate duration—as the square-root—while the brightness decreases exponentially. Thus, there will be a maximum time-gate beyond which the image will not be bright enough to be distinguished from background noise, and this maximum time-

gate will set the maximum image resolution. To surpass this practical limit additional laser power will be needed. Alternatively, our analysis reveals that an increase in the resolution can also be produced by using fluorophores with longer lifetimes. This observation makes color centers in diamond all the more exciting as STED probes since these fluorophores have particularly long lifetimes, > 10 ns [Rittweger et al., 2009, Han et al., 2009, Arroyo-Camejo et al., 2013]. Thus, through the simple addition of a time-gate, it may be possible to significantly increase the 6 nm resolution recently reported with CW STED imaging of color centers [Rittweger et al., 2009].

The practical implementation of a time-gated detection is best realized using time correlated photon counting hardware [Vicidomini et al., 2011]. This enables the user to set the effective time-gate after the image is recorded allowing to tune in the best balance between better resolution (longer t_G) and image brightness (shorter t_G). This is especially useful in the case of CW T-STED in which resolution is increased for time-gates longer than the lifetime of the fluorophore used.

In a pulsed T-STED scheme, using common lasers with a pulse length shorter than the fluorophore's lifetime, the time-gate is usually set right after the depletion pulse has ended to restore resolution lost due to the spread-out depletion pulse as dictated by Eq. 3.17 [Göttfert et al., 2013].

It was long thought that the resolution of far-field optics was fundamentally limited by diffraction, but it is now clear that a variety of techniques can embed additional spatial information in the optical measurement and leverage this additional information to image spatial features well below the diffraction limit. Here, we show that minor differences in fluorescence lifetimes, created by differences in the local intensity of the STED beam, can be amplified into measureable differences in arrival times, revealing that the last photons to arrive carry the most spatial information. CW lasers used as depletion sources represent a cheap and robust alternative to pulsed laser systems albeit at the cost of reduced resolution for the same average power of a pulsed setup. The use of a time-gated detection as proposed in this chapter will likely boost its use in the scientific community. Recent practical implementations of this scheme even in commercial instruments (by Abbe-

rior Instruments GmbH, PicoQuant GmbH and Leica Microsystems GmbH) support our findings and underline the importance of it.

Chapter 4

Microscope design

In the following chapter the design and implementation of the stimulated emission depletion (STED) microscope built as part of this thesis is described. The design allows simultaneous three-dimensional super-resolution imaging in two colors. A super-continuum laser source is used to provide all spectral bands necessary for excitation and efficient depletion to achieve a lateral and axial resolution of ~ 35 nm and ~ 90 nm, respectively. The system's performance is characterized by imaging colloidal particles to assess the shape of the depletion patterns. Furthermore, single fluorescent molecules are imaged to measure resolution in three dimensions. Important design considerations and measurements are described to achieve an optimally working setup. Parts of this chapter have been published in the journal Optics Express under the title *Simultaneous dual-color 3D STED microscopy* [Osseforth et al., 2014]. Due to the complexity of this setup, details on how to build it from scratch and on daily alignment procedures are presented in the appendix of this manuscript.

4.1 Spectral considerations in a dual-color STED setup

Different routes can be taken when expanding a single-color STED microscope to a two-color setup. At the time of planning the setup described in this chapter, the most promising approach was to incorporate a sepa-

rate depletion path for each fluorescence channel. This allows to tune the depletion wavelength to its optimum value for the fluorophore used in the respective channel which in turn ensures best resolution with the limited laser power at hand. An alternative approach is incorporated in a commercially available STED microscope sold by Leica Microsystems GmbH [Leica Microsystems CMS GmbH, 2011, Schmidt et al., 2008]. Here, two fluorophores of which one exhibits a large Stokes shift are depleted with a single beam. While this takes some complexity out of the setup the user is restricted to very few dyes. The presented setup ensures flexibility in choosing the most stable fluorophores for the experiment.

When expanding a one-color STED microscope to a dual-color setup an important peculiarity has to be taken into account. In a conventional dual-color confocal fluorescence microscope one would spectrally separate the two detection channels as much as possible in order to minimize spectral crosstalk. In the case of a STED microscope this causes additional problems. Special care has to be taken to prevent overlap of the depletion band of the short wavelength channel (channel 1) with the absorption spectrum of the dye used in the second, higher wavelength channel (channel 2). If those spectra do coincide, one has to subsequently scan first channel 2 and then channel 1, to avoid bleaching of the fluorophores of channel 2 [Meyer et al., 2008]. This early dual-color STED implementation essentially prevents optical sectioning/repetitive scanning in two colors as during a single scan the fluorophores of channel 2 are bleached by the depletion beam of channel 1. Although somewhat counterintuitive, the performance of a dual-channel STED microscope can be significantly improved by bringing the spectral bands of the two fluorophores as close together as possible while still preventing excessive crosstalk. This approach moves the depletion band out of the absorption spectrum thus allowing simultaneous imaging of two different fluorophores over multiple scans [Neumann et al., 2010].

The microscope discussed in this thesis is based on the latter design. A suitable set of dyes was found to be Atto 590 and Atto 647N, fluorophores which have been known for its stability in STED experiments [Wildanger et al., 2009, Meyer et al., 2008]. A benefit from using these deep red dyes is

the relatively high depletion wavelengths used which minimizes the excitation of autofluorescence in biological samples [Mansfield et al., 2005, Berlier et al., 2003]. Furthermore, the resulting low photon energy of the depletion beams helps keeping excitation of the fluorophores to higher states to a minimum thus reducing excessive photobleaching. The setup was designed to efficiently excite and detect Atto 590/594 or its respective Alexa counterpart Alexa 594 in channel 1 and Atto 647N or Alexa 647 in channel 2. Due to availability as ready-to-use constructs such as labeled secondary antibodies, the dye combination Atto 594 and Atto 647N was most commonly used in this study for the imaging of biological objects (Chapter 5). The absorption and emission spectra of these dyes partially overlap (Fig. 4.1).

While a careful choice of dichroic mirrors and filters will help keep crosstalk between the detection channels low, further reduction of crosstalk is required. To this end, a synchronized time-gated detection was built which efficiently removes residual spectral crosstalk (Section 4.2.3).

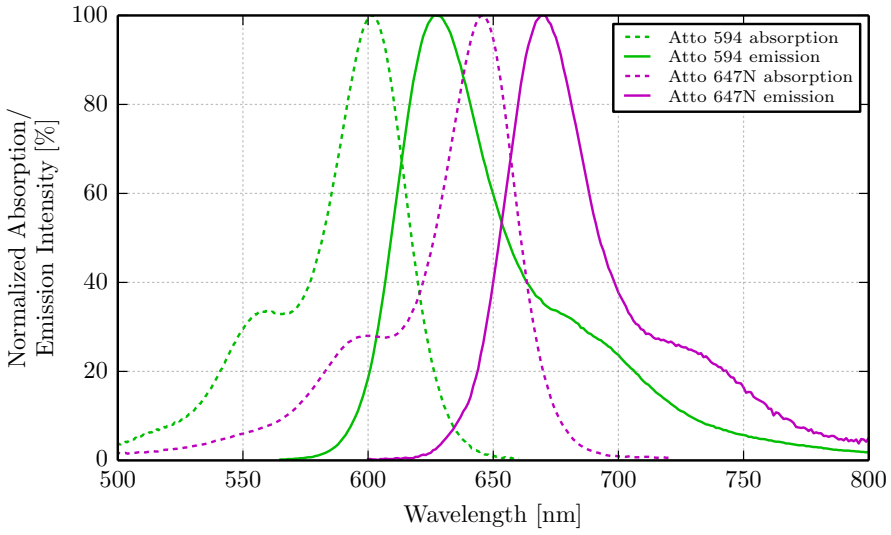

Figure 4.1: Absorption and emission spectra for the dyes Atto 594 and Atto 647N used in this study (taken from data sheet by Atto-Tec GmbH). Spectral overlap of the emission spectra is reduced by suitable filters and a synchronized, time-gated detection (Section 4.2.3).

4.2 Dual-color 3D STED setup

4.2.1 Generating beams for excitation and depletion

The dual-color 3D STED microscope uses a single, unpolarized super-continuum laser source (SC-450-PP-HE, Fianium Ltd., Southampton, UK) to deliver all necessary spectral bands for the various beam paths at high enough power spectral density (Fig. 4.2). The laser has a repetition rate of $\sim$ 1 MHz. As a result, due to the $\sim$ 1 μs interval between pulses, excitable metastable dark states can relax efficiently ensuring minimal photobleaching [Wildanger et al., 2008]. The pulse length is $\sim$ 166 ps which allows for efficient depletion without the need for time-gated detection (Chapter 3, T-STED/G-STED, [Moffitt et al., 2011, Vicidomini et al., 2011]) to maintain best resolution at a given power.

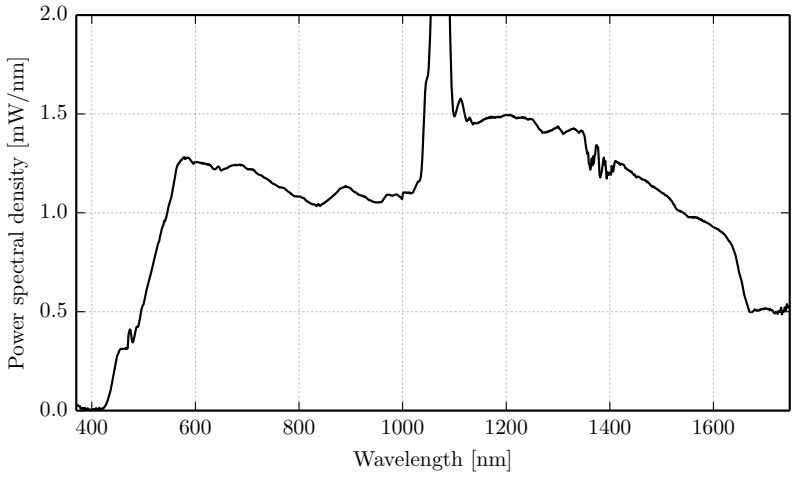

Figure 4.2: Power spectral density of the laser source SC-450-PP-HE by Fianium Ltd. (data from Fianium Ltd.). In the relevant part of the spectrum from $\sim$ 550 nm to $\sim$ 800 nm the power spectral density is above 1 mW/nm.

The design of the dual-color 3D STED microscope can be logically divided into two parts, the *front end*, which refers to the part of the microscope from the laser source up to the single-mode fiber couplers (Fig. 4.3) and the *back end*, which denotes the section from the single-mode fiber collimators to the objective lens as well as the detection (Fig 4.4). The design of the front

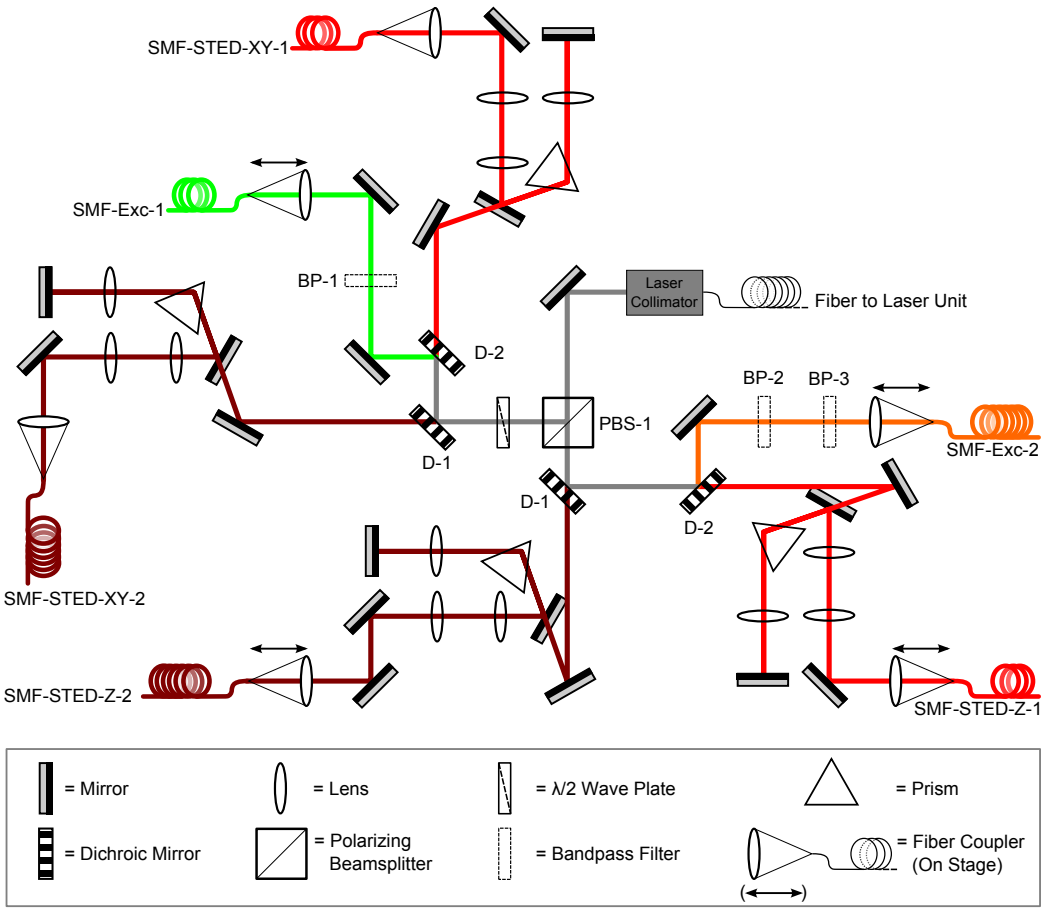

Figure 4.3: Detailed schematic depicting the front end of the microscope, i.e. the beam paths from the laser output collimator to the fiber couplers. The framed inset refers to the components sketched in the figure. Naming scheme of the labeled components follows the description in the main text. Gray: multiple wavelengths present; green: excitation path channel 1; red: depletion beams for channel 1; orange: excitation path channel 2; dark red: depletion paths for channel 2. Note that the mirror in front of each prism is positioned below the common beam height and thus permits transmission of the incoming beam but reflects the reflected beam from the monochromator due to its lower beam height. Please refer to Appendix B.1 for further details on the monochromators.

end is described in this section while the back end will be the topic of the following section. The component abbreviations used in the following are summarized in Table 4.3 at the end of the next section. A practical guide to the alignment of the front end is given in Appendix B.

The unpolarized laser output is divided into vertical and horizontal po-

larization by the use of a polarizing beam splitter (PBS-1). Each path is further split by a first dichroic mirror, which is centered at 730 nm (D-1) transmitting the spectrum necessary for the longer wavelength depletion beams (XY STED-2 and Z STED-2 beam). The reflected light of D-1 is subsequently split by another dichroic mirror (D-2) into the spectral range necessary for the depletion beams of the shorter wavelength STED beams (channel 1) in transmission and the two excitation beams in reflection. The respective spectral ranges for the depletion beams are further fine-tuned to the correct spectral band for the corresponding fluorophore by means of prism-based monochromators. The monochromators are explained in detail in Appendix B.1. The spectral range typically used for the depletion beams was $\sim$ 715 nm $\pm$ 10 nm and $\sim$ 750 nm $\pm$ 10 nm for channel 1 and 2, respectively. The excitation wavelength of the first channel (568 nm) is selected by a single bandpass filter (BP-1). A pair of filters is needed to correctly select the excitation wavelength of channel 2. BP-3 ensures a narrow excitation at 647 nm but passes light of wavelength below 510 nm. The latter residual transmission is blocked by BP-2. All filters and beamsplitters used in the setup are summarized in Table 4.3.

All six beams are coupled into polarization-maintaining single-mode fibers (SMF-x, Table 4.2) using wavelength selected lenses (Table 4.1) for the purpose of spatial cleaning and mechanic decoupling from the rest of the microscope. The use of compact fiber couplers allows a precise mechanical orientation of the fiber's slow axis relative to the polarization axis of the incoming beams. Correct orientation is crucial to maintain linear polarization at the fiber output and thus optimal performance of the microscope due to following polarizing elements. Each beam path further comprises a bistable shutter to selectively activate beams (Appendix C.2) and a servo-based intensity regulation device (Appendix C.3) both placed before each fiber coupler. The latter consists of a laser-cut spiral-shaped blade which can be rotated into the beam to block of the beam (custom-made, Cutworks GmbH). The position is set as a 8-bit parameter resulting in 255 steps to go from fully blocked to full transmission. The aberrated wavefront of the partially blocked beam is cleaned up by subsequently coupling the beam into

the aforementioned single mode fibers. The shutter and the servo-controller are both controlled remotely via custom-written software (LabView, National Instruments, Appendix C.5).

Table 4.1: Fiber couplers and fiber collimators used in the 3D dual-channel STED microscope. All parts from Schäfter & Kirchhoff GmbH, Germany unless stated otherwise

Beam	Fiber Coupler	Fiber Collimator
Excitation-1	60SMS-1-0-A18-01	60FC-T-0-M40-04
Excitation-2	60SMS-1-0-M12-33	60FC-T-0-M40-54
STED-XY-1	60SMS-1-0-A15-02	60FC-T-0-M40-54
STED-Z-1	60FC-0-M15-26	AC254-045-B by Thorlabs, USA
STED-XY-2	60SMS-1-0-M12-NIR-10	60FC-T-0-M40-54
STED-Z-2	60FC-0-M15-26	AC254-050-B by Thorlabs, USA

Table 4.2: Fibers used in the 3D dual-channel STED microscope. All parts from Schäfter & Kirchhoff GmbH, Germany

Beam	Fiber
Excitation-1	PMC-630-4,2-NA010-3-OPC-200-P
Excitation-2	PMC-630-4,4-NA011-3-OPC-2050-P
STED-XY-1	PMC-630-4,6-NA011-3-OPC-150P
STED-Z-1	PMC-630-4,6-NA011-3-OPC-150P
STED-XY-2	PMC-780-4,8-NA013-3-OPC-2000-P
STED-Z-2	PMC-780-4,8-NA013-3-OPC-2000-P

4.2.2 Beam co-alignment and detection

This section describes the back end of the microscope starting with the fiber collimators including everything up to the objective lens and the detection (Fig. 4.4). The component abbreviations used in this section are listed in Table 4.3 at the end of this section. A practical guide to the alignment of the back end is given in Appendix B.2.

The spatial co-alignment of the six beams is done using polarizing beam splitters and dichroic mirrors. The beam paths of the depletion beams are described here in detail exemplary for channel 1 but also apply to channel 2.

The depletion beam STED-XY-1 is sent through a vortex phase plate (VPP-STED-XY-1) to imprint the phase pattern necessary to yield the Laguerre-Gaussian LG01 mode in the focal plane. This light pattern is used

to increase the lateral resolution of the microscope in x and y. To ensure perfect circular polarization of this beam it passes through a combination of a $\lambda/2$ retarder ($\lambda/2$-WP) and a custom-selected achromatic $\lambda/4$ wave-plate ($\lambda/4$-WP) before being directed into a high NA, 100x oil immersion objective (HCX PL APO 100x/1.40-0.70 oil CS, Leica, Germany) by the use of a silver mirror to preserve the state of polarization. To obtain optimal circular polarization for the STED-XY beams, a homebuilt polarization analyzer is inserted between the silver mirror and the objective lens. It consists of a rotating polarizer and a photodiode which detects the modulated light intensity that is transmitted through the polarizer (Appendix C.1). The signal is analyzed by custom-written software (LabView, National Instruments, USA). The observed sine modulation is reduced to a minimum by adjusting the angle of the fast axis of the two retarders one at a time in an iterative fashion. The fine-tuning of the circular polarization is crucial to the performance of the STED microscope. Due to the achromatic retarders used a degree of circular polarization can be obtained to yield point spread functions with a very low central intensity minimum on the order of a percent of the maximum intensity in both channels.

In order to deplete the excited state also along the axial direction a different phase mask is introduced into the STED-Z-1 beam (CPP-STED-Z-1). The mask consists of a sputtered MgF_2 cylinder in the center [Wildanger et al., 2009] with a thickness which results in a phase shift of π. The size of the cylinder is chosen such that half of the total electric field amplitude of the beam is phase shifted [Klar et al., 2000]. When focused, the beam will show destructive interference in the focal point and two prominent axial side lobes above and below the focal plane. Similarly to the effect of the STED-XY depletion beam on the resolution in x and y, the STED-Z beam will lead to an enhanced resolution along the optical axis, z. Note that the interference pattern also shows a ring of light resembling the donut pattern of the STED-XY beams. This also increases resolution in x and y but to a much lesser extend than the dedicated STED-XY beam. The STED-Z-1 beam is superimposed onto the STED-XY-1 beam by the use of a polarizing beam splitter (PBS-2, termed STED-XYZ-1). In contrast to the STED-XY beams,

the polarization state is not as important for the STED-Z beams. However, to efficiently deplete the excited state of randomly oriented molecules in the sample it should also be circularly polarized. All STED beams, i.e. STED-XYZ-1 and STED-XYZ-2, are subsequently spatially combined by a dichroic mirror (D-1). Moreover, the two excitation beams are coupled into the optical path by a pair of dichroic mirrors, respectively (D-2 and D-4) and all beams are combined using dichroic mirror D-3 (D-3). In order to minimize wave front distortions D-1 to D-4 are all on 5 mm thick substrates with a flatness of $\lambda/10$.

The fluorescence light is collected by the same microscope objective and, after passing D-3 and D-4, it is split into the two fluorescence channels by another dichroic (D-5) and subsequently filtered by a pair of emission filters (EF-1 and EF-2). The respective fluorescence light is focused onto a multimode fiber which serves as a confocal pinhole corresponding to ~ 1.16 Airy units to reject out-of-focus light (MMF, M31L01, Thorlabs, USA). For detection a pair of fiber-coupled avalanche photodiodes is used (APD, SPCM-AQRH-13/14-FC, Perkin-Elmer, USA).

The sample was scanned with a fast piezo scanning stage (Stage 733.2DD; Controller E-712 with dynamic digital linearization feature for better tracking accuracy, Physik Instrumente). Coarse positioning of the sample is performed by a piezo-based coarse positioning stage (Stage M-686.D64; Controller C-867.260, Physik Instrumente). This stage is optimized for low drift due to a lead screw-free design. Detector events were counted with a National Instruments computer card (PCIe-6259, National Instruments). Instrument control and image acquisition was performed by custom-written software (LabView, National Instruments, Appendix C.5).

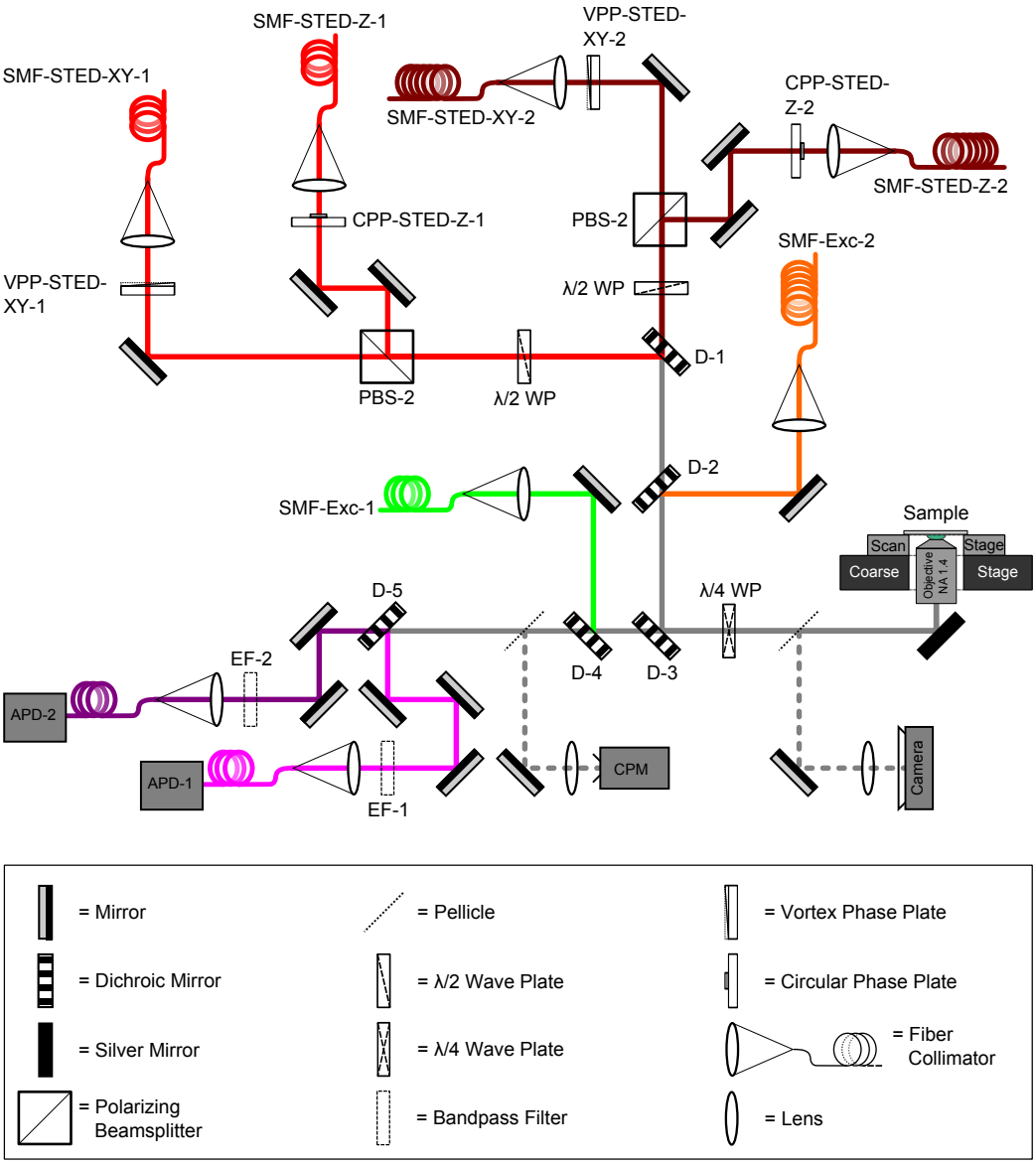

Figure 4.4: Detailed schematic depicting the co-alignment of the various beams into the objective and detection path. Naming scheme of the labeled components follows the description in the main text. Pellicle beamsplitters can be inserted into beam path for special purposes such as PSF alignment and bright field imaging (dotted gray paths). Gray: multiple wavelengths present; green: excitation path channel 1; red: depletion beams for channel 1; orange: excitation path channel 2; dark red: depletion paths for channel 2; light magenta: detection channel 1; dark magenta: detection channel 2.

Table 4.3: Key components used for the custom-built 3D STED microscope

Component in Fig. 4.3 and 4.4	Article and Company
PBS-1	PTW 1.2, B. Halle, Germany
BP-1	z 568/10, Semrock, USA
BP-2	FBH650-40, Thorlabs, USA
BP-3	LL01-647, Semrock, USA
VPP-STED-XY-1	VPP-1B, RPC Photonics, USA; 708 nm pattern
VPP-STED-XY-2	VPP-1A, RPC Photonics, USA; 735.8 nm pattern
CPP-STED-Z-1	Custom made by Lars Kastrup; "1020 3.8"
CPP-STED-Z-2	Custom made by Lars Kastrup; "1070 3.7"
$\lambda/2$-WP	RAC 4.2.15, B. Halle, Germany
$\lambda/4$-WP	custom-selected, B. Halle, Germany
PBS-2	PTW 1.20, custom-selected, B. Halle, Germany
D-1	Z 730 DCXR, Chroma, USA
D-2	Z 660 DCXR, Chroma, USA
D-3	Q 690 SPXR, AHF, Germany
D-4	585 DCXR, Chroma, USA
D-5	Z 645 DCXR, AHF, Germany
EF-1	HC 629/56, Chroma, USA
EF-2	HC 676/37, Chroma, USA

4.2.3 Reducing crosstalk through synchronized detection

A careful choice of dichroic mirrors and filters is necessary to suppress spectral crosstalk as the emission spectra of the dye pair overlap considerably (Fig. 4.1 and 4.6). Trying to keep the detection windows as wide as possible but at the same time reducing emission crosstalk demands for high quality dichroic mirrors and filters. The use of a super-continuum laser source helps in such a complex spectral setting. It allows to precisely tune excitation and depletion wavelengths by the use of filters/monochromators which would hardly be possible using fixed-wavelength laser sources. The calculated transmission through the setup of the excitation and emission beam paths based on the spectral characteristics of the dichroics and filters provided by the respective manufacturers (excluding further components) for the two different channels is shown in Fig. 4.6. Due to multiple requirements to be met by the dichroic mirror D-3 in front of the objective, the residual reflectance in the transmission band ($\sim$ 3 %) inherent to the dichroic mirror is used to reflect the Exc-2 beam into the objective (Fig. 4.5). This is

very inefficient but does not pose a problem since the loss of intensity due to the poor reflectance ($\sim$ 97 % loss at 647 nm) can be easily compensated by the ample laser power at hand. This trick relaxes the high demands on the dichroic mirror D-3.

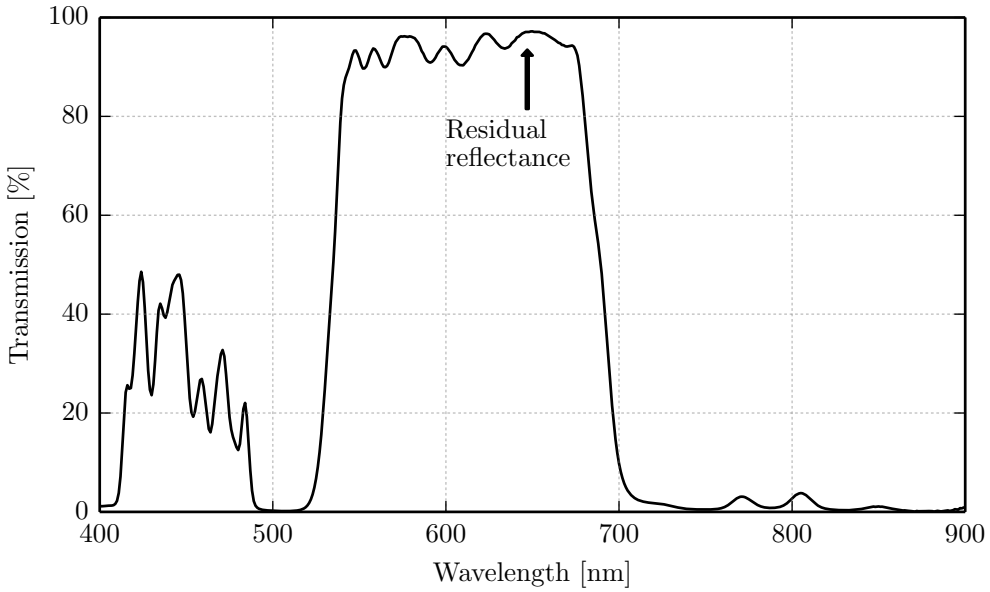

Figure 4.5: Transmission plot of the dichroic D-3 showing the residual reflectance which is exploited to reflect the excitation beam of channel two onto the sample (Exc-2 center wavelength at 647 nm indicated by arrow).

While a careful choice of emission filters and dichroic mirrors allows minimizing spectral crosstalk, it is still not negligible. Moreover, excitation of the fluorophores in detection channel 2 by the STED beams of channel 1 is an even more severe problem. Therefore, it is necessary to introduce a time-delay between the two channels to minimize these effects, thus effectively discarding counts from the inactive channel. To achieve this, the length difference ($\sim$ 20 m) between the fibers of channel 1 and channel 2 introduces a temporal delay of the pulses between the two channels of $\sim$ 90 ns used for time-gating in a synchronized detection scheme. To this end, an electronic gating device was designed and implemented (Appendix C.4). It uses the trigger output of the laser source together with adjustable electronic delays

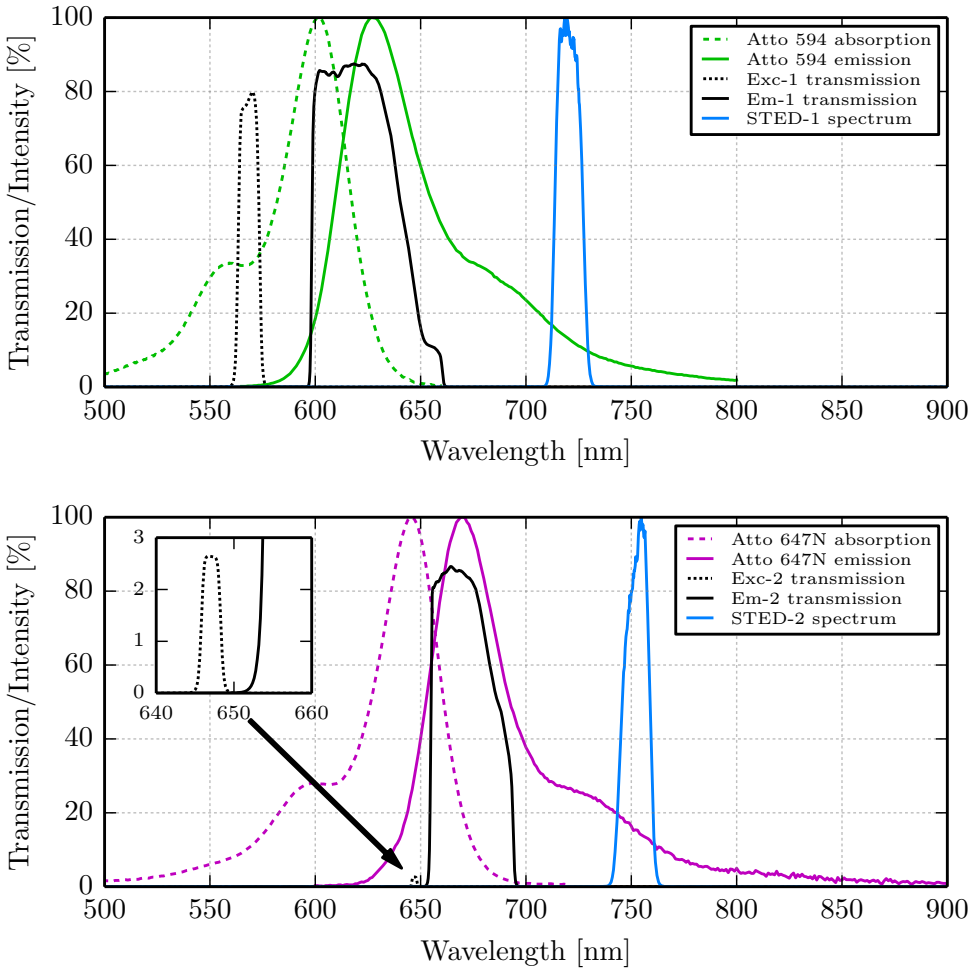

Figure 4.6: Transmission set by dichroic mirrors and excitation/emission filters in each channel's excitation beam path (dotted black) and emission beam path (solid black). Upper panel shows data for channel 1 while lower panel shows channel 2. Inset shows zoomed in part to better visualize the excitation transmission of channel 2. Spectral crosstalk of the fluorescence emission can be successfully reduced by introducing a temporal delay between the pulses of the two channels together with a synchronized detection.

to synchronize a user-defined detection time-gate with the arrival time of the photons of the respective channel by a logical AND operation (Fig. 4.7 and 4.8). By keeping the time-gate short ($\sim$ 10's of ns) dark counts as well as after pulses from both detectors are efficiently ignored resulting in low

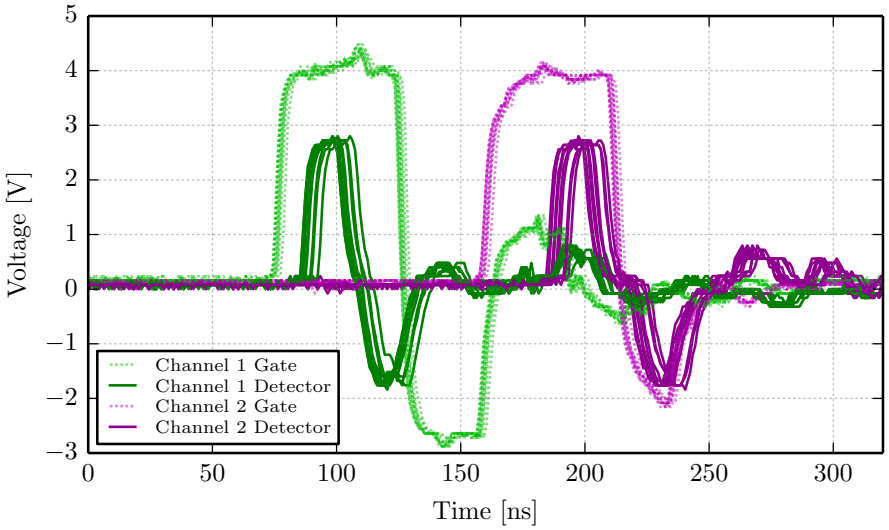

Figure 4.7: Synchronized detection using time gates. Ten individual traces recorded with a four-channel oscilloscope are plotted as an overlay. Dotted lines show the user programmable time gate during which pulses from the corresponding detector (solid lines) are registered as valid counts. Detector pulses arriving outside these time gates are discarded efficiently reducing dark counts from the avalanche photodiodes. Time = 0 is located at the rising edge of the laser source trigger. Timing differences observable between the individual detector pulses are related to the fluorescence lifetime. Damped oscillations visible are due to the electronics used without adverse effects on the time gate functionality.

background images.

To check the residual crosstalk a simple experiment was performed. A sample of single molecules of Atto 590 (Fig. 4.9 A/B) or Atto 647N (Fig. 4.9 C/D) dispersed on a cover slip is imaged using the corresponding excitation while the detectors of both channels are active. As an estimate the crosstalk is now given by the mean of all pixels of the image-wise division of the inactive channels image by the active channels image (the corresponding pixel values of the two images are divided). In the case of the first channel the bleed through to the second detector is about 0.4 % of the intensity recorded by channel 1. In the case of channel 2 the detector 1 counts only 0.1 % of the active channels counts. This discrepancy is best explained by the spectral characteristics of the dyes used; Atto 590's emission spectrum

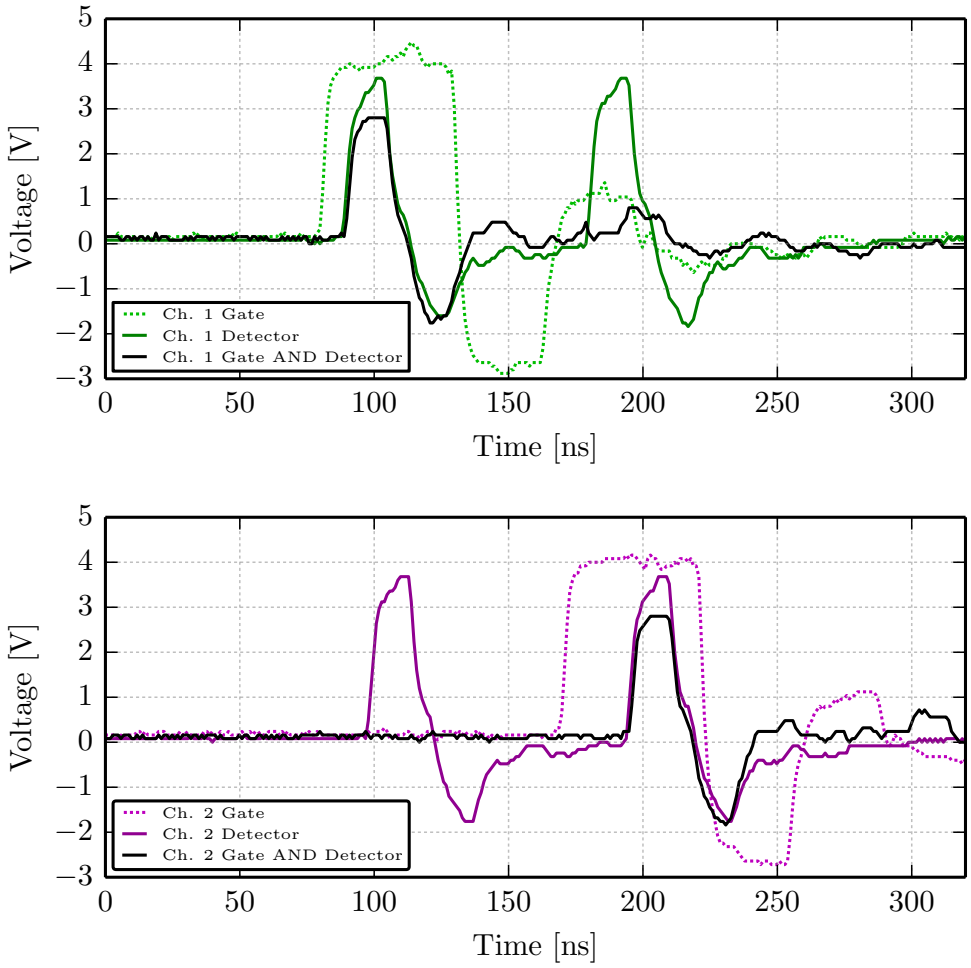

Figure 4.8: Rejection of detector pulses outside the corresponding time gate recorded as in Fig. 4.7. When set up correctly detector pulses are passed to the counters only when the arrival time corresponds to that channels time gate. Each trace shows one valid and one invalid pulse. Upper panel = channel 1; lower panel = channel 2. Time = 0 is located at the rising edge of the laser source trigger. Damped oscillations visible are due to the electronics used without adverse effects on the time gate functionality.

reaches far into the emission spectrum of Atto 647N while the opposite is not the case (Fig. 4.1). Due to this excellent crosstalk rejection by the use of a synchronized detection scheme no image post-processing to reduce crosstalk such as linear unmixing had to be employed after imaging for any of the

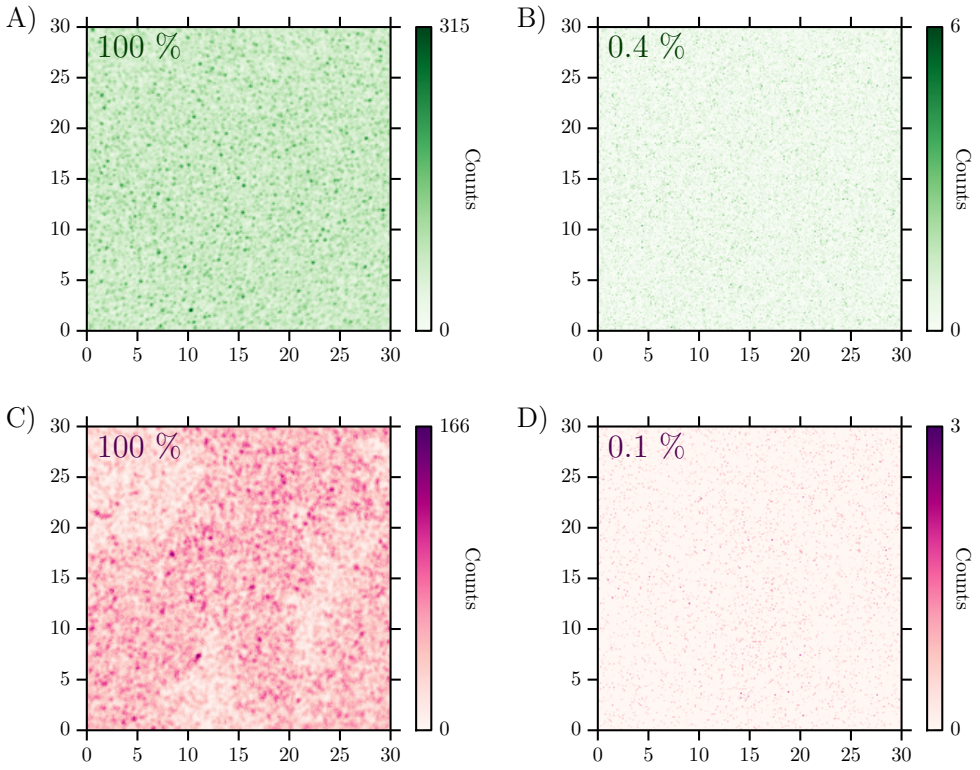

Figure 4.9: Residual crosstalk between channels. A) Atto 590 molecules imaged by irradiation with Exc-1. Recorded image set as reference for panel B. B) Atto 590 fluorescence crosstalk recorded by detector 2 amounts to 0.4 % relative to reference image (panel A). C) Atto 647N molecules imaged by irradiation with Exc-2. Recorded image set as reference for panel D. D) Atto 647N fluorescence crosstalk recorded by detector 1 amounts to 0.1 % relative to reference image (panel C). All data shown is raw data. Color mapping refers to full intensity range per image (note counts on intensity scales). Image scales in μm.

experiments conducted.

As a side note it is important to understand that this crosstalk reduction is working fine when the labeling worked out similarly well in both channels. However, in the occasion that one channel's labeling efficiency is very low while the other's is very high, the user is likely to tune the excitation intensities accordingly disproportionate. If this is the case crosstalk can be worse than measured above. This is due to the fact that the wrong dye species is excited by the overly strong excitation intensity of the weakly labeled channel provided the user tries to compensate weak labeling with high excitation

intensities. The wrongly excited dye molecules will now emit during the wrong time-gate and - with a probability proportional to the considerable emission spectrum overlap as indicated before - will emit into the wrong detection. It is thus important to keep the excitation intensities used in a particular experiment in mind. To conclude, the problem of wrong excitation and subsequent wrong emission due to extreme excitation intensity settings is relatively straightforward to spot - perfect co-localisation between the two channels will appear.

4.2.4 Achieving maximal depletion efficiency

In order to achieve maximal depletion efficiency the relative timing of the excitation and depletion pulse is critical. The excitation pulse has to arrive first in order to allow the delayed STED pulse to efficiently induce stimulated emission (Section 2.4, [Hell and Wichmann, 1994]). To ensure correct relative timing of excitation and depletion pulses for each channel, the excitation and STED-Z fiber couplers are mounted on manual linear stages and adjusted relative to the respective timing of the STED-XY beam. Correct synchronization is based solely on beam path length thus not requiring any drift-sensitive electronic timing device. Once set-up the timing generally does not have to be realigned unless relevant parts of the microscope are altered. To optimize the timing a simple experiment is performed. A μM-solution of dye serves as the sample. The phase plate of the depletion beam to be aligned is removed. The depletion efficiency is measured for a fixed depletion intensity for a set of increasing path lengths. For each position, first the fluorescence signal in the presence of the excitation beam is measured yielding $S_{Exc.}$ (mean counts of 2 $\times$ 2 μm image; pixel size 20 nm; pixel dwell time 1 ms). Consecutively, fluorescence is measured with both excitation and depletion beam active yielding $S_{Exc.+STED}$. Care has to be taken to keep excitation and depletion intensities constant during the course of the experiment. The depletion efficiency η_{STED} is then given by

$$\eta_{STED} = \frac{S_{Exc.} - S_{Exc.+STED}}{S_{Exc.}}. \tag{4.1}$$

After the measurements the respective couplers are fixed at the position which corresponds to the the highest depletion efficiency (at 0 cm/ns in Fig. 4.10). This will ensure the best possible resolution with the system at hand.

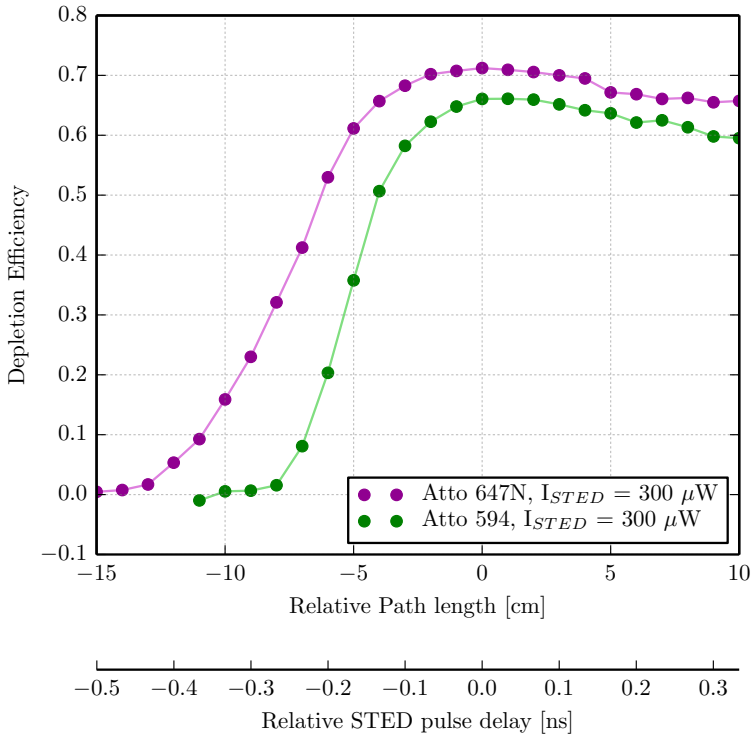

Figure 4.10: Depletion efficiency is dependent on relative timing of excitation and depletion pulse. If the depletion pulse reaches the sample before the excitation pulse, depletion efficiency quickly diminishes to zero (relative STED pulse delay < 0 ns). For STED pulse delays greater than 0 ns the depletion efficiency drops slowly as a function of the fluorophore lifetime which typically is on the order of nanoseconds. The correct timing is positioned at 0 cm/ns.

4.2.5 Depletion patterns for 3D STED microscopy

With the microscope correctly set up the last and crucial step for a working super-resolution STED microscope is the quality of the depletion patterns. Attaining patterns with a true minimum in the center is of utmost importance

since residual intensity will cause a reduction in fluorescence at the location of detection. As a rule of thumb, the intensity at the minimum should be around 1 % of the maximum of the depletion pattern. The PSFs of the depletion beams were experimentally measured by scanning across immobilized individual 80 nm gold colloids dispersed on a cover slip at a dilution of 1:1000 (British Biocell, Appendix A.3) and recording the scattering using a channel photomultiplier module (CPM, MD-963, Perkin-Elmer). The recorded intensity patterns show deep minima with little residual intensity (Fig. 4.11). The quality of the depletion beam pattern is crucial for STED microscopy in order to produce high-contrast images. More so, for dim objects such as single molecules a true central zero is essential to detect any signal above background at all.

The effect of the two individual depletion beam types and their summed intensity profile on the effective PSF were measured by imaging 100 nm fluorescent beads dispersed on a coverslip at a dilution of 1:1000 (Fig. 4.11, for details on the preparation see Appendix A.4). By selectively activating the depletion beams by means of mechanical shutters the setup can be operated as a standard diffraction limited confocal microscope (all depletion beams deactivated, Fig. 4.11 A/B), a 2D STED microscope (only STED-XY depletion beams active, Fig. 4.11 C/D), a Z-STED microscope with only the z depletion beam active (Fig. 4.11 E/F) or a 3D STED microscope (all depletion beams activated, Fig. 4.11 G/H). It is important to note that this 3D mode works with a single objective lens simply by non-coherent co-alignment of the two fundamental depletion patterns. This greatly simplifies the operation and stability of the setup compared to other techniques such as 4π-microscopy [Nagorni and Hell, 1998]. Furthermore, lateral and axial resolution can be tuned by adjusting the intensity in the respective depletion beam allowing the user to dial in optimal parameters for a particular experimental task.

Great care during alignment of the depletion intensity patterns has to be taken. The minima of the STED-XY and STED-Z beams add up when imaging in 3D mode. It is thus mandatory to obtain very low intensity values in the center of the PSFs by tuning the state of polarization in the case of the STED-XY beams. In the case of the STED-Z beam the user

has less degrees of freedom to improve the quality of the depletion pattern. The most important parameters are to use the correct wavelength for which the circular phase plate actually provides a phase shift of π in the center relative to the annular ring. Additionally, the correct lateral alignment of the phase plate relative to the incoming Gaussian beam is crucial to obtain a symmetric, non-skewed axial depletion pattern. Furthermore, the angle of the PSF with respect to the optical axis of the STED-XY and excitation beam as well as the axial position needs to be well aligned. If there is a relative angle/offset between the two depletion patterns axial depletion will suffer causing buildup of confocal signal deteriorating the resolution of the microscope. This also proves to be very important for the relative alignment of the other beams such as excitation and detection. Please see Appendix B for more detailed information on how to attain correct alignment.

In the case of the STED-XY beams, an intensity minimum amounting to $\sim$ 1% relative to the maximum (background corrected) was routinely achieved. For depletion beam powers of $\sim$ 1.5 mW, the peak brightness in STED 2D mode in comparison to the confocal non-STED mode was reduced to roughly 60 - 70%. This is in line with previous publications focusing on the effect of the polarization state on the peak brightness (for a detailed study see [Galiani et al., 2012]). The residual intensity in the central minimum causing the reduced recorded fluorescence signal in STED microscopes is mostly caused by non-perfect circular polarization of the STED-XY beams [Galiani et al., 2012]. In the case of the STED-Z beams providing axial confinement the minimum intensity routinely amounted to $<$ 1%. Signal was reduced in this case to approximately 70 - 80 % compared to non-STED recordings. In 3D STED mode, the reduced peak brightness was $\sim$ 50% of the signal recorded in diffraction-limited confocal mode. Since the residual depletion beam intensity in the central minimum accounts for the lower signal in STED images, reducing the depletion beam intensity will restore the signal originating from the central minimum ($I_{Central\ minimum} \ll I_{Sat}$) at the cost of lower resolution.

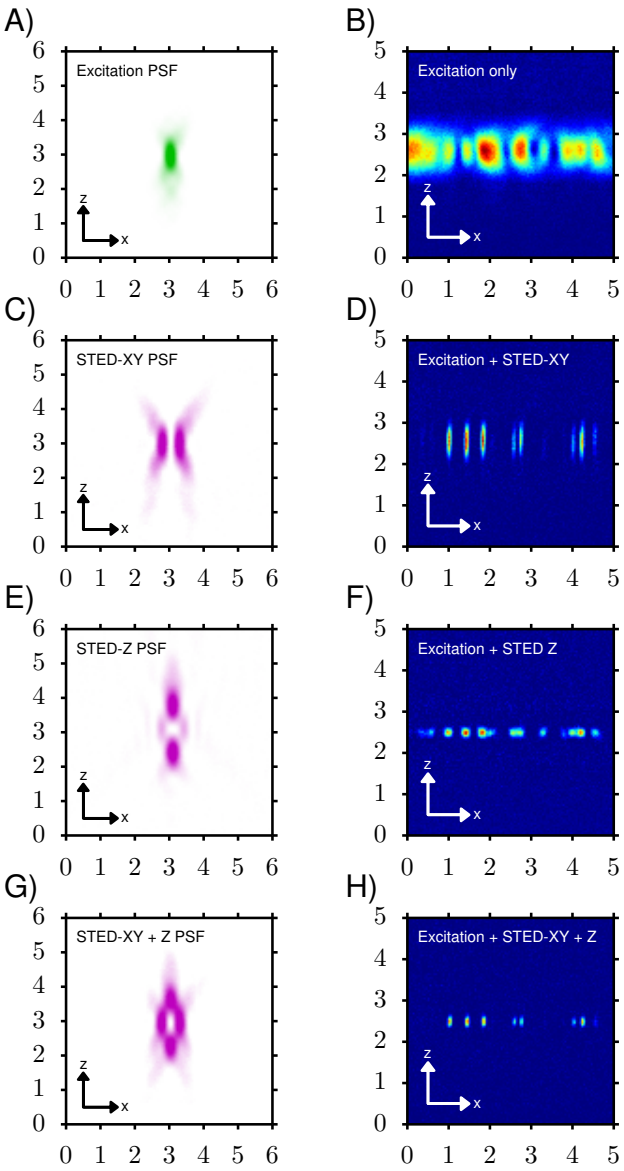

Figure 4.11: Experimentally measured point-spread functions (leftmost panels; green for excitation and magenta for depletion patterns) and corresponding fluorescence images (rightmost panels). Point-spread functions were measured by recording the scattering from an immobilized 80 nm gold bead scanned through the focus. Data from x-z scans are presented showing both the lateral and axial extent of the focal intensity distribution due to symmetry reasons. The fluorescence images were recorded using 100 nm fluorescent beads dispersed on a cover slip (Red Fluospheres 100 nm, Invitrogen; fluorescence images are shown representatively for channel 1). A) and B) Confocal mode using only the excitation beam results in a diffraction limited PSF and fluorescence image which is considerably spread along the z-axis. C) and D) The XY-STED beam improves only lateral resolution; axial resolution is not changed. E) and F) The Z-STED beam acts mainly in the axial dimension. Additionally, resolution is also slightly improved along the lateral dimension. G) and H) By spatially co-aligning the XY and Z STED beams resolution is dramatically enhanced in all three dimensions. Note that the disappearing of beads in image D) and H) is not due to excessive bleaching but due to the fact that not all beads lie directly on the scan plane. Depending on the distance from the scan plane in y and the lateral resolution objects will disappear in the image when switching from confocal to super-resolution mode. In the fluorescence images the pixel dwell time was 300 μs at a pixel size of 12.5 nm. All numbers are in μm.

4.2.6 Resolution measurements using single dye molecules

Single dye molecules attached to short pieces of DNA were imaged to test both resolution and sensitivity of our instrument in a single experiment (Fig. 4.12). To this end, a 1 nM 1:1 mixture of 60 bp long DNA molecules labeled with either Atto 590 or Atto 647N and biotin were immobilized to cover slips using NeutrAvidin and imaged in a dual-color experiment in 2D mode (for experimental details see Appendix A.5). Excitation average power per beam of < 1 μW and depletion average power per beam of > 1.5 mW were used (measured before the objective). Most of the fluorescence spots observed exhibited rather round fluorescence patterns (Fig. 4.12 A), indicating that photobleaching was not limiting in these experiments. In order to determine the resolution of the microscope the recorded 2D intensity profiles from several molecules were fitted using rotation-symmetric 2D Gaussian functions. The calculated average lateral FWHM (mean $\pm$ standard deviation) for channel 1 was 40.2 nm $\pm$ 2.6 nm (n = 32) and for channel 2 we found 34.2 nm $\pm$ 2.5 nm (n = 51).

Extracting intensity values along a line across a representative single molecule yielded slightly better results, namely $\sim$ 35 nm for Atto 590 and $\sim$ 31 nm for Atto 647N (Fig. 4.12 B and C). One possible reason for the observed improved resolution when only single line scans are analyzed could be the fact that blinking of the molecules adds to the noise of the system and thus reduces the quality of the 2D Gaussian fits. Independent of the analysis procedure it is clear that the microscope has single molecule sensitivity and that a lateral resolution of $\sim$ 35 nm can be obtained.

Axial resolution was measured using the same labeled DNA molecules as described above but with only either Atto 590 or Atto 647N present in the sample. Fitting a Gaussian function to axial cross-sections of single Atto 590 and Atto 647N molecules imaged with the STED-Z beam active shows an axial FWHM of 89.4 nm $\pm$ 14.5 nm and 88.4 nm $\pm$ 27.4 nm (mean $\pm$ standard deviation, n = 10 and n = 5, respectively, Fig. 4.12 D through F). While combining the STED-XY and STED-Z intensity profiles leads to an increased intensity in the x-y plane and should thus theoretically lead to a

slight improvement in lateral resolution ($\sim 5\,\%$), a similar lateral resolution in 3D STED mode as compared to STED-XY mode was observed due to limited experimental accuracy. It is, however, noteworthy that in Z-STED mode residual side lobes stemming from non-perfect alignment/optical aberrations of the Z-depletion pattern can be efficiently reduced in combination with the STED-XY depletion pattern.

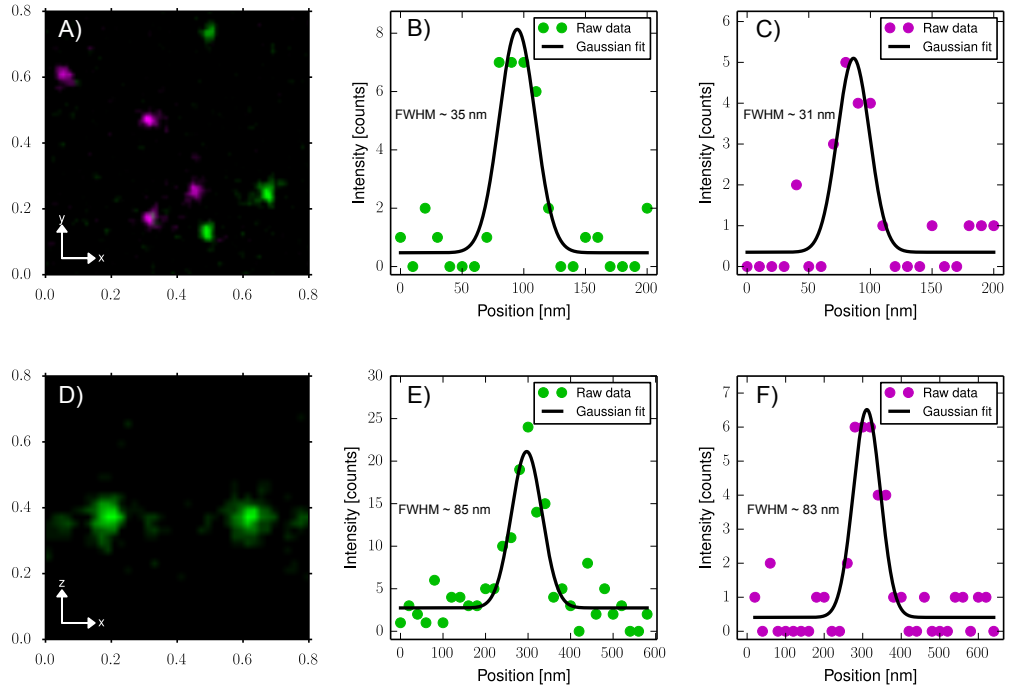

Figure 4.12: Imaging immobilized DNA molecules labeled with single Atto 590 (green) or Atto 647N (magenta) fluorophores. A) Exemplary image of single molecules imaged in STED-2D mode in the x/y plane. B) and C) Gaussian fit to cross-section of single Atto 590 or Atto 647N molecule indicating a lateral FWHM of $\sim$ 35 nm and $\sim$ 31 nm, respectively. D) Exemplary image of single Atto 590 molecules imaged using the Z-STED beams in the x/z plane. E) and F) Cross-section along the z-axis of a single Atto 590 or Atto 647N molecule shows a FWHM of $\sim$ 85 nm and $\sim$ 83 nm, respectively. Images A and D were post processed for printing purposes but not for data analysis; fits in panel B, C, E and F show raw data. Pixel size is 10 nm^2 (panels A through C) or 20 nm^2 (panel D through F) at a pixel dwell time of 400 μs. Ticks on image A and D in μm. Fitting and plotting was performed using the Python distribution *Python(x,y)* [P. Raybaut and G. Nyo, 2014].

4.2.7 Microscope stability

As we have seen above the presented STED microscope is capable of achieving diffraction-unlimited imaging down to few tens of nanometers. This feature along with the necessity to co-align multiple beams to very high precision evidently asks for high temporal stability with regards to mechanical drift. Generally, laser-scanning super-resolution microscopes are not as sensitive to long-term drift compared to localization-based wide-field setups as drift between subsequently imaged pixels becomes negligible due to the sequential construction of the image. However this only holds true for drift of the sample relative to the bundle of co-aligned beams. Any drift of beams relative to each other can quickly destroy the ability to attain super-resolved images in a STED microscope. The demand for beam stability is somewhat relaxed by the fact that the depletion intensity profile constrains fluorescence to a small spot relative to the size of the excitation pattern. Small drift between corresponding excitation and depletion beams is therefore compensated by the large excitation spot. In a dual-color instrument, however, any drift between the depletion beams of the two channels will cause a wrong alignment of the images recorded. This can be detrimental if relative distances between features of the two detection channels are to be analyzed in dual-color images.

To make sure mechanical drift is kept to a minimum only highest quality parts for the construction of the microscope were used. This comprised the use of stainless steel components if available and the construction of the microscope stage from Invar/FeNi36, an alloy with a very low coefficient of thermal expansion α of $\sim 1.2 \times 10^{-6}$ K^{-1}. To further decrease drift due to changes in temperature the whole microscope was enclosed in a box made of sheets of polyurethane foam boards (Kapa graph black, 3A Composites GmbH). This enclosure acts as a low-pass filter and thus keeps temperature fluctuations in the lab from reaching the sensitive optical parts important for the alignment of the microscope (Fig. 4.13). Furthermore, the whole back end part of the microscope was built keeping the optical path as short as possible to reduce the effect of drift on beam alignment stability (Fig. 4.4).

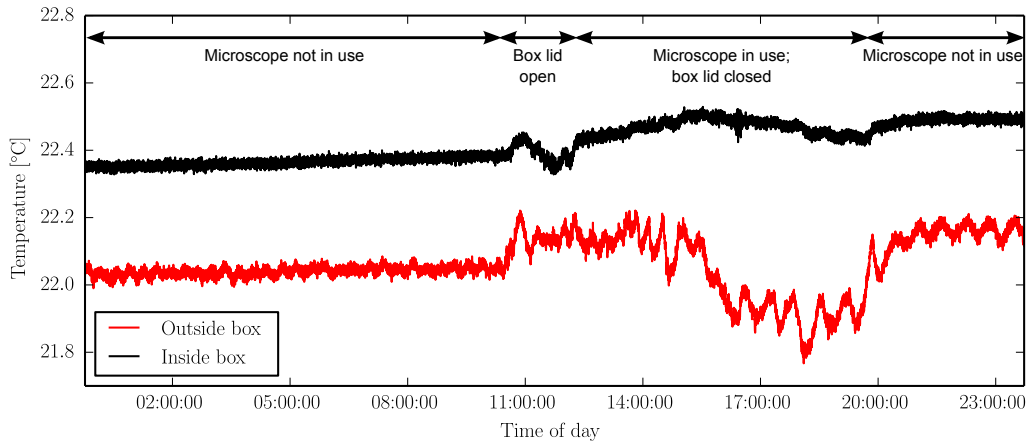

Figure 4.13: Temperature trend measured over a day inside and outside the microscope box close to the STED-Z-2 depletion beam collimator. Temperature oscillations of roughly 0.1°C and a 30 min period originate from the lab's air conditioner. These fluctuations are effectively eliminated by the enclosure. Even lower frequency temperature fluctuations are effectively decoupled from the inside of the box. The offset of both trends are partially due to an absolute offset of the temperature sensors used. Note the annotations above the temperature traces.

To check stability of the custom-built microscope a simple experiment was performed. Similar to the experiment above to record the intensity profiles of the individual beams, a single 80 nm gold bead was scanned through the focus (Appendix A.3). All phase plates were removed prior to the experiment to allow a two-dimensional Gaussian function to be fitted to the images to yield the beam position. Each beam was scanned sequentially using the function 'drift measurement' in the scan program (Appendix C.5.2). When all beams have been scanned the next cycle begins until a user-defined number of cycles has been reached. When looking at the recorded dataset it is clear that the system does drift over time (Fig. 4.14).

From the traces in Fig. 4.14 it becomes apparent that all beams seem to drift in a similar fashion. This suggests that all beams are moving relative to the sample but stay in place relative to each other. By plotting the movement of the beams relative to the reference beam STED-XY-1 over time from the same dataset it can be confirmed that most drift can be attributed to sample drift. Relative displacement between beams over time actually proves to be

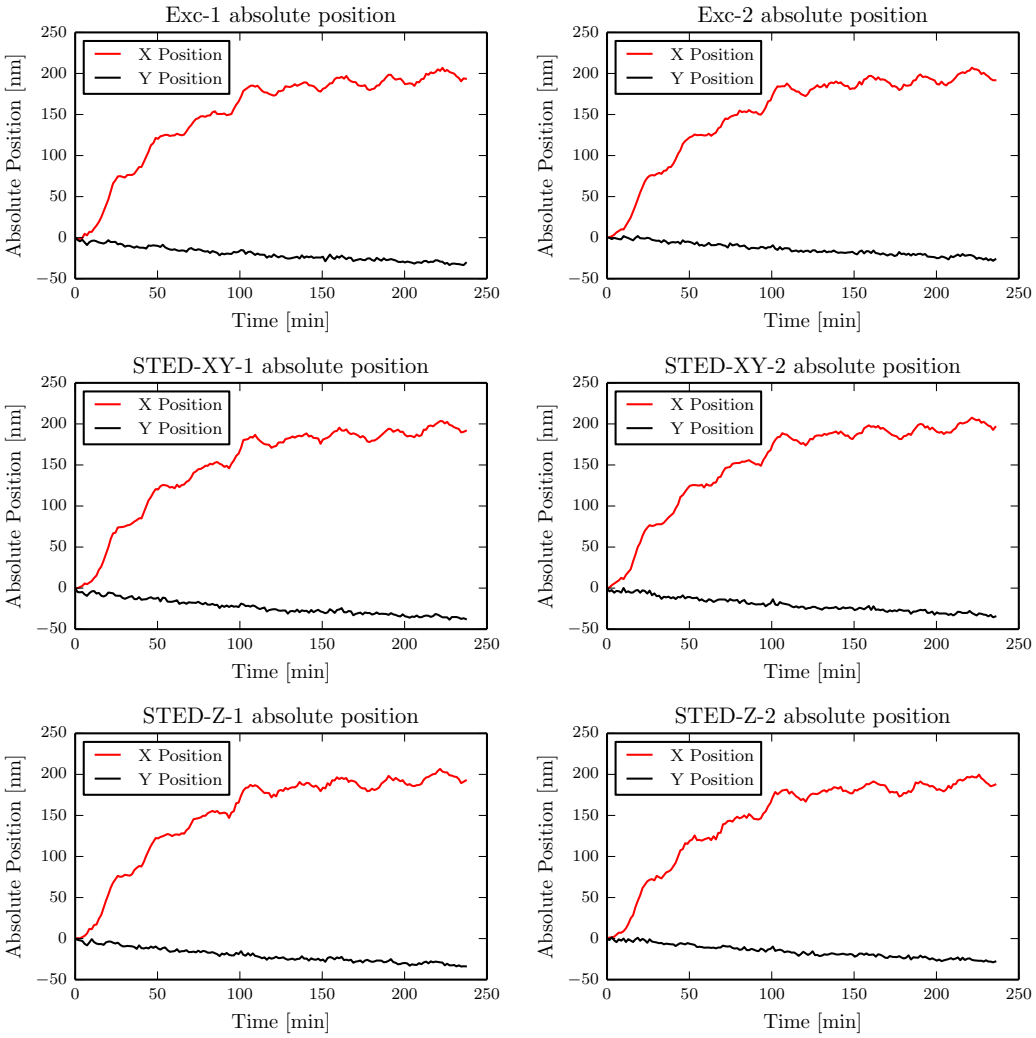

Figure 4.14: Absolute drift of the instrument measured using a single 80 nm gold bead. Note that the x-axis was the fast scanning axis. Beam position was determined by fitting a two-dimensional Gaussian function to the image. Images of each beam were continuously recorded for $\sim$ 4 hours. Traces are normalized to a start value of zero. Left and right column represents data for channel one and two, respectively.

very stable (Fig. 4.15). To check the axial movement of the beams the width of the Gaussian fit was analyzed. The data also suggests very low drift in z as changes of absolute width of the recorded PSFs are mostly below 10 nm over the full 4 hours of measurement (data not shown).

To conclude on the last experiments, the following points need to be

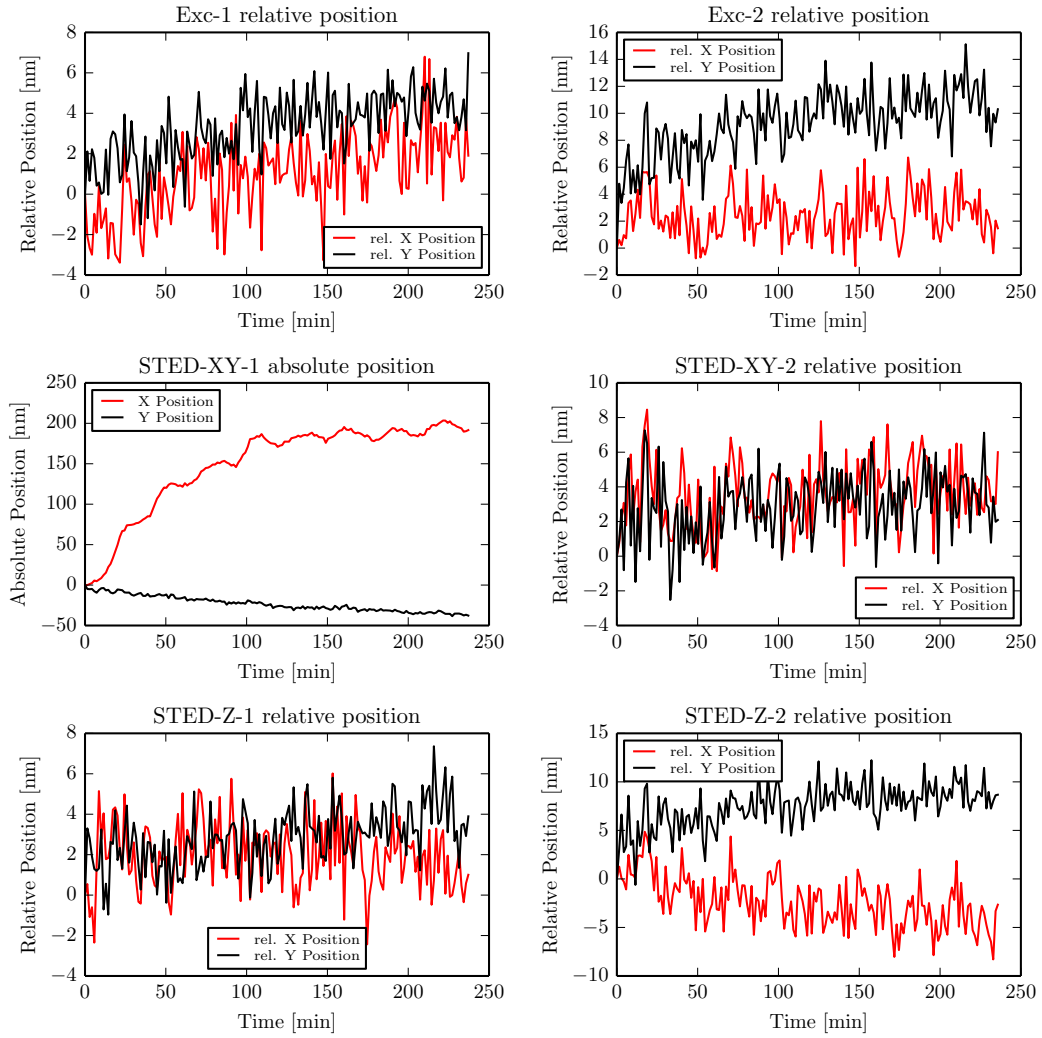

Figure 4.15: Drift between beams relative to reference beam STED-XY-1. Beam position is very stable over time, defeating the need for constant re-alignment of the excitation and depletion beams. Dataset used from Fig. 4.14. Traces are normalized to a start value of zero. Left and right column represents data for channel 1 and 2, respectively. Note that the position of beam STED-XY-1 is plotted in absolute values and serves as the reference position over time.

pointed out. First, the biggest fraction of drift observed is sample drift. Compared to sample drift in microscopes commonly used in research on the order of $\sim$ 100 nm per few minutes [Görlitz et al., 2014], the observed sample drift in the presented setup is very low. As a worst case scenario when imaging the largest field of view with the current scanning stage of

30 x 30 μm at a relatively long pixel dwell time of 400 μs and pixel size of 20 nm^2, the acquisition of one image takes 15 minutes. During this time the sample could drift up to 20 - 30 nm according to the data in Fig. 4.14, artificially elongating/shortening distances between objects. This results in a very low error of $\sim$ 0.7 ‰ over the whole range of the image diagonal of 42.4 μm. Second, the drift between beams is very low over several hours thus allowing super-resolution imaging without constant realignment. In practical terms, the setup was aligned in the morning just before imaging. Then, after lunch break, alignment was quickly checked and imaging continued till the evening. When a complete re-alignment of all beams was necessary it could be observed that beam position seemed less stable for a few days. After a couple of days, though, the stability increased until almost no drift overnight could be seen (a few tens of nm). This could be caused by the mechanical properties of the greased fine-adjustment screws present on the mirror/collimator mounts after they have been severely readjusted.

4.3 Outlook

This chapter described the performance of the microscope built during the course of this thesis. What started out as a single-channel 2D microscope is now a fully-working, high performance nanoscope. However, development rarely stops and a few things can still be improved or modified.

To bring the spectral separation of the two channels to perfection the excitation filter for channel 1 should be replaced by a bandpass filter located at around 590 nm. This is straightforward to implement and further reduces the wrong excitation of the seconds channel's fluorophores by Exc-1. Care has to be taken to still get satisfactory blocking of excitation light in the detection path. This could be enforced by changing the angle of incidence of the proposed 590 nm bandpass filter to shift the pass band to lower wavelengths.

A strength of STED imaging is its speed due to the fast underlying processes used for creation of super-resolved images [Westphal et al., 2008]. The systems design and the technique itself does not preclude the imaging of living cells. However, the current setup does not take advantage of this as

it is limited by the relatively slow repetition rate of the laser used. Currently it allows the imaging of a 1 μm x 1 μm area at a pixel size of 20 nm^2 in approximately $\sim$ 0.5 seconds. Recently, faster laser systems with a single, very powerful depletion channel have become available which operate at 20 MHz [Göttfert et al., 2013]. The use of these modern sources will allow significantly faster imaging speeds ideally suited for live-cell imaging.

A recent development is the use of the above mentioned high power laser source for depletion of two different fluorophores at a suboptimal depletion wavelength. Due to the high power the relatively low STED cross-sections at the detuned wavelength can be efficiently compensated. While this laser system was not available during this study it opens an interesting option for more simple two-color STED setups in the future and could easily be retrofitted to the herein described setup [Göttfert et al., 2013]. Additionally, the spectral width of the detection windows could be broadened thus allowing a better detection efficiency of the microscope.

A concomitant modification to make use of a faster laser system would be to settle on beam scanning. This would allow for faster image acquisition and also more complex scan paths such as averaging of scan lines which could help reduce photobleaching.

The use of polarization state converters to shape the characteristic STED-XY intensity pattern instead of using the somewhat over-sized vortex phase plates seems to be a promising approach. This could prove to be valuable when using high intensity laser sources for improved resolution as it allows to tune the phase shift to the wavelength used.

Lastly, the addition of a standard wide-field fluorescence setup to the STED microscope would allow to quickly identify regions of interest in a sample. Currently this needs to be done in confocal scanning mode which is slow compared to camera-based epifluorescence setups. Initial design considerations have been performed but the implementation has not started yet.

In summary, the instrument described provides a versatile tool for 3D two-color super-resolution microscopy and should due to its relatively simple, modular and tunable design find many applications in life science.

Chapter 5

Projects

After having characterized the technical details of the microscope the following chapter will present data recorded with the setup built as part of this thesis. It was put to use to image a variety of different biological samples ranging from nucleoporins in yeast cells and higher eukaryotic cells, C2 toxin component C2I in HeLa cells and scaffold proteins in chemical synapses in hippocampal neurons.

To begin with, an *in vitro* experiment is described which aimed at verifying a nanoparticle quantification routine for diffraction-limited microscopes. The second project provided the motivation to implement axial resolution enhancement by the use of dedicated phase mask as described in Chapter 4. Lastly, two ongoing investigations in the field of toxicology and neurology are discussed.

5.1 Particle_in_Cell-3D: An ImageJ macro

Nanoparticles with a diameter of 1 - 100 nm are controversially discussed in the light of bioactivity and human health [Lee et al., 2010, Krug and Wick, 2011]. To better assess their effect on cellular processes several methods such as mass spectrometry, flow-cytometry and light as well as electron microscopy-based techniques have been used to study nanoparticle uptake by cells [Oh et al., 2010, Suzuki et al., 2007, Andersson et al., 2011, Lu et al.,

2009, Elsaesser et al., 2010, Brandenberger et al., 2010, Mühlfeld et al., 2007]. These approaches bring along a set of disadvantages, the most prominent being elaborate sample preparation, the loss of spatial information and the restriction to ensemble measurements. To overcome these limitations we propose a nanoparticle quantification algorithm based on confocal image stacks and validate it using super-resolution STED imaging. Parts of this section have been published in the journal Nanomedicine under the title *A fast analysis method to quantify nanoparticle uptake on a single cell level* [Torrano et al., 2013]. The work was part of a collaboration with the group of Prof. Christoph Bräuchle (LMU, Munich, Germany).

The algorithm was implemented as a macro by Adriano A. Torrano for the widely-used, public domain image processing software ImageJ named Particle_in_Cell-3D to allow the user to set optimal parameters for their needs [Rasband W.S., 1997-2014, ImageJ Documentation Wiki, 2013]. It quantifies nanoparticles based on the measured fluorescence intensity of all voxels belonging to a single, discernible and diffraction limited object assuming that the total measured intensity is proportional to the amount of particles and that fluorescence self-quenching is negligible. This approach gives access to the quantification of nanoparticles in diffraction-limited images even when agglomerated. This is especially important in the context of life science as agglomerates of nanoparticles tend to form in biological medium [Stark, 2011]. By analyzing confocal image stacks of live cells typically taken with a spinning disc confocal microscope, spatial information alongside absolute quantification of particles is obtained on a single cell level which presents an advantage over the afore-mentioned techniques.

To validate the absolute quantification of optically non-resolvable agglomerates of nanoparticles, 100 nm fluorescent beads (Red FluoSpheres, Invitrogen, Appendix A.4) dispersed on a cover slip were first imaged in confocal mode and subsequently in STED 2D mode. This elegant solution allows to directly compare the output of the macro to the actual number of nanoparticles in a given region as the nanoparticles are resolved in the super-resolution image (Fig. 5.1).

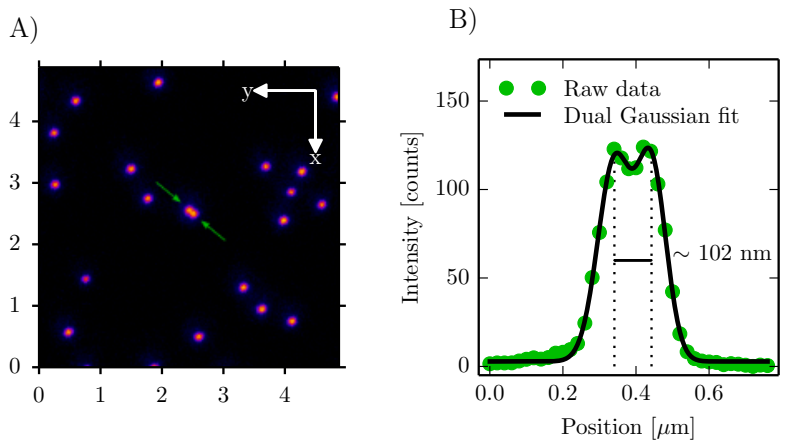

Figure 5.1: Neighboring 100 nm fluorescent polystyrene beads can be resolved using the STED setup. A) Representative STED image of 100 nm fluorescent nanoparticles dispersed on a cover slip imaged using 2D STED mode. B) Dual Gaussian function fitted to the intensity profile over two adjacent beads as indicated by green arrows in panel A. The fit yielded a separation of the two centers of highest intensity of $\sim$ 102 nm showing that even nanoparticles in direct contact with each other are resolved individually. Axes ticks in μm.

Analysis of two image stacks with 619 objects using the macro and STED microscopy revealed a good agreement of absolute quantification up to agglomerates of at least five nanoparticles (Fig. 5.2). As most particles were monodispersed in the samples too little agglomerates comprised of more than five particles were present leading to untrustworthy statistics (Fig. 5.2).

For the proposed algorithm to correctly quantify nanoparticles in absolute terms the variability in fluorescence intensity for single particles is an important parameter. For the tested nanoparticles the number of fluorophores per particle was relatively constant. This should be tested before trusting results from the macro and hence a calibration procedure is an optional routine built into the macro. The macro also allows a semi-automatic three-dimensional segmentation of cells into membrane-associated and lumen-associated regions to gain insights into the localization of particles taken up by the cell. A more thorough description of all features of the Particle_in_Cell-3D macro can be found in the original publication by the interested reader [Torrano et al., 2013].

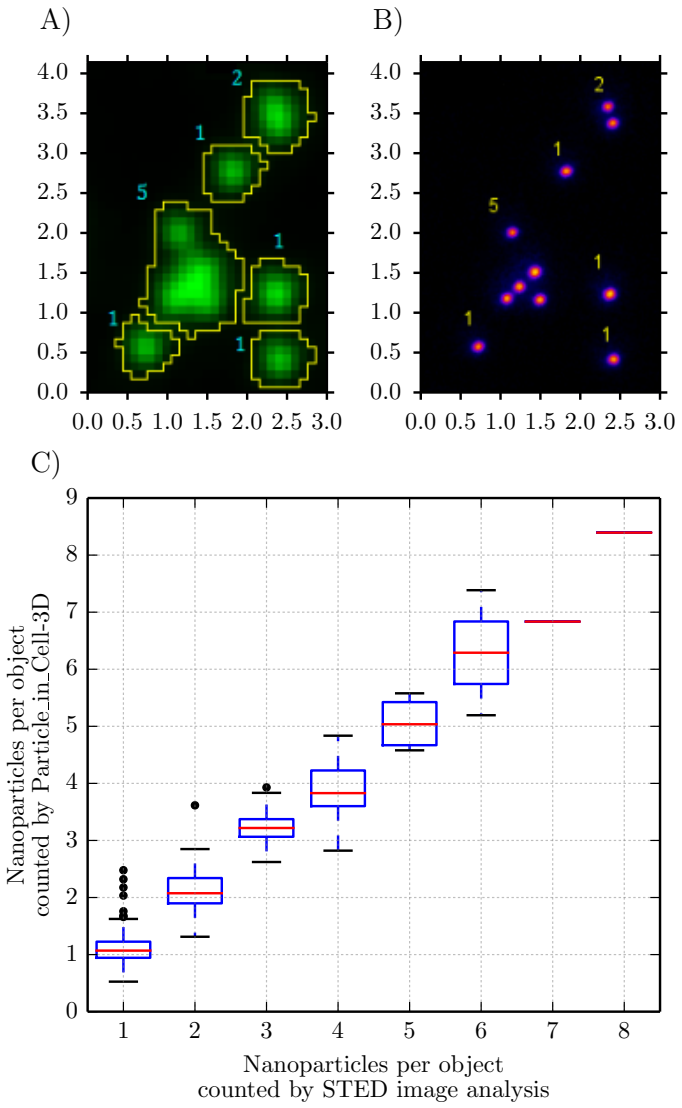

Figure 5.2: Direct comparison of Particle_in_Cell-3D macro output to actual particle counts using STED microscopy. A) Representative section of a confocal image analyzed by the macro with automatically assigned objects encircled in yellow. Computed counts are written next to the objects. B) STED image of the same region and direct counting by the observer. The counts are matching the output of the macro Particle_in_Cell-3D in panel A. C) Performance of Particle_in_Cell-3D ImageJ macro compared to STED image analysis. The calculated number of 100 nm sized NPs in an object agrees well with the actual number as determined by STED image analysis. Two 30 $\times$ 30 μm stacks were analyzed, resulting in 619 objects. A total of 443 objects were composed of one NP, 100 objects of two NPs, 43 objects of three NPs, 25 objects of four NPs, four objects of five NPs, two objects of six NPs, one object of seven NPs and one object was made up of eight NPs as determined by super-resolution imaging. Whiskers (black horizontal bars) extend up to 1.5-times the interquartile range (depicted as blue box); black dots represent outliers outside of the whisker range; median is drawn red. Axes ticks in panel A and B in μm.

5.2 2D vs. 3D STED imaging in cells

Parts of this section have been published in the journal Optics Express under the title *Simultaneous dual-color 3D STED microscopy* [Osseforth et al., 2014]. Having put the microscope to a first test we wanted to demonstrate its capabilities on biological samples in collaboration with the group of Prof. Heinrich Leonhardt (LMU, Munich, Germany). Nuclear pore complexes (NPCs) have been proven to be an excellent test system for super-resolution optical microscopy [Löschberger et al., 2012, Szymborska et al., 2013, Göttfert et al., 2013]. NPCs are complex structures made up of more than 456 individual proteins divided into $\sim$ 30 types of distinct proteins, so-called nucleoporins, and a diameter of roughly 100 nm and $\sim$ 120 MDa [Alber et al., 2007, Lim and Fahrenkrog, 2006]. NPCs are the sole site at which nucleocytoplasmic transport of cargo such as RNAs, membrane proteins and soluble proteins takes place either by diffusion or mediator-based pathways. Transport rates of up to 1000 events per second and NPC have been reported stressing the importance of this barrier between the two major cellular compartments, the cytoplasm and the nucleus [Grünwald and Singer, 2012]. In a simplistic view, it consists of cytoplasmic filaments protruding into the cytoplasm, a central core constituting the static structure of the NPC and a nuclear basket located towards the nucleoplasm (Fig. 5.3, [Sorokin et al., 2007]).

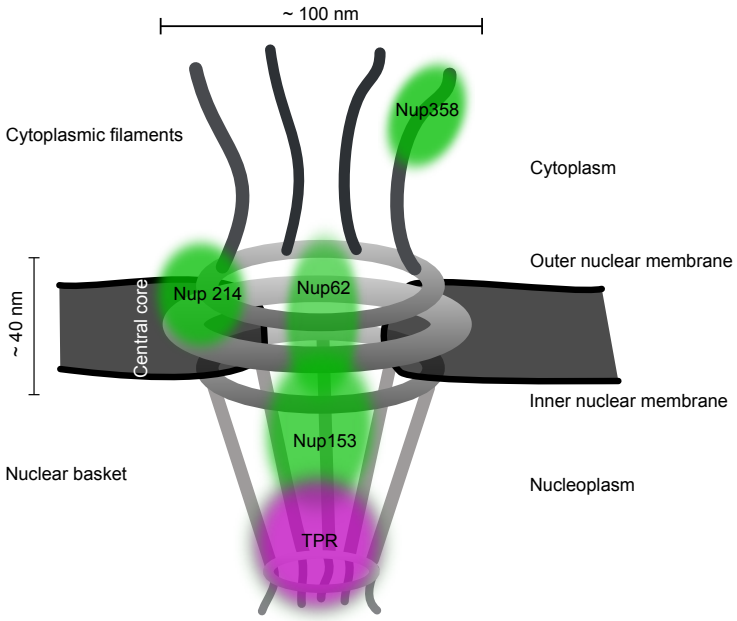

Figure 5.3: Schematic overview of the nuclear core complex and approximate sites recognized by the αFG-repeat (green) and αTPR (magenta) antibody used for imaging. Figure adapted from Schermelleh et al. [2008] and Sorokin et al. [2007].

5.2.1 Imaging nuclear pore complexes in fixed cells in 2D STED mode

We first investigated fixed human bone osteosarcoma U2OS cells with nuclear pore complexes immunostained for dual-color imaging in 2D mode (Fig. 5.4, Appendix A.6). Primary antibodies were targeted against the phenylalanine-glycine repeat (FG-repeat) region common to several nucleoporins in the central or the cytoplasmic region of the NPC (αFG-repeat, channel 1, secondary antibodies conjugated to Alexa 594). We also used primary antibodies to H3.X/Y which showed a cross-reaction with nuclear pore complexes [Wiedemann et al., 2010]. Sequence alignment indicates that it is most likely targeted to the inner basket protein Tpr (αTpr, channel 2, secondary antibodies conjugated to Atto 647N, Fig. 5.3). Cells were imaged using a voxel size of 20 x 20 x 250 nm (xyz). Average power used for each excitation and depletion beam was < 1 μW and > 1.5 mW, respectively.

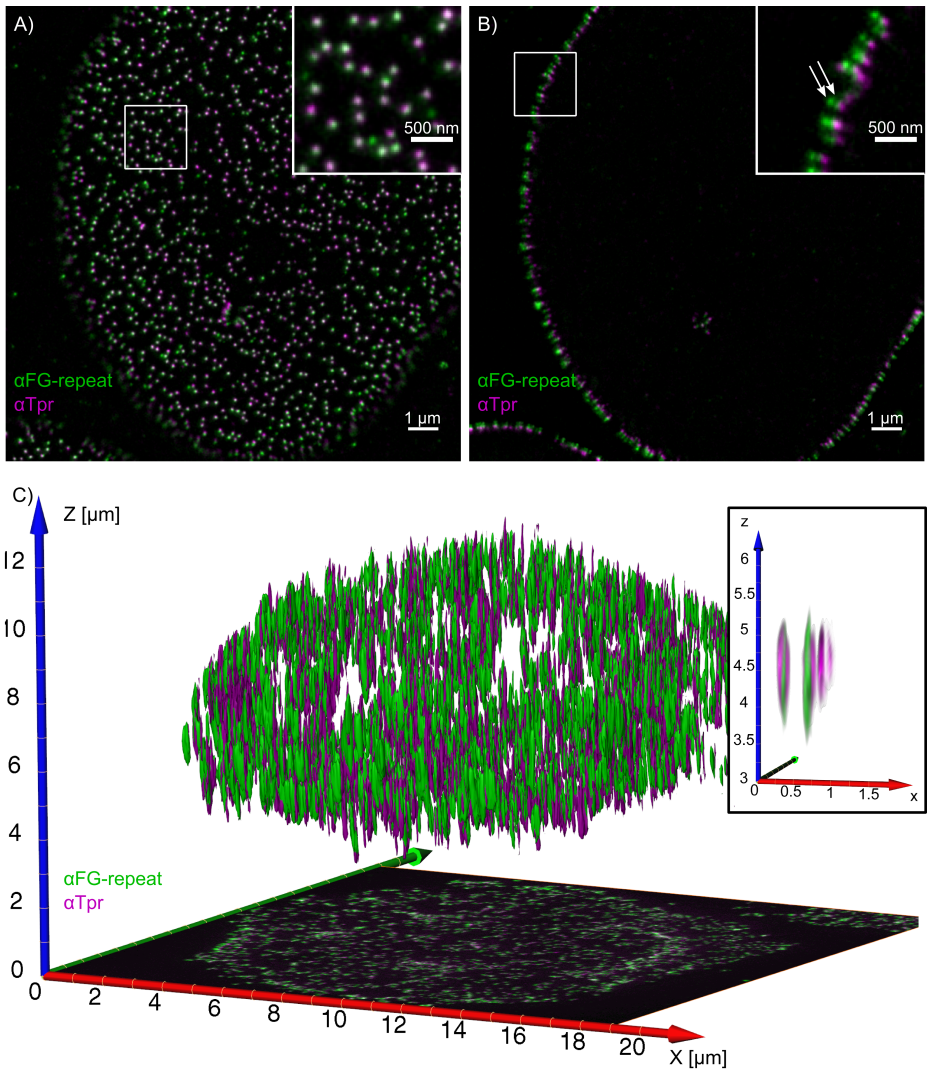

Figure 5.4: Dual-color STED microscopy in 2D mode of fixed U2OS cells using antibodies targeting different parts in the NPC. Green: Primary antibody against FG-repeat containing nucleoporins detected via secondary antibody conjugated to Alexa 594. Magenta: Primary antibody against inner nuclear pore basket protein Tpr detected via secondary antibody conjugated to Atto 647N. Images were background corrected and contrast was enhanced for printing purposes. Pixel dwell times were 180 μs. Depending on the z-height of the imaging plane different views of the cell nucleus are obtained. A) Apical slice shows co-localization of the two secondary antibodies with a FWHM of single nuclear pore complexes of $\sim$ 80 nm. B) Mid-section slice through the nucleus shows a clear separation between the two secondary antibodies. In contrast to Tpr, the FG-repeat antibody typically displays two spots, in the central part and the cytoplasmic side of NPCs (white arrows), demonstrating the ability to separate different epitopes within this large $\sim$ 120 MDa sized complex. C) 3D isosurface reconstruction of 34 slices (19 x 19 μm) of one nucleus atop a maximum intensity projection of the same data using Avizo 8.0.1 (FEI) and Fiji [Schindelin et al., 2012]. Inset shows zoomed in volume rendering of individual NPCs. Figure taken from Osseforth et al. [2014].

In an apical slice viewing top-down onto the nuclear membrane, co-localization of the two colors is observed (Fig. 5.4 A). The mean FWHM ± standard deviation of single dot-like structures is 81 nm ± 6.6 nm (n = 20) and 80 nm ± 5.9 nm (n = 20) in channel 1 and 2, respectively. In contrast, when looking at the mid-section slice of the nucleus a distinct staining pattern can be observed in which antibodies directed against FG-repeats are oriented towards the cytoplasm relative to the signal from the Tpr antibody (Fig. 5.4 B). Strikingly, two distinct regions targeted by the αFG-repeat antibody with a separation of about 92.2 nm ± 11.4 nm (n = 8) can be observed for a single nuclear pore complex. In a similar experiment using 3D structured illumination microscopy (3D SIM) different epitopes recognized by the same primary antibody could not be resolved [Schermelleh et al., 2008]. It is known that the commercially bought antibody does in fact react with Nup62, Nup214, Nup358 and Nup153 ([Schermelleh et al., 2008], Fig. 5.3). While the first three proteins are located towards the cytoplasmic side on the nuclear pore complex, Nup153 is found more centrally on the same level as the nuclear lamina [Schermelleh et al., 2008]. Since in 2D mode the lateral resolution of the herein presented setup is higher than that of 3D SIM, the observation of two distinct label positions strongly suggests that we can in fact discriminate between different epitopes on a single nuclear pore complex using the same primary antibody. The antibody directed against Tpr that constitutes the inner basket locates even further at the inner nucleoplasmic side of the NPC [Wiedemann et al., 2010]. The mid-section slice can reveal many details as the object of interest is correctly oriented in the focal plane and shows only a spot like pattern of small size. This is due to the fact that for this orientation the structure of interest, i.e. location of the respective epitopes, is oriented in the direction of optimal resolution.

This fortunate combination of circumstances is seldom found when imaging more complex structures in cells with strongly asymmetric effective PSFs. Additionally, to infer trustworthy results representative of the whole cell nucleus from only a single slice is rather difficult and oftentimes unjustified. The downside of low axial resolution becomes apparent when calculating a 3D reconstruction of 34 slices of one nucleus (Fig. 5.4 C). In all but the mid-

section slice information gained from imaging is compromised due to the poor axial resolution of the 2D STED mode. Therefore, three-dimensional super-resolution microscopy is necessary in order to quantitatively interpret microscopy data from three-dimensional biological structures that extend along the optical axis. For the given example of NPC, the correct sectioning can lead to two orthogonal 2D projections of the 3D structures which yields already a wealth of information, however, for more complex three-dimensional structures without predetermined spatial orientation, 3D super-resolution data is required.

5.2.2 Imaging replication complexes in fixed cells in 3D STED mode

To test the performance of the 3D mode in a dual-color experiment we imaged replication complexes in mouse C2C12 myoblast cells in early to late S-phase using a pulse labeling experiment (Appendix A.7). 5-ethynyl-2'-deoxyuridine (EdU) was incorporated into cells for 15 min after which cells were formaldehyde fixed. EdU labeled postreplicative DNA was detected with Alexa 594 (channel 1) via click chemistry and the replication machinery was immunostained with primary antibodies against proliferating cell nuclear antigen (αPCNA) and secondary antibodies conjugated to Atto 647N (channel 2). A series of z-slices was acquired which allowed a 3D reconstruction of the replication foci within the nuclear volume (Fig. 5.5 A).

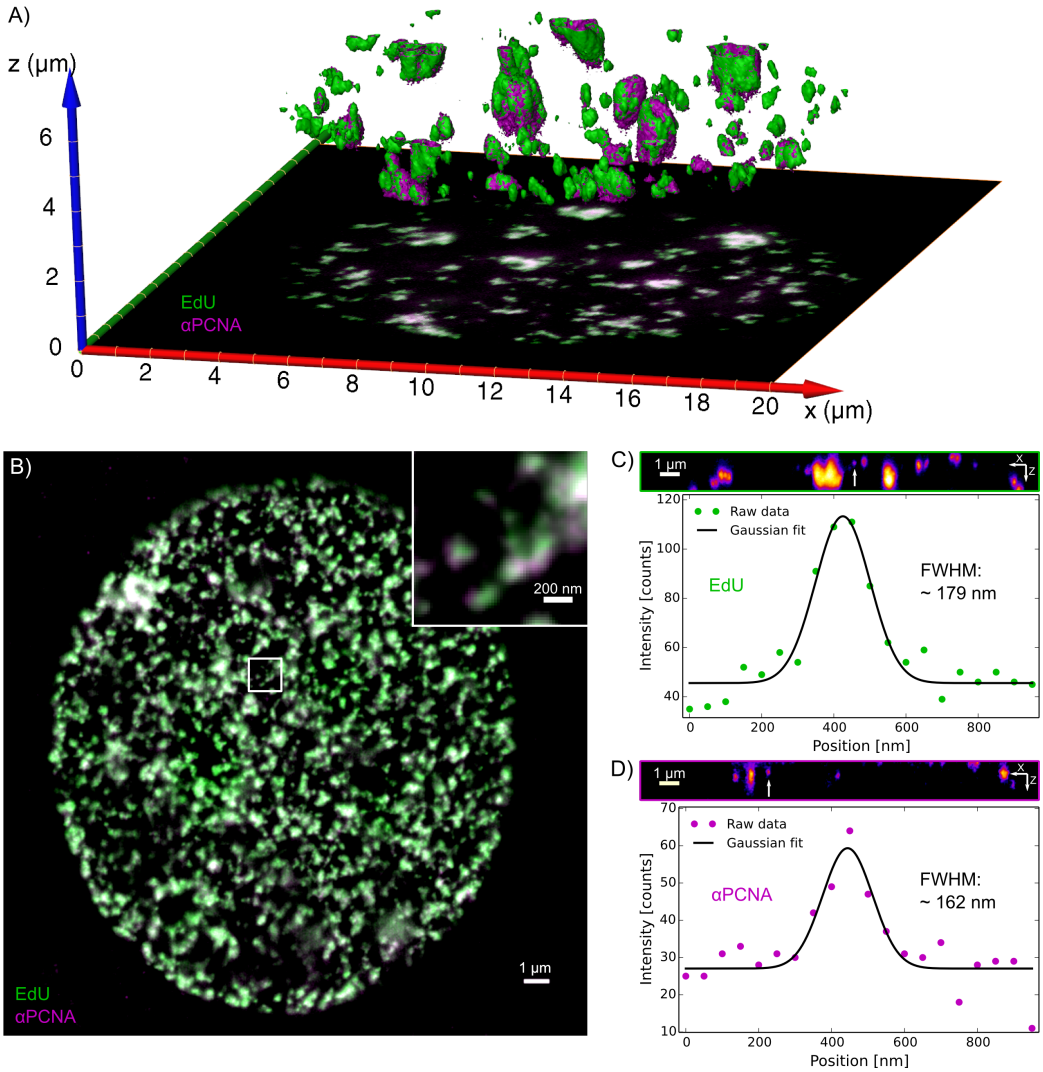

Figure 5.5: Replication foci in a C2C12 cell nucleus in late S-phase labeled during a 15 min EdU pulse imaged with the dual-color 3D STED microscope. EdU incorporation was visualized by covalent coupling of Alexa 594 dye via click chemistry (first channel; green). The second channel (magenta) shows immunostaining of PCNA using Atto 647N-conjugated secondary antibodies. A) 3D isosurface reconstruction of 38 dual-color image planes taken in 3D mode with a voxel size of 50 nm^3 at a pixel dwell time of 400 μs using Avizo 8.0.1 and Fiji [Schindelin et al., 2012]. The bottom plane (20 x 20 μm) shows the maximum intensity projection of the data set. B) x-y slice of a different nucleus in early S-phase imaged in 3D mode with a pixel size of 20 nm and pixel dwell time of 200 μs. C) Upper panel: Representative x-z-slice assembled from the first channel (EdU) of the image stack used for subfigure A. Lower panel: Gaussian function fitted to raw data of upper panel, position indicated by arrow. D) Upper panel: Representative x-z-slice constructed from the second channel (αPCNA) of the image stack used for subfigure A. Lower part: Gaussian function fitted to raw data of upper panel at position indicated by arrow. Image data was post processed to remove background and improve contrast for printing purposes. Figure C and D use a multicolor look-up table to better visualize the dynamic range of the images. Fitting and plotting was performed with raw data using the Python distribution *Python(x,y)* [P. Raybaut and G. Nyo, 2014]. Figure taken from Osseforth et al. [2014].

As expected for the 15 min pulse experiment the EdU signal partly co-localizes with PCNA in replication foci while other areas show only post-replicative DNA (Fig. 5.5 B, [Baddeley et al., 2010]). Replication foci show a heterogeneous three-dimensional shape with a significant variability in size, details which would be hidden when imaging in 2D mode. By fitting Gaussian functions to cross-sections along the axial dimension one finds narrow features with a FWHM of $\sim$ 180 nm (EdU) and $\sim$ 160 nm (PCNA) indicating the improved axial resolution of the 3D STED setup (Fig. 5.5 C/D). In an earlier study which used 2D dual-color STED microscopy to quantify replication complexes its reduced axial resolution forced the researchers to disregard objects smaller than 400 nm in z in their quantification analysis [Cseresnyes et al., 2009]. As seen here in the case of 3D STED this will result in a quantification error as replication complexes smaller than the diffraction limit in the axial dimension are present in the mammalian nucleus [Baddeley et al., 2010, Cseresnyes et al., 2009]. Thus, by using two depletion beams per channel we are able to obtain dual-color images with high resolution in all three dimensions allowing us to reveal nuclear architectures of dimensions much smaller than the diffraction limit.

5.2.3 Imaging fixed yeast cells using nanobodies

To illustrate that the setup has high sensitivity even in a cellular environment, we chose a different biological example, namely Nup82 in *Saccharomyces cerevisiae* (yeast) cells (Appendix A.8). Nup82, a nucleoporin, locates towards the cytoplasmic side of the nuclear pore complex between the outer and inner ring and acts as a linker nucleoporin [Rout, 2000, Alber et al., 2007]. It serves as an anchor point for FG-nucleoporins which are natively unfolded proteins featuring phenylalanine-glycine repeats filling the central channel and protrude towards the nucleoplasm and cytoplasm [Alber et al., 2007]. Due to the cell wall surrounding yeast cells, standard immunolabeling methods employing a primary and secondary antibody present a challenge. Thus, before labeling, the cell wall needs to be digested creating so called spheroblasts. This greatly affects cellular morphology and possibly creates

artifacts when imaging intracellular structures [Ries et al., 2012]. We therefore chose a different approach to selectively label Nup82. This comprised the genetic fusion of green fluorescent protein (GFP) to the protein of interest. Subsequently, cells were labeled with small αGFP-antibodies - so called nanobodies - carrying the inorganic dye Atto 594 which can penetrate the cell wall without its prior digestion [Ries et al., 2012]. Nanobodies are very small (13 kDa, 1.5 nm x 2.5 nm) camelid antibodies consisting of only the heavy chain variable domain [Rothbauer et al., 2006]. Fluorescently labeled nanobodies are termed chromobodies [Rothbauer et al., 2006]. As only one antibody carrying one to two fluorophores can attach to one GFP molecule, the amplification effect of standard immunolabeling techniques does not apply here [Ramos-Vara, 2005, Coons, 1955]. The signal recorded was thus lower than in common immunostaining images like e.g. Fig. 5.4 and Fig. 5.5. The same area comprising several cells immobilized on a cover slip by the use of Concanavilin A was imaged in standard confocal, 2D and 3D STED mode (Fig. 5.6, 5.7 and 5.8).

To better illustrate the effect of the three different imaging modes, the images are split along the diagonal. Diffraction-limited confocal is shown opposed to 2D STED mode (Fig. 5.6) and 2D STED mode opposed to 3D STED mode (Fig. 5.7). A zoomed in representative cell from the dataset is shown in Fig. 5.8. It becomes evident that diffraction-limited images cannot resolve the organization of nuclear pore complexes in the nucleus. At best, the distinct localization to the nuclear membrane can be observed without the ability to quantify individual nuclear pore complexes. When switching to STED 2D mode, what appears to be individual nuclear pore complexes can be seen. However, even when focusing on the axial center of the nucleus in a xy scan, signal from Nups from the apical sections above and below the imaging plane are visible (signal visible inside the nuclear membrane ring, Fig. 5.6, 5.7 and 5.8). This is due to the diffraction-limited axial resolution inherent to this imaging mode. When imaging in STED 3D mode the focal plane is constrained to a much smaller depth of view effectively discarding signal from the apical sections of the nucleus. The signal from Nup82 is thus only located in the nuclear membrane rim in the mid-section.

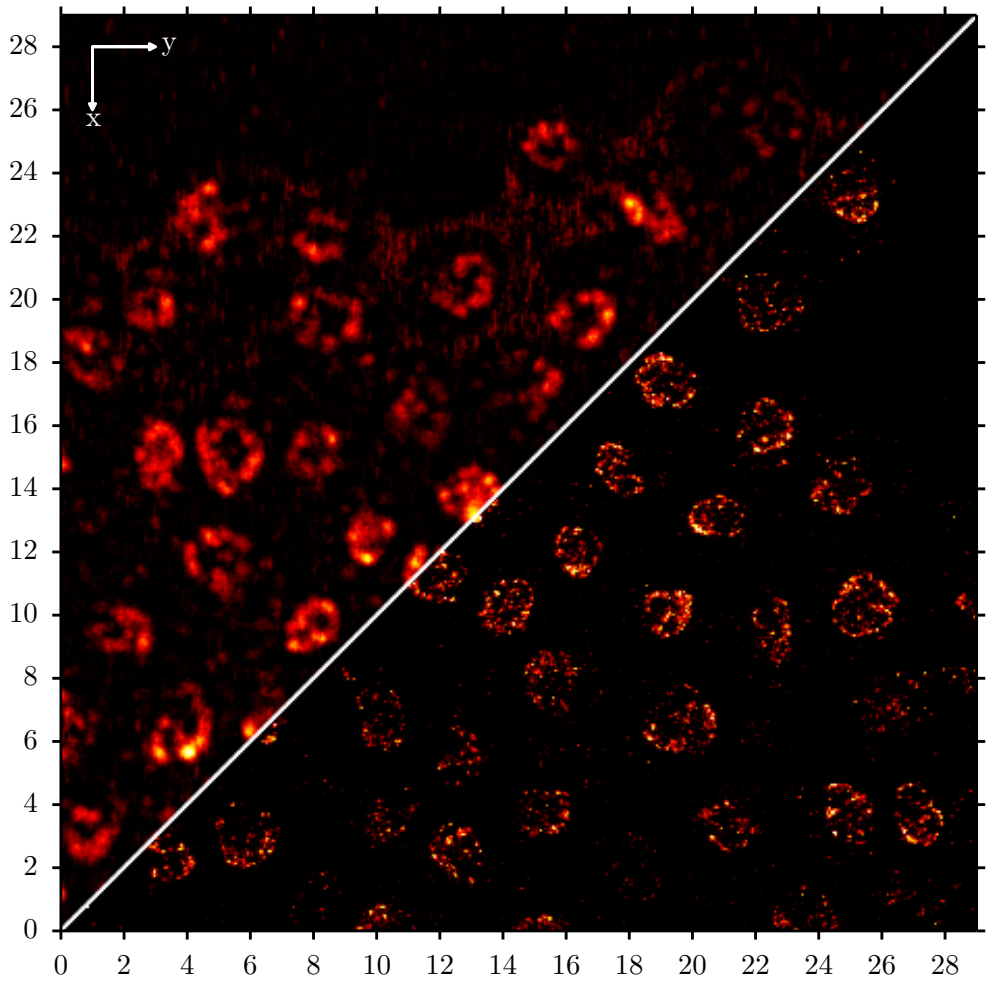

Figure 5.6: Nup82 stained using Atto 594 labeled nanobodies targeted against GFP-tagged protein. Upper left triangle shows area imaged in diffraction-limited confocal mode. Individual nuclear pore complexes cannot be resolved but a ring-like structure suggests localization to the nuclear membrane. Lower right part of the image shows the area imaged using STED 2D mode. As expected, the superior resolution allows to discern the ring-like structure into smaller dot-like individual nuclear pore complexes. Image was post-processed for visualization purposes. Pixel dwell time was 600 μs at a pixel size of 20 nm. All numbers are in μm.

While a complete three-dimensional scan in 3D STED mode similar to the data shown in Fig. 5.5 A was not successful due to excessive photobleaching and low signal, imaging a single optical slice can prove advantageous. When

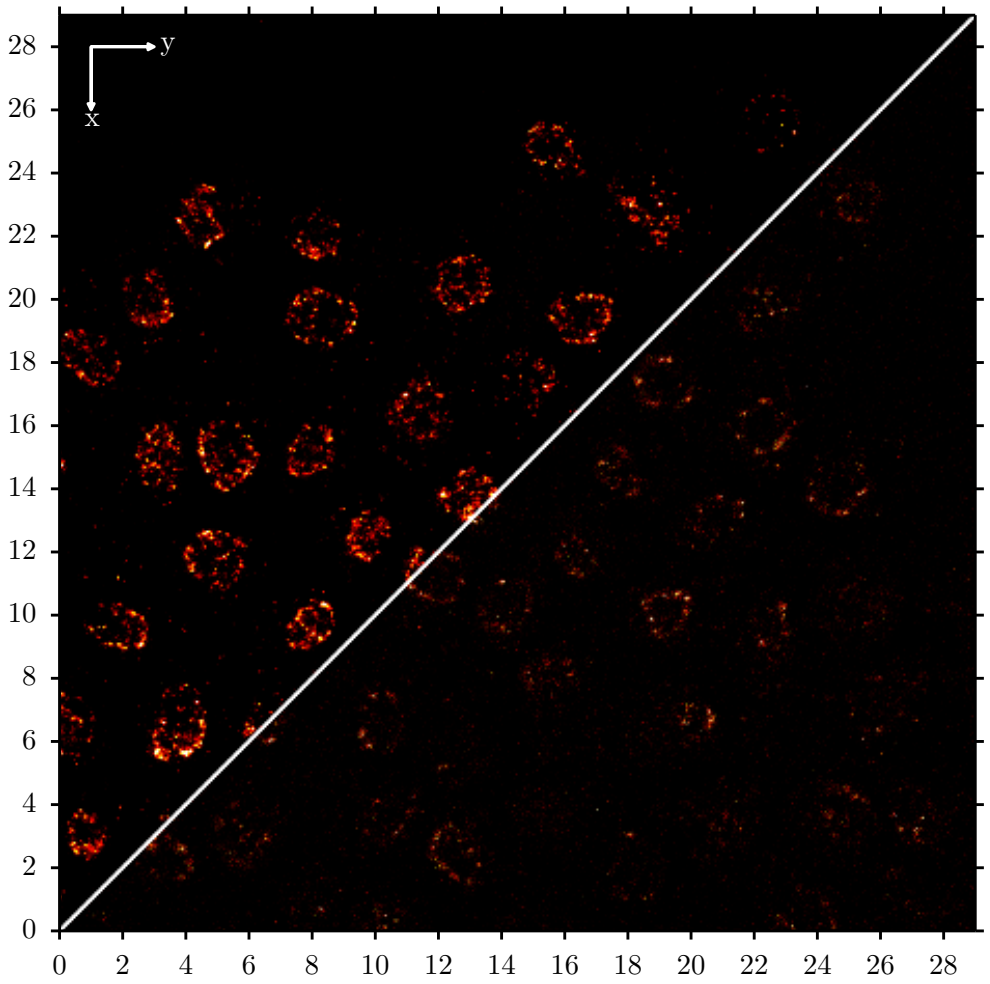

Figure 5.7: The same imaging area as in Fig. 5.6 illustrating the difference between STED 2D and STED 3D mode. While the upper left part above the white line was imaged in STED 2D mode the part below was acquired in 3D mode. While in 2D mode there is signal stemming from out-of-focus regions present seen as dots inside the nucleus this type of signal disappears when switching to 3D mode. As the imaged volume decreases along z in 3D mode, less labeled proteins lie inside the imaging plane thus reducing apparent signal. The signal from the nuclear membrane is mostly preserved while the spots inside the nucleus are discarded. Image was post-processed for visualization purposes. Pixel dwell time was 600 μs at a pixel size of 20 nm. All numbers are in μm.

imaging in cells it is often of importance to know the cellular compartment from which a recorded signal originates. Due to the low depth of view in

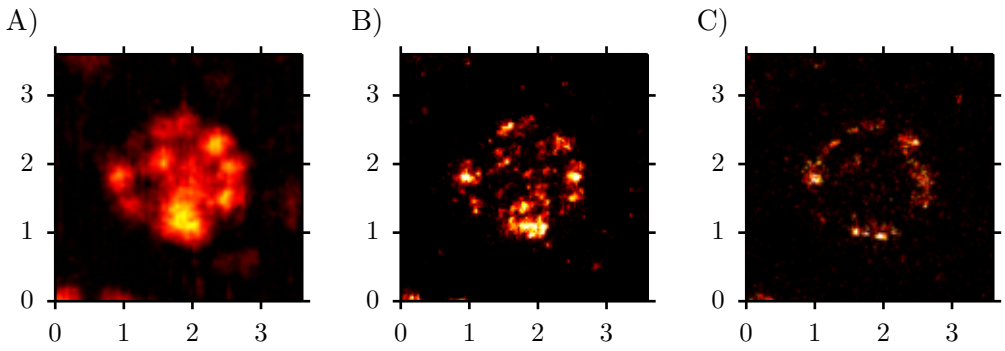

Figure 5.8: To allow a better comparison between imaging modes a representative cell from the dataset shown in Fig. 5.6 and 5.7 is plotted. A) In confocal mode the localization of Nup82 to the nucleus is observed. Details are hidden due to the diffraction limit. B) STED 2D mode allows to resolve individual substructures. Due to diffraction-limited axial resolution, signal from a considerable depth is projected onto the imaging plane (mid-section). This results in signal recorded in the center of the nucleus stemming from the apical region even though the focal plane was set to the axial center of the nucleus. C) In 3D STED mode the depth of focus is reduced to about 100 nm. Out-of-focus objects such as the aforementioned signal from the apical region are selectively discarded. As a result, only NPCs in a circle are visible indicating the optical slice through the nucleus. If objects extent further in the axial dimension than the axial resolution they will appear dimmer due to the smaller focal volume which is left to emit fluorescence. Image was post-processed for visualization purposes. Axis tick marks in μm.

the 3D STED mode the imaging plane is much more confined allowing a better discrimination between e.g. signal from outside the cell and signal originating from the cytoplasm. The Nup82 example shown here clearly illustrates this point. Had one not known that the fluorescence is stemming only from the nuclear membrane, both, confocal as well as the 2D STED images, would have suggested that the labeling occurred throughout the nuclear volume. Only with 3D STED, a proper assignment of the spatial origin of the fluorescence signal becomes possible for three-dimensional structures below the diffraction limit. Furthermore, when performing co-localization analysis based on microscopic images, a better resolution in all three dimensions is of great importance to exclude co-localization events based on partial overlap of blurred objects.

5.2.4 Conclusion

In conclusion the presented STED microscope allows a flexible imaging approach. Depending on the need of the experiment the microscope allows super-resolution imaging in two colors in 2D or 3D mode in biological samples. 3D imaging can be done in two modes. Either only a single thin optical section is recorded (Section 5.2.3) or many sections are recorded to form a z image stack allowing a full 3D reconstruction (Section 5.2.2). A requirement for 3D image stack reconstruction is good labeling. If the density of labeling is relatively low (only one to two fluorophores per protein/structure of interest), a full 3D reconstruction is difficult due to photobleaching. However, 3D STED mode still allows an optical section to be taken with a sufficient signal-to-noise ratio.

To alleviate the problem of photobleaching in low fluorescent samples, the use of a reducing and oxidizing system (ROXS) commonly used in single-molecule spectroscopy could enable 3D image stack recordings of the aforementioned yeast cells [Kasper et al., 2010]. In short, ROXS, alongside the removal of oxygen in the sample, depletes the dye's triplet states and efficiently recovers oxidized and reduced states to prevent photobleaching. Furthermore it reduces blinking of the fluorophores [Vogelsang et al., 2008, Cordes et al., 2009]. Moreover, due to the nature of stimulated-emission depletion microscopy, adjusting the depletion intensity allows the user to tune the resolution of the microscope and concomitantly the photo-induced stress on the sample. This can prove useful when imaging under non-optimal conditions such as low labeling density and high photobleaching rates.

A further, more drastic approach to alleviate excessive photobleaching when imaging z-stacks would be the use of a two-photon-excitation source. It effectively reduces residual excitation above and below the focal plane because of the quadratic dependence of the excitation probability on the excitation beam intensity [Patterson and Piston, 2000, Denk et al., 2006]. Combining a two-photon excitation source in a 4π configuration would provide an even smaller excitation volume. The 4π configuration describes the coherent superposition of two excitation foci using two counter-propagating

beams focused by two opposing objective lenses [Hell and Stelzer, 1992]. This significantly increases the effective NA and thus resolution to about 150 nm in all dimensions [Nagorni and Hell, 1998]. This approach further reduces the exposure of fluorophores to excitation light in the sample above or below the effective PSF in a STED microscope when acquiring a z-stack. Optical sections to be scanned thus profit from the axial confinement of the diffraction-limited focal spot generated by the two opposing objective lenses.

Likewise, the depletion beams can be aligned to interfere in the same fashion as the excitation beams. The STED-XY beams need to constructively interfere in the focus while the axial depletion beams - without the need for a dedicated phase plate - are made to interfere destructively. This will cause a central zero in the axial depletion intensity distribution in the focal plane similar to the circular phase plate used in the herein presented setup - with the exception that the diffraction limited intensity distribution is made smaller due to the 4π configuration. The combination of 4π with STED microscopy has been experimentally demonstrated and termed IsoSTED [Schmidt et al., 2008]. It provides a nearly isotropic resolution of $\sim$ 30 nm in all three dimensions superior to any other STED microscope implementation published to date. However, the very elaborate alignment and instability of the interference patterns brought about by two opposing lenses has hindered its widespread use [Schmidt et al., 2008, 2009, Hell et al., 2009].

5.3 *Clostridium botulinum* C2 toxin

Bacteria of the genus *Clostridium* are anaerobic, spore-forming bacilli and are ubiquitously found in the world. While most clostridia are valuable for industrial applications in the field of solvent production or biodegradation, a few members of the family, most notably *C. botulinum, C. difficile, C. perfringens* and *C. spiroforme*, are serious pathogens causing diseases like botulism, gas gangrene, food poisoning and pseudomembraneous colitis [Stiles et al., 2011]. Some of these species secrete binary exotoxins, so called "AB" toxins, to their environment. While many bacteria show this ability, the

"A" and "B" part of some exotoxins of the aforementioned species do not assemble in solution. In that class of toxins the activated cell-binding "B" part is recruited to the target's cell surface by receptor-mediated binding of monomers which then assemble as homoheptamers. Subsequently, the enzymatic "A" component can dock to the homoheptamer and further translocates into the cytoplasm via acidified endosomes. The enzymatic "A" part then mono-ADP-ribosylates G-actin which results in the breakdown of the actin cytoskeleton and subsequent rounding of the cell and finally cell death [Barth et al., 2004, Stiles et al., 2011].

The prototype of this toxin family is the C2 toxin from *C. botulinum* [Ohishi et al., 1980]. The two components that make up the C2 toxin is C2I, the $\sim$ 49 kDa enzymatic part "A" and C2II(a), the $\sim$ 80 to 100 kDa binding/translocation component "B" ("a" for activated, denoting the ability to form monoheptamers). The activated "B" component binds to asparagine-linked carbohydrate structures on mammalian cells and forms a complex with C2I after heptamer formation [Eckhardt et al., 2000]. The complex is endocytosed by the target cell and acidification of the early endosome causes the heptamer to change its conformation to a pore, helping the enzyme component to translocate into the cytoplasm ([Barth et al., 2000], Fig. 5.9). The following work was done in collaboration with the group of Prof. Holger Barth (Ulm University, Ulm, Germany).

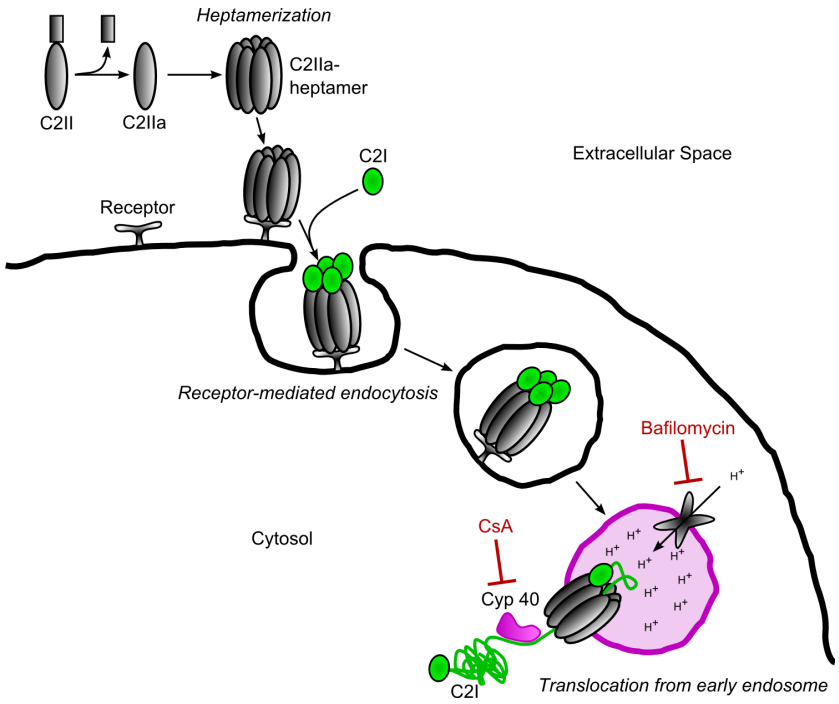

Figure 5.9: Schematic overview of the C2 intoxication pathway from proteolytic activation of C2II to C2IIa and following receptor-mediated endocytosis of C2 and final translocation of the enzymatic component C2I into the cytosol. Bafilomycin acts as a suppressor disabling acidification of early endosome thus trapping C2I in the vesicle. With the help of Cyclosporin A as a specific inhibitor, Cyp 40 was identified as necessary for translocation of C2I to the cytoplasm. Once in the cytosol, active C2I mono-ADP-ribosylates G-actin causing cell-rounding and finally cell death. Green and magenta color scheme represents objects labeled with Atto 590 and Atto 647N, respectively, throughout this section. Adapted from Barth et al. [2004].

5.3.1 Imaging C2I toxin component and Cyp 40 in fixed HeLa cells

In this investigation the setup built as part of this thesis was used to image HeLa cells which were intoxicated with fluorescently labeled C2I component and non-labeled C2IIa under various treatment conditions (Appendix A.9). *In vitro* experiments revealed an interaction of C2I with cyclophiline (Cyp) 40 as a helper protein during translocation to the cytosol. In a first try to confirm this *in vivo* a dual-color experiment was performed which com-

prised labeled C2I component (unspecifically labeled with Atto 590 using an amino-reactive dye) and indirect immunostaining of Cyp 40 with Atto 647N (Fig. 5.10 and 5.11).

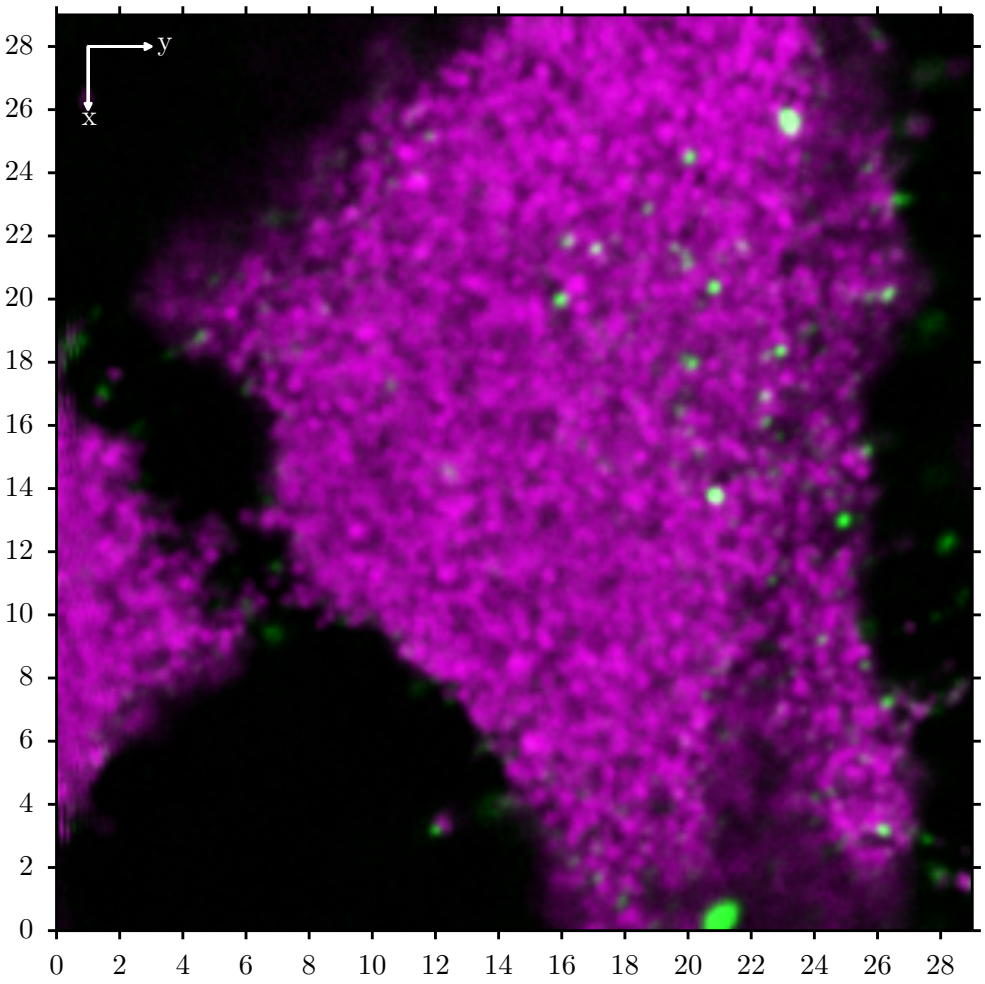

Figure 5.10: Dual-color diffraction-limited confocal image of fluorescently labeled C2I component (green, Atto 590) and immunostained Cyp 40 (magenta, Atto 647N) in a fixed HeLa cell. The image suggests co-localization of both labeled species indicated by the white color. The signal from Cyp 40 is present as a quasi-continuous layer throughout the whole cell. Image was post-processed for visualization purposes. Pixel dwell time was 200 μs at a pixel size of 100 nm. Axis scale in μm.

In standard diffraction-limited confocal imaging mode partial overlap of

both labeled species can be observed pointing to co-localization (Fig. 5.10, co-localization events appear white). While there are only a few spots of C2I observed in the confocal image, Cyp 40 is found throughout the cell resulting in an almost homogeneous Cyp 40 "layer". In super-resolution 2D mode however, the large Cyp 40 signal "layer" can be resolved to a very fine spotty pattern (Fig. 5.11). The increase in resolution revokes the suggested co-localization of C2I and Cyp 40. While both species lay in close proximity to another, no apparent co-localization can be seen. This exemplifies that co-localization analysis based on microscopic images with a resolution below the size of the objects under investigation can be misleading. In other words, co-localization can always be falsely observed when lowering resolution. In the case shown here a possible explanation why no co-localization was observed in fixed cells using 2D STED is that the interaction of C2I and Cyp 40 during translocation of C2I from early endosomes proven by *in vitro* experiments happens on a rather short timescale.

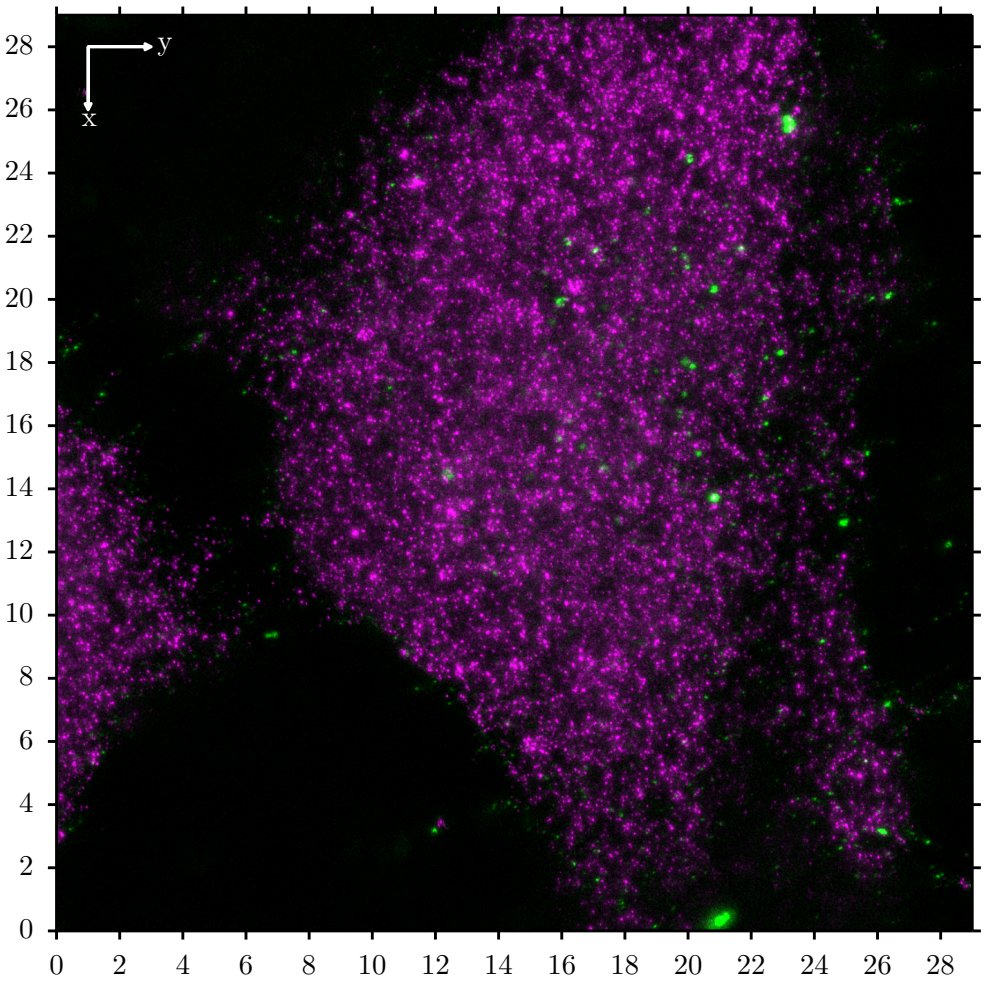

Figure 5.11: Dual-color 2D STED image of the same cell as in Fig. 5.10 showing the localization of the cyclophilin throughout the cell as a pattern of small spots. Due to improved resolution the conclusion that Cyp 40 and C2I co-localize, as suggested by the dual-color confocal image (Fig. 5.10), does not hold true anymore. Image was post-processed for visualization purposes. Pixel dwell time was 280 μs at a pixel size of 20 nm. Axis scale in μm.

5.3.2 C2I intoxicated cells inhibited by Cyclosporine A or Bafilomycin

When inhibiting Cyp 40 with Cyclosporine A (CsA) [Tanaka et al., 2013, Schiene-Fischer and Yu, 2001], the translocation of C2I from the endosome

to the cytosol is reduced leading to a non-toxic phenotype. The resulting phenotype was compared to cells not being protected by CsA and a control treatment with Bafilomycin. Bafilomycin is commonly used in the field of toxicology to detect toxin release from acidic compartments [Barth et al., 2000]. It specifically inhibits the vacuolar-type H^+-ATPase thereby trapping C2I in endosomes preventing translocation. When cells are intoxicated with C2 toxin, a concomitant addition of Bafilomycin will thus protect the cell from the enzymatic effect of C2 toxin. We therefore expected CsA-treated cells to have a similar phenotype as Bafilomycin-treated cells. Non-treated but intoxicated cells should show a different phenotype as the toxin can make the passage into the cytosol leading to the rounding of the cell and final cell death. Indeed, when imaging fixed cells with a phase contrast microscope a significant amount of rounded cells in the case of the sole addition of C2 is observed. On the contrary, Bafilomycin and CsA treated cells intoxicated with C2 show a viable phenotype (Fig. 5.12, upper row). This suggests that Cyp 40 is needed for the translocation of C2I into the cytosol. This finding is in line with *in vitro* experiments [Ernst et al., 2014].

When imaging in standard confocal and more so in super-resolution mode the distribution of C2I was analyzed in more detail (Fig. 5.12, middle and last row). In the presence of CsA the distribution of C2I is comparable to that of Bafilomycin treated cells. The spotty pattern consists of objects which are larger than the resolution of the STED microscope. Some of these spots show a non-homogenous signal throughout a single object. We attribute these spots to cellular compartments, most likely early endosomes. On the other hand, the C2I signal from untreated but intoxicated cells shows smaller and more abundant features. This finding fits the previous observation well. While suppressing Cyp 40 with CsA, the C2I component cannot translocate into the cytosol and stays trapped in endosomes which hold several toxins and thus appear as larger objects. The cell stays intact - it is protected from the enzymatic activity of the toxin. Without the protection of CsA or Bafilomycin the cell rounds up and dies. For this to happen, C2I must move from the endosomes to the cytosol to exert its enzymatic action. In the cytoplasm the toxin is not concentrated in any vesicle thus dispersing freely

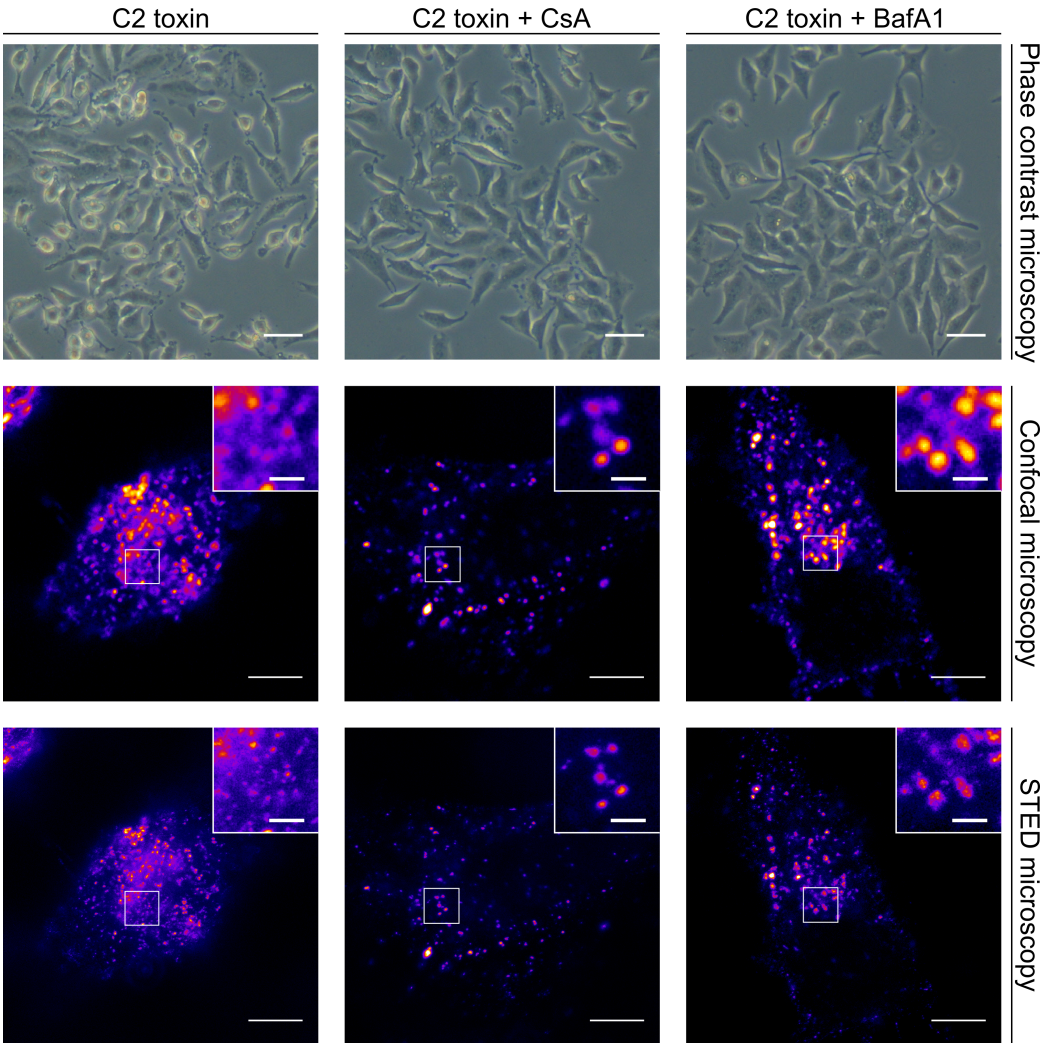

Figure 5.12: Comparison of cell phenotypes when intoxicated with C2 toxin alone, CsA and C2 toxin or Bafilomycin and C2 toxin. CsA protects cells from the enzymatic action of C2 thus showing no sign of intoxication (middle column) similar to Bafilomycin treated cells (right column). On the contrary, C2 treated cells (left column) are abundantly rounded indicating effects of the actin-degrading activity of active C2 toxin. Insets show magnified part of image as indicated by white box. Contrast was optimized and a multi-color look-up-table was applied for the purpose of visualizing a higher dynamic range. Pixel dwell times were 200 μs at a pixel size of 50 nm (confocal images) or 20 nm (STED images). Scale bars correspond to 50 μm in the phase contrast images, 5 μm in the confocal/STED panels and 1 μm in the insets.

leading to the smaller observed structures seen in Fig. 5.12 (left bottom panel).

5.3.3 Imaging C2I and early endosomal marker EEA1

Following up on earlier experiments employing dual-color confocal laser scanning microscopy to image C2I alongside the early endosomal marker anti-Rab5 in rat astrocytes [Haug et al., 2003] we imaged early endosome antigen 1 (EEA1) and C2I in fixed HeLa cells. EEA1 specifically labels early endosomes (similar to anti-Rab5) at which stage the translocation of C2I into the cytosol occurs [Haug et al., 2003]. When adding Bafilomycin to the cells maturation of the endosomes is stopped and thus we expected to see thorough co-localization of the early endosomal marker and C2I because of its entrapment and accumulation in these types of vesicles. However the measurements performed so far do not show the expected degree of co-localization (Fig. 5.13).

In comparison we studied cells not treated with Bafilomycin (allowing C2I to exit early endosomes). Surprisingly, the difference in co-localization to Bafilomycin treated cells is negligible (Fig. 5.14). The reason for this observation could be manifold and only a guess can be made as to why C2I does not seem to localize in EEA1 stained early endosomes. Compared to early work that showed co-localization in Bafilomycin treated cells [Haug et al., 2003], the cell type used in the early work (rat astrocytes) is different from our experiments (HeLa cells). While it is hard to imagine that an important pathway such as endosomal transport fundamentally differs from cell type to cell type, it could be that the inoculation time before fixation differs and needs to be optimized. Indeed, Nagahama et al. [2014] recently showed that in MDCK cells, C2I is only observed in early endosomes ~ 5 min. after intoxication with C2IIa and C2I. After this time period, C2I quickly translocates into the cytoplasm, while C2IIa is either transported to the plasma membrane through recycling endosomes or degraded in lysosomes [Nagahama et al., 2014]. This data could indicate that for our first experiments in HeLa cells, the inoculation time of the toxin prior to fixation was too long and C2I

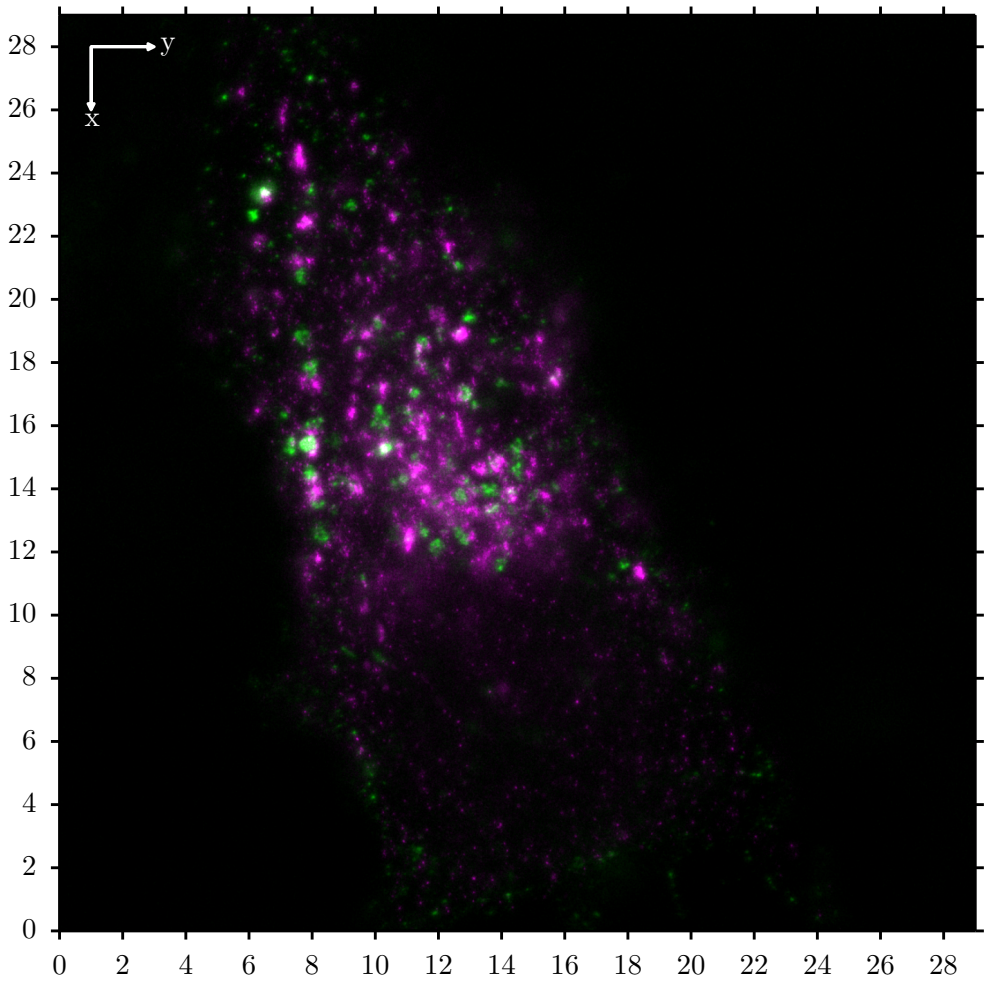

Figure 5.13: Dual-color STED image of C2I (green, Atto 590) and EEA1 (magenta, Atto 647N) in HeLa cells treated with Bafilomycin. The expected strong co-localization of both species brought about by the addition of Bafilomycin can not be observed. Only individual events of co-localization are present but are not comparable to previous works. Image was post-processed for visualization purposes. Pixel dwell time was 200 μs at a pixel size of 20 nm. Axis scale in μm.

had therefore already left the early endosomes. Further experiments have to be conducted that go beyond the initial first trials shown here. While a wrong timing as mentioned before can explain that only little co-localization in the experiments without Bafilomycin was observed, it falls short as an explanation for the results measured with the inhibitor Bafilomycin. Interestingly,

when comparing Fig. 5.13 to Fig. 5.14, one finds that in Bafilomycin treated cells, EEA1 labeled structures are more abundant compared to the cells not treated with the inhibitor. This seems to be in line with the expected effect of the inhibitor which arrests the maturation of early endosomes. However, it is not clear whether Bafilomycin stops endosomal maturation at the stage of early endosomes which can be probed by EEA1 or at later stages of the endosomal maturation pathway. Different results have been brought forth regarding this maturation stop caused by Bafilomycin and a cell-type dependency seems likely [Huotari and Helenius, 2011]. Interestingly, we observed more C2I labeled structures in non-Bafilomycin treated cells (Fig. 5.14) versus inhibited cells (Fig. 5.13). A highly speculative explanation for this result could be that some C2I trapped in early endosomes is recycled by Bafilomycin inhibited cells in the 2 h time frame for the experiments conducted. This discussion makes it obvious that more stringent experiments with the inoculation time as the variable parameter have to be performed to understand the complex mechanism and explain the initial results presented in this section.

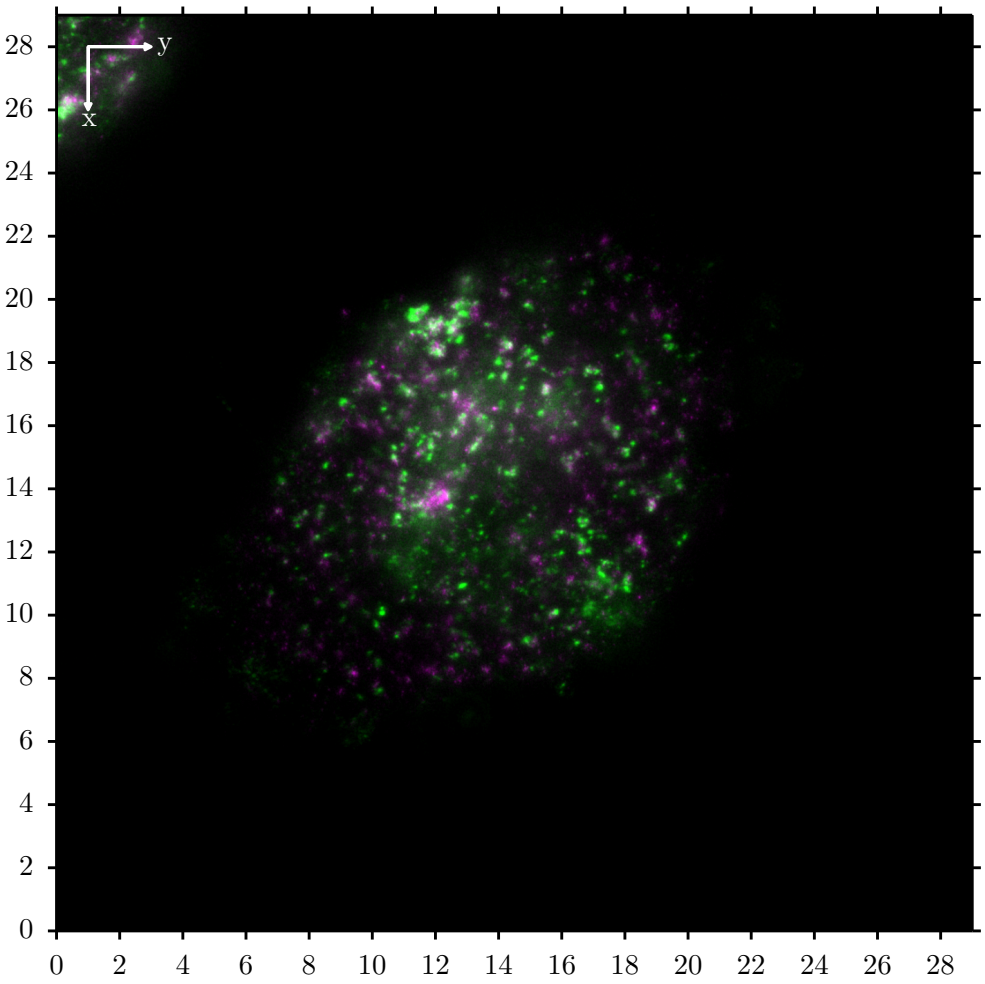

Figure 5.14: Dual-color STED image of C2I (green, Atto 590) and EEA1 (magenta, Atto 647N) in HeLa cells. Compared to Fig. 5.13, the degree of co-localization unexpectedly does not differ in these experiments. A probable cause for the few co-localization events observed is that C2I already left the early endosomes during the 2 h toxin inoculation time prior to fixation [Huotari and Helenius, 2011]. Image was post-processed for visualization purposes. Pixel dwell time was 200 μs at a pixel size of 20 nm. Axis scale in μm.

5.3.4 Conclusion

We demonstrated that using super-resolution STED microscopy we could image fluorescently labeled C2I component and attribute changes in the apparent distribution to the effect of CsA as a suppressor of Cyp 40. The improved

resolution helped in ruling out false co-localization suggested by previous experiments using diffraction-limited confocal microscopy when imaging Cyp 40 and C2I indicating interaction of both species on a rather short time scale. While co-localization of trapped C2I and endosomes did not yield the expected results, more stringent experiments than these initial trials have to be conducted to test the effect of experimental parameters on the result. Especially the duration of incubation of the cells with the toxin prior to fixation seems important in order to capture the state of the cell when up-taken toxin is still present in early endosomes.

5.4 Imaging scaffold proteins in chemical synapses

Chemical synapses play a pivotal role in the transfer of information between cells in the central nervous system. These cell-cell contacts are highly specialized structures made up of a presynaptic part, the synaptic cleft and a postsynaptic part. The presynaptic part comprises the presynaptic nerve terminal called bouton which is loaded with neurotransmitter-filled vesicles that fuse with the presynaptic plasma membrane at the active zone. Electron microscopy determined the synaptic cleft to be around 20 nm wide, constituting a discontinuity in the flow of information from one cell to the other [Harris and Weinberg, 2012]. In asymmetric, type I glutamatergic synapses the postsynaptic part is made up of neurotransmitter reception machinery and the postsynaptic density (PSD, [Harris and Weinberg, 2012]). Asymmetric synapses are excitatory synapses increasing the probability of an action potential to occur in the postsynaptic partner cell [Purves et al., 2004]. They are mostly found on dendrites and dendritic spines while their shape and size varies greatly even on a single dendrite ([Harris and Weinberg, 2012], Fig. 5.15).

As an initial trial to image chemical synapses we chose a standard indirect immunostaining approach to selectively label the presynaptic marker Bassoon and the postsynaptic protein Homer 1 (Appendix A.10) in embryonic hippocampal neurons from rat brain (fixed and labeled after 14 days *in vitro*) in collaboration with the group of Prof. Tobias Böckers (Ulm Uni-

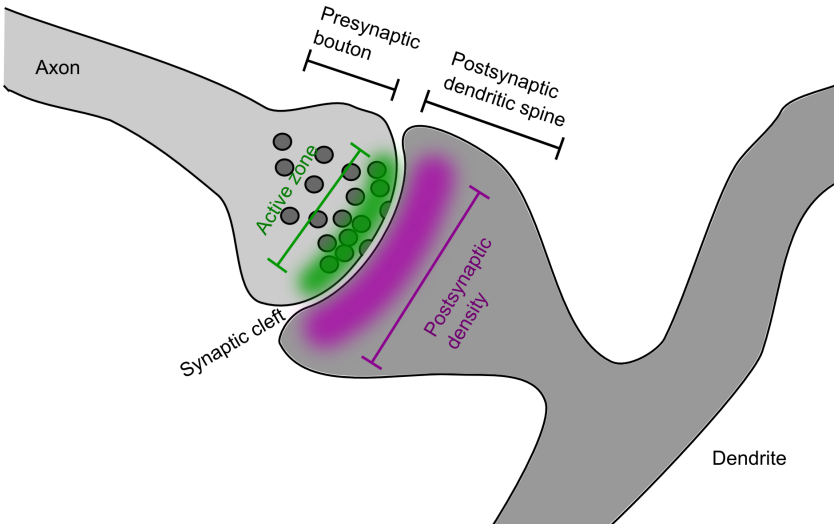

Figure 5.15: Schematic overview of a glutamatergic chemical synapse made up of a presynaptic bouton loaded with neurotransmitter-filled vesicles which can fuse with the presynaptic membrane at the active zone (green). At the opposing side of the synaptic cleft, the postsynaptic dendritic spines contains the prominent postsynaptic density (magenta).

versity, Ulm, Germany). Bassoon is one of the largest proteins (420 kDa) found specifically in the active zone [Schoch and Gundelfinger, 2006] and acts as a scaffold protein important in synapse formation [Waites et al., 2013]. Homer 1 is a scaffold protein found in the PSD where it plays a role in Ca^{2+} signaling and as a regulator for synaptic strength and dendritic morphology [Foa and Gasperini, 2009]. These two proteins have been previously imaged using STORM super-resolution microscopy and shown to be viable position reference markers to investigate synapse structure as their distance is consistent across synapses [Dani et al., 2010].

The imaging of synapses greatly benefits from using the STED setup. In diffraction-limited confocal mode synapses appear as smeared-out, partially overlapping, sometimes elongated spots (Fig. 5.16). Any potential details in the substructure are lost due to limited optical resolution. When using STED 2D mode objects separated by a cleft appear very similar to the study of Dani et al. [2010] (Fig. 5.17). A great variability in synapse shape was observed. Most synapses appear as two fairly straight lines parallel to each other while

others exhibit a more pronounced bent shape (Fig. 5.17 and 5.18 A). Synapse size also differed among synapses in some cases exhibiting what appear to be multisynaptic contacts (Fig. 5.18 B, [Shepherd and Harris, 1998]). The variability in shape and size has so far been described in the literature mostly based on electron microscopic images.

As we could show in the case of STED microscopy, it has the potential to unravel the complex structure of chemical synapses. As a fluorescence microscopy technique it brings along a set of advantages compared to EM imaging such as a less elaborate sample preparation and the possibility to image live cells. This has in fact been recently shown in the case of live-cell STED microscopy and will greatly improve our understanding of synaptic plasticity [Nägerl et al., 2008, Takasaki et al., 2013]. In the future we aim at determining the localization of various pre- and postsynaptic scaffold proteins important for the correct function of chemical synapses relative to the position of Bassoon and Homer across different parts of the brain. While the initial data shown was recorded using cultured neurons, we currently work on imaging synapses directly in cryostat cut brain slices roughly 10 μm thick.

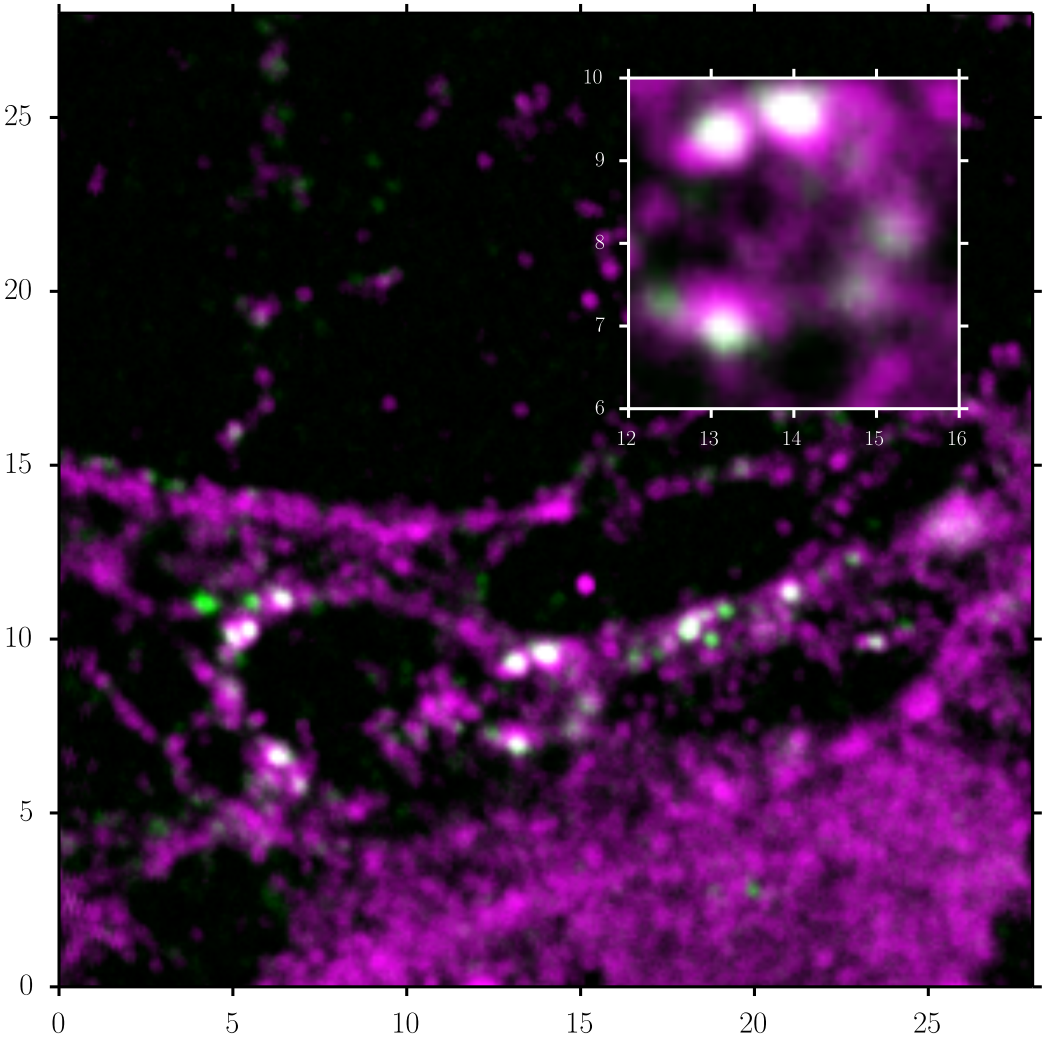

Figure 5.16: The presynaptic protein Bassoon (Atto 594, green) and postsynaptic Homer 1 (Atto 647N, magenta) imaged in diffraction-limited confocal mode. Individual synapses are visible as partially white objects while structural details are not discernible due to limited optical resolution. Inset shows zoomed in section. Pixel dwell time was 200 μs at a pixel size of 100 nm. Axis scales in μm. Image was post-processed for visualization purposes.

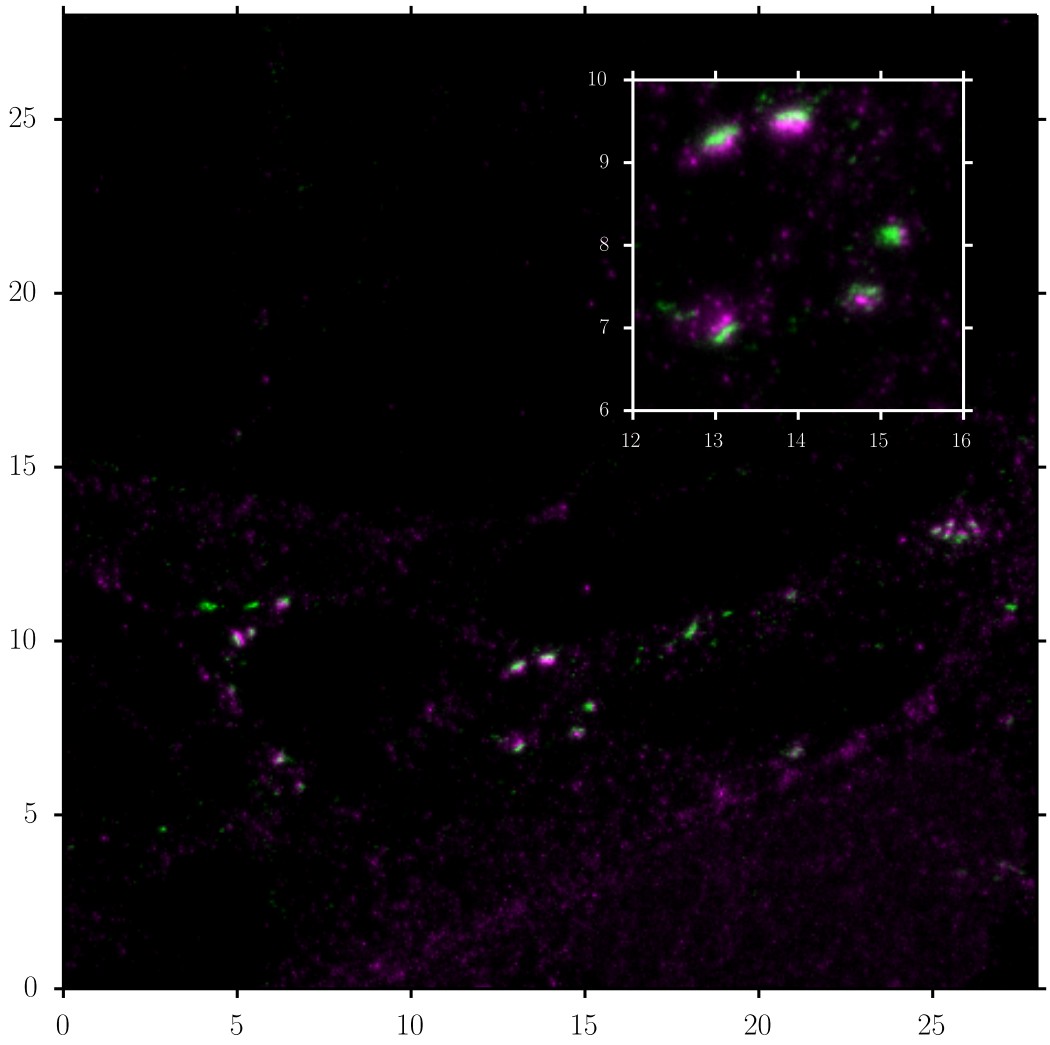

Figure 5.17: The same area as in Fig 5.16 imaged in STED 2D super-resolution mode (Bassoon = Atto 594, green; Homer 1 = Atto 647N, magenta). The benefits of using super-resolution mode are most evident when comparing the zoomed-in inset to the inset shown in Fig 5.16. Individual synapses and their substructure with separated pre- and postsynaptic markers are resolved. Pixel dwell time was 400 μs at a pixel size of 20 nm. Axis scales in μm. Image was post-processed for visualization purposes.

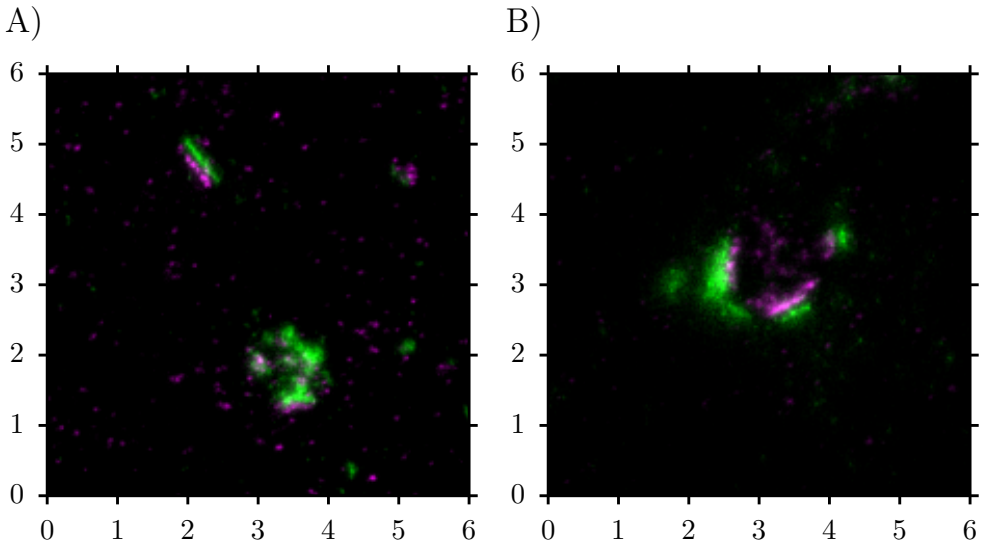

Figure 5.18: Various synapse shapes are visible in super-resolved images (Bassoon = Atto 647N, green; Homer 1 = Atto 594, magenta). Individual synapses and their substructure are resolved with a cleft separating the pre- and postsynaptic markers. A) Exemplary image showing straight and bent synapses of various sizes. B) Exemplary recording of possible multisynaptic contact. Pixel dwell time was 400 μs (panel A) and 300 μs (panel B) at a pixel size of 20 nm. Axis scales in μm. Image was post-processed for visualization purposes.

5.5 Conclusion and outlook

In this chapter the STED microscope built as part of this thesis was put to test in a variety of applications. From the data presented the advantage of STED microscopy over conventional, diffraction-limited fluorescence microscopy becomes most evident in the context of biological imaging. The gain in information that comes along with improved optical resolution is striking. The design allows a direct comparison between conventional diffraction-limited confocal imaging and super-resolution STED microscopy. This was used to directly validate an intensity-based, absolute quantification algorithm counting nanoparticles in diffraction-limited images (Section 5.1).

With the setup at hand we could show that the rather complex setup presented and characterized in Chapter 4 is able to provide flexible simulta-

neous dual-color super-resolution imaging in cells in either 2D or 3D mode. With the option of tuning the depth of view in 3D mode, structural details in the crowded environment of the nucleus could be resolved when recording image z-stacks. This improved optical sectioning capability comes at the cost of increased photobleaching in 3D mode due to the higher intensity used for depletion. One should note that this is only limiting for relatively low labeling densities as shown for yeast cells using chromobodies as fluorescent markers. However, even at low labeling densities a single optical slice with super-resolution in all three dimensions can still be recorded (Section 5.2.3).

Since the data shown are initial experiments we expect to improve this situation by applying a ROXS protocol to increase fluorophore stability and photon output (Section 5.2.4). A further interesting approach to reduce photobleaching when recording z-stacks is to lower the exposure of fluorophores to excitation light prior to actually being detected by confining the excitation spot size using a 4π configuration or by reducing the excitation probability outside the diffraction-limited spot using a two-photon excitation source. A combination of these techniques will provide the best performance at the cost of increased experimental complexity (Section 5.2.4).

Regarding the C2 toxin project (Section 5.3), which did not yield the expected results in terms of co-localization events, further experiments have to be conducted to shed light on the initial results obtained so far. Conducting time-series experiments with a varying inoculation time of the toxin prior to fixation is a promising approach to be able to image the toxin component C2I on its way through early endosomes into the cytosol. The data presented underlines the necessity to conduct super-resolution microscopy to rule out false-positive co-localization events due to poor resolution.

We could successfully show that imaging synapses in hippocampal neurons using STED microscopy allows to discern pre- and post-synaptic proteins and even more so, individual synapse shapes (Section 5.4). This project will be expanded in future experiments to image proteins of the ProSAP/Shank family to elucidate their role in the correct functioning of the synapse in the light of autism disorders.

The setup described can be readily extended to a three-color (or even

more) STED microscope by the addition of time-correlated single photon counting hardware similar to the work by Bückers et al. [2011] to assign the recorded signal to a channel based on differences in the lifetimes of fluorophores with a similar emission spectrum. This brings along the advantage that the excited state of two fluorophores is depleted by the same stimulating beam intensity distribution making co-localization analysis more robust.

The incorporation of a faster and more powerful modern laser source as presented by Göttfert et al. [2013] will help to further increase resolution and will yield a reduced complexity of the setup due to the ability to use a single depletion beam for lateral or axial resolution improvement for both channels making alignment less elaborate. A concomitant change will be to switch to beam scanning to make use of the higher repetition rate of the modern lasers (several 10's of MHz) allowing faster image acquisition than is currently possible. The pulse durations of these modern, high-power lasers is on the order of a nanosecond and, thus, the use of the presented T-STED scheme is advisable (Chapter 3).

Finally, the setup could be expanded to a 4π STED configuration. This will further improve resolution (especially along the optical axis) and minimize photobleaching due to the smaller PSFs at the cost of highly increased setup complexity (see Section 5.2.4).

To conclude, the presented data exemplifies the successful design and use of the microscope built as part of this thesis while technical improvements discussed above such as using a modern laser source will likely extend the capabilities of the microscope in the future.

Chapter 6

Summary

The focus of this thesis lies in the theoretical description on the improvement of STED microscopes by the use of time-gating and the design, building and consequent application of a two channel STED microscope with the possibility of breaking the diffraction limit in all three dimensions. In the following paragraphs, the major parts of this work are summarized.

T-STED: Time-gating of the photons detected in a pulsed and especially CW-STED microscope provide the means to improve the resolution beyond what classical STED microscopes can achieve. The physical basis lies in the photophysical processes of fluorophores subjected to excitation and depletion light. In a standard STED microscope, the varying intensity of the depletion light across its focal pattern is used to deplete the excited state of the fluorophore from the periphery towards the center of the excitation spot, yielding a small spot left to fluoresce which is not fundamentally limited in size by diffraction. Thus, by being able to discriminate between the two emission channels - spontaneous vs. stimulated emission - and only recording the former, diffraction unlimited resolution is achieved. However, as the process of stimulated emission competes with spontaneous emission in such a setting, the lifetime of the excited state is also altered depending on the rate of stimulated emission. In a STED microscope with a varying STED beam intensity across the focus, this causes the lifetime to vary across the PSF accordingly. Thus, spatial information is encoded in the arrival time of

the detected spontaneously emitted photons. By time-gating the detection and selectively discarding photons arriving before a certain point in time after excitation, the resolution can be significantly increased. Our theoretical predictions were practically implemented by Vicidomini et al. [2011]. Time-gating is now a standard approach to increase resolution in commercial STED microscopes by Leica Microsystems GmbH, PicoQuant GmbH and Abberior Instruments GmbH indicating the importance and feasibility of our theory. This work was originally published in Optics Express, 19, Issue 5, 2011 with the title *Time-gating improves the spatial resolution of STED microscopy* [Moffitt et al., 2011]. See Chapter 3 for details on T-STED.

3D dual-color STED microscope: A working STED microscope capable of recording two channels simultaneously and providing a lateral and axial resolution of $\sim$ 35 nm and $\sim$ 90 nm, respectively, was built as part of this thesis. The setup constitutes a highly integrated, novel design by the use of a single super-continuum laser source. The microscope's performance was tested on a variety of samples ranging from single-molecules to complex biological samples and compares well to published data from similar, albeit less integrated setups [Wildanger et al., 2008, 2009]. Due to the flexible design of the setup the user can tune lateral and axial resolution independently for use in different experimental settings. The sensitivity allows the imaging of single molecules used as test objects for resolution measurements. The results including the design of the setup as well as first test measurements were originally published in Optics Express, 22, Issue 6, 2014 with the title *Simultaneous dual-color 3D STED microscopy* [Osseforth et al., 2014]. See Chapter 4 and Appendix B for details on the microscope.

Particle_in_cell-3D, an ImageJ macro: Due to the superior resolution of the built microscope over conventional confocal microscopes it was successfully put to use to count fluorescent beads in order to assess the performance of an intensity-based counting algorithm coined Particle_in_cell-3D. This algorithm, implemented as a macro for the widely acclaimed open-source software ImageJ, is able to quantify nanoparticles in diffraction-limited images even when not optically resolvable. It does so by segmenting the blurred objects in an image into smaller objects and subsequently measures their in-

tegrated intensity. If the intensity of a single bead is known, the algorithm can count objects hidden beneath the fluorescent spot in an image simply by dividing the measured integrated intensity of an unresolvable fluorescent object by the intensity of a single bead. The macro's performance was successfully tested by comparing counts measured by the macro to images made in super-resolution mode with the STED microscope which is able to optically resolve individual nanoparticles with a diameter of 100 nm. The results were originally published in Nanomedicine, 8, Issue 11, 2013 with the title *A fast analysis method to quantify nanoparticle uptake on a single cell level* [Torrano et al., 2013]. The algorithm was successfully put to use in a subsequent publication [Blechinger et al., 2013]. See Section 5.1 for details regarding the macro.

Imaging yeast cells using nanobodies: Yeast cells were imaged using novel small antibody fragments called nanobodies. While having the advantage to cross the cell membrane of yeast cells without prior digestion the direct immunolabeling approach does not yield the fluorescence intensity as standard indirect immunolabeling methods employing a primary and secondary antibody. Nevertheless, yeast cells were successfully imaged in 2D and 3D STED mode exemplifying the validity of the technique. In the case of the nucleoporin Nup82, only in 3D STED mode the detected fluorescence signal could be correctly assigned to the nuclear membrane. Further experiments are planned in yeast cells focusing on the spatial and temporal distribution of eukaryotic transcription factors.

Imaging *Clostridium botulinum* C2 toxin in fixed HeLa cells: Initial experiments focused on the interaction of Cyp 40 with C2I component after release from early endosomes. To this end, fluorescently labeled C2I toxin was imaged for the first time with STED microscopy in fixed cells. The increase in resolution made it possible to rule out false positive colocalization with Cyp 40 initially observed using diffraction-limited confocal mode, indicating a rather fast interaction time of the two proteins. A first attempt to image the toxin component inside early endosomes from which it is released into the cytosol after endocytosis did not yield the expected results as suggested by biochemical analysis. However, images taken sug-

gest a release from early endosomes in experiments using Bafilomycin as an inhibitor of endosomal release of C2I toxin. This data contributed to the results published online in the Journal of Molecular Biology, 2014 with the title *Cyclophilin-Facilitated Membrane Translocation as Pharmacological Target to Prevent Intoxication of Mammalian Cells by Binary Clostridial Actin ADP-Ribosylated Toxins* [Ernst et al., 2014]. See Section 5.3 for details on the project.

Imaging scaffold proteins in chemical synapses: Initial images are presented showing chemical synapses in fixed cultured hippocampal neurons. Two scaffold proteins - the presynaptic protein Bassoon located in the active zone and the postsynaptic protein Homer 1 present in the PSD - were labeled using a standard indirect immunolabeling approach. A variety of differently shaped synaptic contacts were imaged in STED mode normally hidden beneath the diffraction limit. Initial data looks very promising and comparable to data published using stochastic optical reconstruction microscopy [Dani et al., 2010]. Further experiments focusing on the location of scaffold proteins of the ProSAP/Shank family within the synapse are planned. See Section 5.4 for details on the project.

Taken together, this work presents novel techniques which have been successfully applied to present-day technological and biological questions validating its use for the scientific community. A variety of collaborations emerged as part of this thesis which will prove the usability of the presented STED microscope in the future.

Appendix A

Methods

A.1 Cover slips

Cover slips used were mainly precision cover slips with a specified thickness of 170 μm $\pm$ 5 μm purchased from Carl Roth GmbH & Co. KG. These cover slips are not necessary for obtaining high-quality images provided that the embedding medium and the immersion-oil have the same refractive index as the glass used ($\sim$ 1,524 at 546 nm). Cover slips were cleaned with pure ethanol using lens paper (Thorlabs, USA).

A.2 Mounting medium

Self-prepared varieties of Mowiol (Polyvinylalcohol/PVA, Sigma-Aldrich, Germany) as well as 2,2'-thiodiethanol (TDE) were used to embed objects between objective slide and cover slip (Appendix A.1). Mowiol was mainly used in conjunction with non-biological matter whereas TDE was used for biological samples. TDE was prepared according to the protocol given by Staudt et al. [2007]. In short, pure TDE is diluted to 97 % with phosphate buffered saline (PBS) and subsequently adjusted to a pH of 7.5. This last step is the most demanding one as measuring the pH using an electrode in a highly viscous medium requires patience. When adjusting the pH one should add a drop of HCL and wait for approx. 10 minutes until the reading on the

pH meter has successfully stabilized. If the targeted pH value is overshot, one will need to further dilute the TDE thus changing the refractive index of the medium. Prepared TDE aliquots are stored airtight in the fridge but can be left at room temperature once opened (usable for weeks).

Mowiol was prepared in two ways. In the one case, Mowiol pellets were simply dissolved in water overnight on a shaker in a Falcon tube to a concentration of 2 %. This results in a non-viscous fluid which performs well when embedding drop-cast samples. The other procedure calls for more elaborate preparation steps. After mixing 2.4 g of Mowiol to 6 g of glycerol, 6 ml H_2O was added and left at room temperature to partially dissolve. After adding 12 ml of 0.2 M Tris-HCl (pH 8.5) the mixture is heated to approx. 50°C while stirring to help dissolve the Mowiol. The solution at this point will look like foam. To yield liquid solution the mixture is centrifuged for a couple of minutes at 5000 g. Finally, 1,4-diazabicyclo[2.2.2]octan (DABCO, Roth GmbH, Germany) is added to a concentration of 2.5 % as an antifading agent. Aliquots are stored airtight at -20°C. Once opened aliquots are good for weeks provided the container is airtight. This variety of Mowiol is much more viscous than the one described above. This led to problems when using it for the embedding of weakly-attached yeast cells on cover slips. As they were frequently washed away, the simple, less viscous variety of Mowiol was used in this case.

A.3 Gold nanoparticle sample preparation

Gold nanoparticles with a diameter of 80 nm were acquired from BBI Solutions (EM.GC80, England). After sonification for 10 min, 20 μl of a 1:1000 diluted gold bead solution (in ethanol) was drop-casted onto cleaned cover slips (Appendix A.1) and left to dry. Subsequently, the sample was mounted in approx. 5 μl Mowiol mounting medium (Appendix A.2). An alternative approach is to centrifuge 20 μl of stock gold bead solution and re-suspend the pellet in Mowiol to a dilution of 1:1000. Afterwards the solution is spin-coated onto a cover slip and mounted in Mowiol as mentioned above. Both methods work well but the spin-coating seems to better disperse the gold

beads onto the surface. The quality of the sample can be easily assessed by imaging the sample with the STED beam. If most donuts appear to have the same shape and intensity, gold beads are monodispersed.

A.4 Fluorescent bead sample preparation

A variety of fluorescent beads were imaged during the course of this study such as 20 nm and 100 nm Fluospheres from Invitrogen (colors red, crimson and dark red) as well as custom-synthesized double-labeled silica beads with a diameter of 50 nm (Micromod, Germany). After sonification for 10 min, 20 μl of a 1:1000 diluted fluorescent bead solution was drop-casted onto cleaned cover slips (Appendix A.1) and left to dry. Subsequently, the sample was mounted in approx. 5 μl Mowiol or TDE mounting medium (Appendix A.2). In the case of TDE, the cover slip was further sealed with clear nail polish.

A.5 Single-molecule sample preparation

100 μl Neutravidin (0.5 mg/ml in PBS) was drop cast onto a cleaned cover slip (Appendix A.1) and incubated for 30 min. After incubation, cover slips were washed three times with 1 ml PBS. 100 μl of a 1 nM solution of a 1:1 mixture of 60 bp long DNA molecules internally labeled with either Atto 590 or Atto 647N and terminally labeled with biotin (IBA GmbH, Germany) was drop-cast onto a coated cover slip and left to incubate for 15 min at room temperature. Subsequently, cover slips were rinsed three time with 1 ml PBS to remove unbound oligomers. Finally, cover slips were mounted in TDE embedding medium (Appendix A.2). Sequence data (5' to 3' end, biotin on 5' end) of the DNA molecules used are GAG ACA CTA XTA TGG TGG GCC AAT GAC ACC AAT TAC GCA GAC TAT GAA TAT TGA TAC GGT (X denoting Atto 590 on dT-NH_2) and ACC GTA TCA AYA TTC ATA GTC TGC GTA ATT GGT GTC ATT GGC CCA CCA TAA TAG TGT CTC (Y denoting Atto 647N on dT-NH_2).

A.6 Indirect immunostaining of FG-repeat region and Tpr

Cells were seeded directly onto cleaned cover slips (Appendix A.1) placed in multi-well plates. After fixation in 2 % formalin (diluted in PBS) for 10 min following permeabilisation with 0,5 % Triton X-100 for 10 min, cells were blocked with 2 % bovine serum albumine (BSA, in PBS) for 30 minutes at room temperature. Subsequently, primary antibodies mouse-αFG-repeat (1:200, Abcam, USA) and rat-αTpr (1:10) were incubated for 1.5 h at room temperature. After washing three times in PBS samples were incubated with labeled secondary antibodies donkey-αMouse-Alexa 594 (1:500, Invitrogen, USA) and goat-αRat-Atto 647N (1:100, Alexis Biochemicals, USA) for an hour at room temperature. Following labeling, samples were washed three times in an excess volume of PBS and post-fixed in 2 % formalin (in PBS) for 10 min. After two more washing steps in PBS samples were washed two times in H_2O to remove salts. Finally, cells were mounted in TDE embedding medium (Appendix A.2) or Vectashield (Vector Laboratories, USA). Samples were prepared by Andreas Maiser (LMU, Munich, Germany).

A.7 Labeling of post-replicative DNA using 5-ethynyl-2'-deoxyuridine (EdU)

Labeling of post-replicative DNA was performed in conjunction with indirect immunolabeling using antibodies. C2C12 wildtype cells were seeded onto cover slips (Appendix A.1) in multi-well plates. Pulse labeling with EdU (1:500) was performed for 15 min. Fixation was done for 10 min in 2 % formalin (in PBS) after which permeabilisation was performed using methanol for 5 min. Subsequently, cells were blocked in 2 % BSA for 30 min at room temperature. The click chemistry construct ClickIT labeled with Alexa 594 (Invitrogen) was used to specifically label incorporated EdU. Incubation was performed for 1.5 h at room temperature in conjunction with the primary mouse-αPCNA antibody (1:20). After three washing steps in

great excess of PBS cells were incubated with the secondary antibody goat-αMouse-Atto 647N (1:200, Sigma-Aldrich). Subsequent steps follow the protocol given in Appendix A.6. Samples were prepared by Andreas Maiser (LMU, Munich, Germany).

A.8 Yeast nanobody labeling

Yeast cells do not adhere on cover slips and thus tend to float when using non-hardening embedding medium such as TDE-based medium. It is therefore necessary to use Concanavilin A coated cover slips to secure the cells to the surface. Concanavilin A is a lectine which binds to carbohydrates on the yeast cell surface. 10 μl Concanavilin A solution (20 mg/ml in H_2O, Sigma-Aldrich) was drop-cast on a cleaned cover slip (Appendix A.1) and left to dry for 20 min at room temperature.

To label yeast cells using nanobodies instead of regular full-size antibodies, cells were fixed in solution with 700 μl 37 % formaldehyde per 5 ml yeast cell suspension for 30 min at room temperature. Following fixation the cell suspension was centrifuged for 3 min at 4000 g and the supernatant discarded. Cells were washed three times in 1 ml buffer #1 (1x PBS with 0.1 % Tween 20) and subsequently permeabilized for 10 min in 1 ml buffer #2 (1x PBS with 0.5 % Triton X-100). After two more washing steps with buffer #1, the cell pellet was blocked with 500 μl buffer #3 (buffer #1 with 4 % BSA) for 10 min. After centrifugation for 3 min at 4000 g, the cell pellet was resuspended in 200 μl buffer #3. 1 μl nanobody solution labeled with Atto 594 (Chromotek, Germany) was added and incubated for 1 h at room temperature. After labeling cells were washed three times in PBS and finally resuspended in 50 μl PBS. 50 μl of cell suspension was drop cast onto a Concanavilin A-coated cover slip and incubated for 10 min. Subsequently, cover slips were washed three times in water to remove non-attached cells. Finally, cover slips were mounted in 7 μl 2 % Mowiol solution (Appendix A.2). Samples were prepared by Susanne Ude (Ulm University, Ulm, Germany).

A.9 C2 intoxication of HeLa cells and immunostaining of Cyp 40 and EEA1

HeLa cells were seeded onto 15 mm diameter round, cleaned cover slips (Appendix A.1) in 12 well plates and incubated for two days. Depending on the treatment cells were pre-incubated for 30 min at 37°C with 20 μM Cyclosporine A (Sigma-Aldrich) or 100 nM Bafilomycin A1 (Calbiochem) or left untreated. Subsequently, cells were intoxicated with either an inactive double mutant of C2I (C2IE387/389Q) and C2IIa or active wildtype C2I and C2IIa. In both cases C2I was fluorescently labeled with Atto 590 using a N-hydroxysuccinimidyl ester for amino labeling. Concentration of C2I was 500 - 1000 ng/ml and 1 - 4 μg/ml for C2IIa. After 2 h at 37°C cells were washed with PBS two times and then fixed in 4 % paraformaldehyde for 20 min at room temperature. Following the fixation the cells were washed in PBS and permeabilized in 0.4 % Triton X-100 (in PBS) for 5 min at room temperature in the dark. After three washing steps in PBS the cover slips were transferred to a wet chamber and blocked with dry milk (90 μl per cover slip) for 30 min at 37°C in the dark. After one washing step in PBS cells were incubated with primary rabbit antibodies αCyp 40 (1:1000, Thermo Fisher Scientific), αEEA1 (1:100, Acris Antibodies GmbH) or secondary antibody goat-αRabbit-Atto 647N (1:2000, for control, Sigma-Aldrich) for 30 min at 37°C in the dark. Following the staining, the cover slips were washed three times in excess of PBS. Subsequently, cover slips were incubated with goat-αRabbit-Atto 647N antibody (1:2000, Sigma-Aldrich) for 30 min at 37°C in the dark. After three final washing steps in PBS cover slips were once washed in pure H_20 to prevent formation of salt crystals and then mounted in 4 μl TDE embedding medium (Appendix A.2) onto objectives slides. Afterwards, cover slips were sealed with transparent nail polish and imaged using the STED microscope. Samples were prepared by Katharina Ernst (Ulm University, Ulm, Germany).

A.10 Immunostaining of cultured hippocampal neurons

Neurons from DIV 14 (days in vitro, primary hippocampal cell culture from day 18 embryonic rats) grown on cover slips (Appendix A.1) in multi-well plates were washed two times in PBS. Subsequently, cells were fixed with 4 % paraformaldehyde and 4 % sucrose for 20 min at 37°C. Following fixation, cells were washed two times in PBS for 5 min per washing step. After washing, cells were permeabilized in 0.2 % Triton X-100 (in PBS) for 5 min and subsequently blocked with 10 % fetal calf serum (FCS, in PBS) for 10 min. Primary antibodies rabbit-αHomer1b/c (1:1000, Synaptic Systems) and mouse-αBassoon (1:500, Enzo) were added to the blocking solution for 1 h at room temperature. Subsequently, cells were washed three times for 5 min each in PBS. Secondary antibodies αRabbit-Atto 594, αRabbit-Atto 647N, αMouse-Atto 594 and αMouse-Atto 647N (all 1:2000, Sigma-Aldrich; secondary antibodies were switched in different experiments, thus four instead of two secondary antibodies are given here) were incubated for 1 h at room temperature in PBS. After two following washing steps in PBS, cells were stained with DAPI (1:50.000 in PBS) for 5 min for quality control of nuclei under an epi-fluorescence microscope. Finally, cover slips were washed in deionized water and mounted in 4 μl TDE embedding medium (Appendix A.2) and sealed with nail polish. Samples were prepared by Michael Schön and Ursula Pika-Hartlaub (both Ulm University, Ulm, Germany).

Appendix B

Details on setup alignment

This section serves the purpose to give some practical guideline on how to align the described STED microscope in the lab and to point out some pitfalls along the way. It is split into three subsections with the first two dedicated to the building description starting with the front end - the part from the laser output to the single-mode fibers - and ending in the alignment of the back end - the part of the setup from the fibers to the objective and the detectors. The third subsection is dedicated to the daily alignment routine of the microscope.

Alignment describes the adjustment of optical components such that the laser beam propagates along a certain defined optical axis. This is most commonly achieved by using two iris apertures of equal height (3 inches in the case of the herein presented instrument) which serve as the reference through which the beam has to pass perfectly centered. By adjusting the optical components before the two iris apertures the beam can be centered onto both apertures assuming the components provide enough degrees of freedom. The judgment whether the beam is centered onto the iris apertures can be done by eye in the case of visible light or with the help of a small camera (see Appendix C.5.5). Bringing the beam to the center of both apertures is done by iteratively adjusting the angle and lateral position of the beam.

Such an alignment tool is very helpful but will fail for certain alignment tasks. One such task is the correct alignment of lenses in a beam expander or

the construction of a fiber collimator. The reason is that slight translational misalignment of a lens can be compensated by tilting the same lens. To help in this scenario a wavefront sensor can be used. To this end, a Shack-Hartmann sensor was purchased which provides real-time information on the wavefront aberrations of an incoming beam (SHSLab HR-130-GE STD by Optocraft GmbH). Let us exemplarily consider the alignment of a fiber collimator using this sensor. First the wavefront sensor is placed normal to the desired propagation direction of the assembled fiber collimator. This can be realized with a collimated "helper" laser beam. Next, the bare fiber is placed in front of the sensor and adjusted such that the beam is centered and normal to the sensor plane. Finally, the collimating lens is placed between the fiber and sensor at the correct distance to yield a collimated beam. The software provides real-time information on the collimation, tilt and higher optical wavefront aberrations so that this alignment task is made very easy. Needless to say the wavefront sensor is very useful when identifying the source of aberrations in the setup such as bent dichroic mirrors.

B.1 Front end alignment procedure

The first thing to plan is the general layout of the optomechanics making up the four monochromators, the dichroics and filters (see Fig. 4.3 for the schematic and Fig. B.1 for a photograph). The layout has to be chosen such that when built the fibers of channel 1 are long enough to reach from the fiber couplers to the collimators in the back end of the setup. Second, enough space for the fiber couplers should be provided such that the fiber couplers can be moved to or farther away from the laser source depending on the necessary timing alignment between the excitation and depletion beam of each channel. To this end approx. 40 cm of clearance for the fiber couplers on translation stages should be included in the planning of the layout. When the general layout is settled upon, the placement of components can start beginning with the source.

It is advantageous to leave adequate space between the source and the first mirror to be able to perform power or wavefront measurements directly after

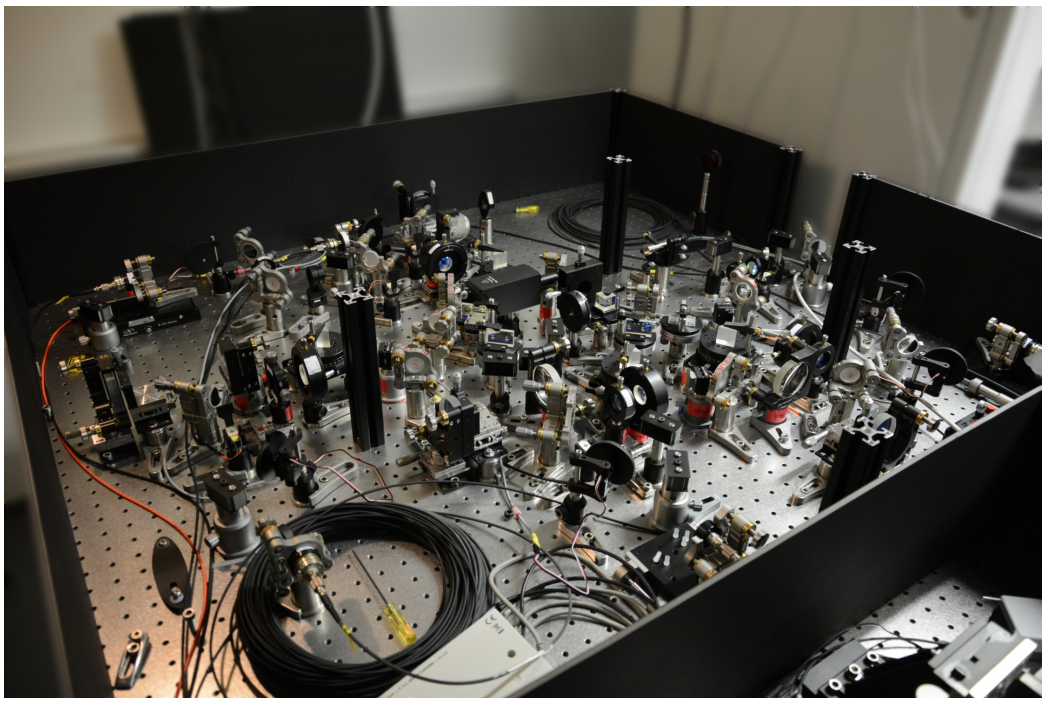

Figure B.1: Photograph of the front end built during this thesis. It occupies roughly half of the 1.2 m by 2.4 m optical table. The back end (Fig. B.3) is partly visible in the lower right corner of the photograph.

the source. The first dielectric mirror serves as a lowpass filter. Significant power in the infrared spectrum is transmitted which needs to be collected with an appropriate beam dump placed in the transmission path of the first mirror. From here on onwards, components are placed as close together as possible/allowed while still allowing practical alignment procedures.

The next optical component is the polarizing beamsplitter cube. A power measurement using a thermal power head on each arm of the beamsplitter should give a similar reading. The s-polarization of the reflected beamsplitter branch is further rotated by 90° using a $\lambda/2$ plate to maximize transmission in the prism-based monochromators further down the beam path.

Care has to be taken when building the rest of the front end setup to not back-reflect laser light into the source. For this reason an iris aperture is placed between the first mirror and the polarizing beamsplitter cube. Strong back-reflections normal to the propagation direction of the beam generally

occur at bandpass filters. These should be slightly tilted with respect to the optical axis to dump the reflected light on the aforementioned blocking iris aperture.

The alignment of the rest of the components up to the prism-based monochromators is straight forward. In the following these monochromators are explained in more detail (Fig. B.2). The beam enters a prism after which a $2f$ lens arrangement images the beam onto a mirror. A mechanical slit is placed in front of this mirror providing wavelength selection. The mirror is slightly tilted so that the reflected beam propagates towards the table on its way back through the $2f$ arrangement and the prism. Instead of exiting the monochromator the way it entered, the beam is picked off by a small mirror (height below 3 inches) and directed to a telescope. The purpose of this telescope is to optimize the coupling efficiency of the following single-mode fiber coupler. Correct alignment of the monochromator is achieved when no spectral gradient is visible across the exiting laser beam. This can be evaluated by closing the slit to only let an $\sim$ 10 nm wide band pass the monochromator. While keeping the opening aperture of the slit constant, the pass band is changed by moving the whole slit across the spectrum in front of the tilted mirror by means of a translation stage. The center of the spot should remain constant in space across the whole spectrum. This is achieved by the correct alignment of the distance from the prism to the lens to the tilted mirror ($2f$ arrangement). Note that in order to maximize the transmission through the monochromator, the light incident on the prism should be linearly p-polarized and enter at the brewster angle.

Following the monochromator, the shutter to switch the beam on or off is placed (Appendix C.2). Additionally, the servo-based intensity regulating discs are placed at the edge of the beam so as to provide no clipping of the beam when the position parameter in the intensity controller GUI is set to 255 and full blocking of the beam when set to 0 (Appendix C.3). The final element in each beam path is the fiber coupler. The incoming linearly polarized light has to be coupled into the slow axis of the fiber to maintain linear polarization at the fiber output. The slow axis (marked on the fiber ferrule) is less sensitive to bending of the fiber than the fast axis.

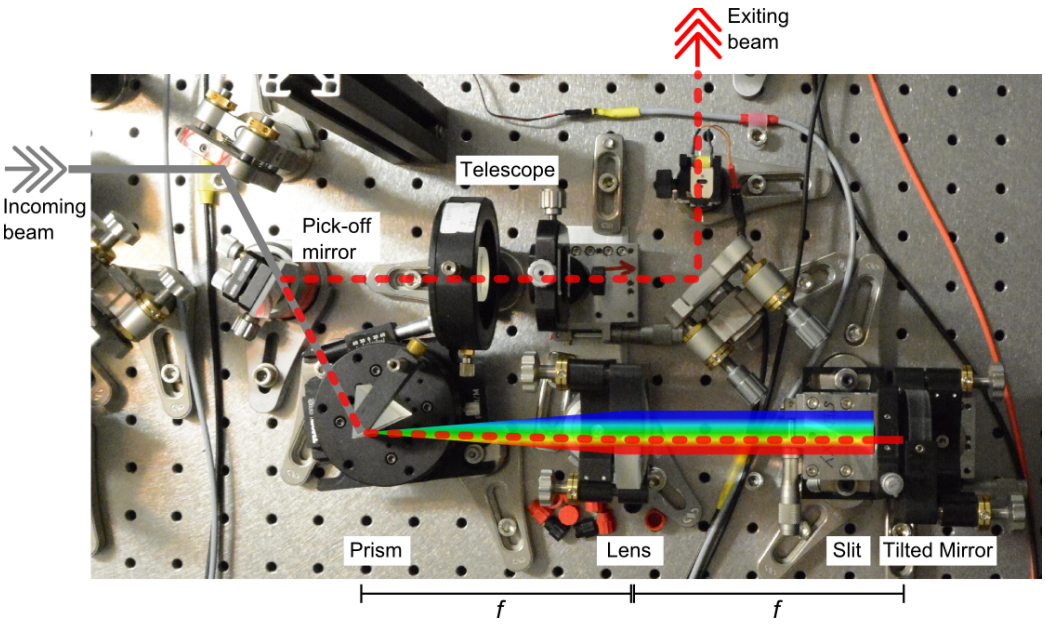

Figure B.2: Exemplary photograph of the STED-XY-2 monochromator with beam paths drawn as an overlay. The incoming beam (gray and rainbow line) is reflected on the tilted mirror and subsequently propagates towards the table surface (dotted red line). It is then picked off by a mirror and send to a telescope and finally to the fiber coupler (not shown). Wavelength selection is achieved by only letting the wanted part of the spectrum reach the tilted mirror by means of a mechanic slit placed in front of it. The lens is placed at distance f from the prism and the tilted mirror.

If the light is coupled into both the fast and slow axis the exiting light will be elliptically polarized due to the different speeds of propagation in the two axes. Correct alignment can be achieved by carefully rotating the fiber coupler in the mechanical mount and monitoring the state of polarization at the fiber output. Care has to be taken when rotating the coupler as it is very easy to completely loose the single-mode fiber coupling when the position of the coupler is altered. Should the coupling efficiency drop to zero, a helpful trick is to loosen the fiber in the coupler and slightly pull it out. This usually works well when trying to find a good starting position for maximizing the coupling efficiency in general.

B.2 Back end alignment procedure

This subsection deals with the alignment of the rest of the microscope - from the single-mode fibers to the objective and the detectors (see Fig. 4.4 for the schematic and Fig. B.3 for a photograph). As for the front end, the general layout of the back end should be well planned prior to building. The most important parameter to consider is the timing between the excitation and depletion pulses and thus the relative path lengths of each beam. Here, we start alignment from the fiber collimators. Another common way not described herein is to begin alignment with the help of a collimated alignment laser launched from the objective holder towards the fiber collimators and the detector pinholes.

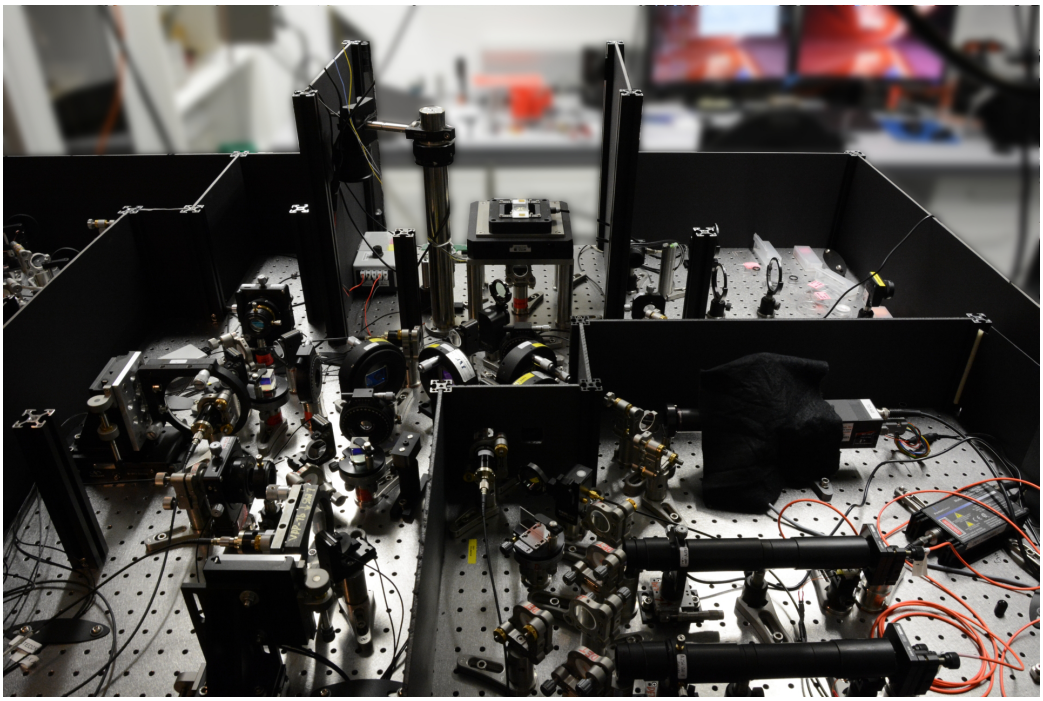

Figure B.3: Photograph of the back end built during this thesis. It occupies roughly half of the 1.2 m by 2.4 m optical table. The front end (Fig. B.1) is partly visible on the left edge of the photograph.

First, the fiber collimators are placed. The depletion beams for the axial resolution improvement are collimated by custom-built collimators consisting of a fiber holder and a lens in a 6-axis optomechanical mount. All other

beams are collimated by off-the-shelf compact collimators (Table 4.1). The reason for using homebuilt collimators is that the distance from the lens to the fiber can be more precisely controlled using the aforementioned 6-axis lens holder thus giving better control when aligning the depletion patterns in z on a gold bead. The fibers in the collimator are rotated such that the axial depletion beams are s-polarized (perpendicular to the table surface), while the remaining beams are p-polarized (parallel to the table surface). This will allow the subsequent co-alignment of the axial and lateral depletion beams for each channel using a polarizing beam splitter (PBS-2).

Subsequently, a piezo mirror is placed into the beam path which will provide nanometer alignment precision necessary for the co-alignment of all beams in the focus (Agilis AG-M100N, Newport Corporation). To provide all necessary degrees of freedom to perform beam walking (angle and position) a second manual mount is needed in each beam path. For all beams except the axial depletion beams this is the fiber collimator holder itself (in fact a manual mirror mount). Due to the homebuilt fiber collimator present in the z-depletion beam paths a second manual mirror is placed just after the lens holder. The piezo mirrors are placed closest to the objective lens (with respect to the manual positioning holder/mount).

Following the polarizing beam splitter PBS-2, the $\lambda/2$ plates are positioned. The further alignment of the dichroic mirrors is straight forward. However, attention should be paid to a precise initial alignment due to the limited size of the dichroic mirror relative to the large beams passing through them. Since the focal length of the collimator lens and the numerical aperture of the fiber used define the beam diameters of the beams they range from approx. 6.5 mm in the case of the excitation-1 beam to approx. 7.2 mm in the case of the STED-XY-1 beam to 10.6 mm for the STED-Z-2 beam. If the beams do not run centered through the dichroic mirrors one risks clipping on the edge of the mounts when having to realign with the dichroics in place.

After the fiber couplers and the polarizing beamsplitters are put into place, the achromatic $\lambda/4$ retarder and the 45° silver mirror beneath the objective holder have to be aligned. The $\lambda/4$ retarder in conjunction with the $\lambda/2$ plates are used to obtain perfect circular polarization for the beam

STED-XY-1 and STED-XY-2 entering the objective lens. Due to the way the beams STED-Z-1 and STED-Z-2 are superimposed onto the lateral depletion beams to form a single beam, the axial depletion beams will also be circular polarized with high quality. However, the excitation beams will show a small degree of elliptical polarization as the spectral region for which the $\lambda/4$ retarder is corrected for is limited from 650 nm to 900 nm (with an accuracy of a $\lambda/4$ phase shift of $\pm$ $\lambda/300$). To achieve circular polarization, proceed as follows: Put the compact polarization analyzer in place between the 45° mirror and the objective lens (section C.1). Start the respective GUI from the main application located in the "Scan" tab (Appendix C.5 and C.5.2). Switch on the analyzer to full speed and adjust the beam intensity such that the photodiode is not driven into saturation. In an iterative manner, adjust the $\lambda/2$ and $\lambda/4$ retarder of the particular beam until no residual sine modulation is visible in the graph displayed in the GUI. Switch on the other lateral depletion beam and perform the same adjustment. The optimal position of the $\lambda/4$ retarder deviates $< 1°$ for both depletion beams (dependent on the actual wavelengths used). Finally, the $\lambda/4$ retarder is set to the position between the two measured optima.

Next, the objective lens is aligned. Alignment of the high numerical aperture objective lens is not simple due to its minute focal length and high opening angle. To this end, a tube of approx. 20 cm length with an iris aperture on each end proves to be a helpful tool. The tube is screwed into the objective holder instead of the objective lens. Subsequently, each beam is iteratively adjusted to pass through both iris apertures centered as discussed in the opening section of Appendix B. Since the objective lens is susceptible to off-axis alignment, this alignment should be performed with a camera attached to the far-end of the alignment tube for more precise results. Typically, I used the STED-XY-1 beam as the reference beam to which all other beams are co-aligned to. To check the quality of alignment an iris aperture is placed before the 45° mirror and centered onto the beam (note: center the iris onto the beam, not the beam onto the iris!). Screw the objective into the holder and observe how the beam emerges from the objective when slowly closing down the iris. If alignment is correct, the beam should emerge co-

axially from the objective lens. Closing the iris aperture effectively reduces the numerical aperture of the objective lens making it easier to determine the center and angle of the emerging beam. Once the initial alignment of the objective is finished the phase plates can be inserted into the depletion beams (Table 4.3). For the STED-XY-1 beam the 708 nm pattern on the VPP-1B is used. The 735.8 nm pattern on the VPP-1A is used to imprint the 2π-phase shift pattern onto the STED-XY-2 beam. For the STED-Z-1 depletion beam the phase mask "1020 3.8" is used, while for STED-Z-2 the mask "1070 3.7" is used (the numbers correspond to the thickness and diameter of the sputtered disk). These two phase plates were empirically tested to yield the lowest residual intensity in the central minimum of the PSF from an initial set of ten phase masks.

Next, the detection path needs to be aligned. To this end, it is helpful to place a cover slip (using immersion oil) on top of the objective lens and focus to the glass-air interface. The resulting strong back-reflection is used for the alignment of the detection. Alternatively a pool of concentrated dye solution can be used as a sample to generate a beam usable for the alignment of the detection pathway by eye or camera. This approach is a little more difficult to do, as the beam is relatively dim, but it is insensitive to not-normal cover slip placement with respect to the optical axis of the objective lens. In either case the reflected/back-propagating beam needs to be co-axial to the incoming beams. This can easily be checked by using two iris apertures positioned onto the incoming beams and observing the beam exiting from the objective on the very same iris apertures.

Building the detection is straight-forward. The emission filter should be placed before the lens focusing the beam onto the multimode fiber due to the dependency of the filter's passband on the angle of incidence inherent to interference filters. The focusing lens has a focal length of 200 mm. In combination with the objective lens used the magnification of the microscope amounts to 100x. The optimal pinhole diameter which corresponds to one Airy unit ($D_{optimal}$; measured between the first zeros of the Airy function) is given by

$$D_{optimal} \approx \frac{1.22\ \lambda\ M_{Objective}}{NA} \tag{B.1}$$

where λ is the wavelength of the emission and $M_{Objective}$ is the magnification of the objective lens. $D_{optimal}$ amounts to $\sim$ 53.8 μm when using 618.5 nm as the wavelength of emission (the mean of the emission peaks of Atto 590 and Atto 647N). The detection fiber core has a diameter of 62.5 μm thus the pinhole used in this setup corresponds to approx. 1.16 Airy units. The detection fiber's relatively high numerical aperture of 0.275 calls for means of stray light rejection. To this end, a black plastic tube shields the beam from the emission filters to the detection fiber mount. The detection shutter is placed right in front of the fiber mount, leaving a little gap between the aforementioned shielding tube and the fiber mount.

The channel photomultiplier (CPM) detector used for co-alignment of the beams in the focus on a gold bead is especially sensitive to stray light. To this end a black-out cloth was draped over the lens, shutter and opening aperture of the CPM. The beam for this alternative detector path is picked-up by an electronically actuated pellicle beamsplitter between the dichroic mirrors D-4 and D-5. By using a pellicle beamsplitter the detection paths can be used to scan the sample while at the same time recording the back-scattered signal with the CPM as pointed out later in Appendix B.3.

The bright-field beam path used for a rather crude observation of the sample can now be added to the setup. First, the correct focus setting for the sample needs to be found. Subsequently, the camera is moved to/from the imaging lens until it is focused correctly. A more elaborate imaging system is in the planning stage which will allow epi-fluorescence recordings using a new scientific CMOS camera and LED-based excitation sources. This will greatly enhance the ability to efficiently find interesting regions in the sample prior to super-resolution imaging.

With the microscope fully assembled the fine-tuning of the alignment has to be performed. This is described in the following section.

B.3 Daily alignment procedure

Due to long-term drift (on the order of several hours) the microscope's alignment should be checked every day at least once. To do this, a gold bead sample in conjunction with the CPM detector is used. Pixel dwell time is set to 200 μs, scan range to 1.5 μm or 4 μm (scan plane in xy and xz, respectively) and pixel size to 10 nm or 20 nm (scan plane in xy and xz, respectively).

Before the co-alignment of the beam is tackled, the state of polarization of the lateral depletion beams needs to be optimized using the polarization analyzer (see Appendix C.1 and B.2). Subsequently, a gold bead is brought into focus and scanned in the xz plane using the STED-XY-1 reference beam. The intensity pattern should not be tilted to the left or right. If it is, it needs to be corrected by beam walking the corresponding beam with two mirrors. In each beam path one mirror is a piezo controlled mirror while the second mirror is either the fiber collimator holder itself or an actual manual mirror (only in the case of the axial depletion beams due to the home-built collimator design). In an iterative manner the mirror farther away from the objective is adjusted such that the intensity pattern tilts further. Subsequently, the intensity pattern is brought back to its initial position using the mirror closer to the objective. Depending on the distance between these two mirrors and the degree of tilt, this action needs to be performed a couple of times until the intensity pattern is perfectly parallel to the z axis. Next, the yz scan plane is scanned and adjusted accordingly. Due to small imperfections of the mirrors used, after an initial alignment of the beam in xz and then yz, the beam tilt in xz needs to be re-evaluated if the adjustments made to the mirrors were large. Any offsets between the beams in z are compensated by de/focusing the respective lens in the fiber collimator.

Next, the gold bead is scanned in xy. The depletion intensity pattern should be symmetric with a distinct minimum in the center. To correct a laterally offset minimum and asymmetries in the peak height along the rim, the phase mask needs to be translated in x or y. Subsequently, the tilt of the PSF needs to be re-checked using the aforementioned approach. Finally,

all other beams are adjusted so that their position co-coincides with the reference beam and any tilt is corrected. This includes the detection beam paths. To this end, the fiber from the Exc-1 fiber coupler is unplugged and the bandpass filter in front of it removed. A multimode fiber of the same type as the detection fiber is inserted and attached to the particular detection fiber by the means of an inline fiber coupler. Subsequently, the detection beam is scanned across the gold bead. The alignment follows the routine described above.

The microscope is now ready for imaging. While the setup will drift more after the days of building, the drift overnight decreases with time. Thus, alignment in tilt and position of the beams are generally small (on the order of 10's of nanometers overnight).

Appendix C

Instrumentation and software

A short overview of some of the major hardware components as well as the software written as part of this thesis is given in this section.

C.1 Compact polarization analyzer

The state of polarization is very important for the correct functioning of the setup. In order to measure the quality of circular polarization a compact polarization analyzer was built (Fig. C.1). It consists of a rotating polarizer and a photo diode with the necessary electronics and a battery. To quickly check the state of polarization right before the objective lens this analyzer was designed so that it slides in between the 45° mirror and the objective lens (Appendix B.2). This feature avoids having to take out the objective for polarization measurements. Needless to say, the analyzer can be positioned in between any components throughout the setup. A graphical user interface (GUI) was written in LabView which gives the user real-time information on the quality of circular polarization. The GUI can be run standalone or run as part of the main program suite used to provide computer control of the microscope (Appendix C.5).

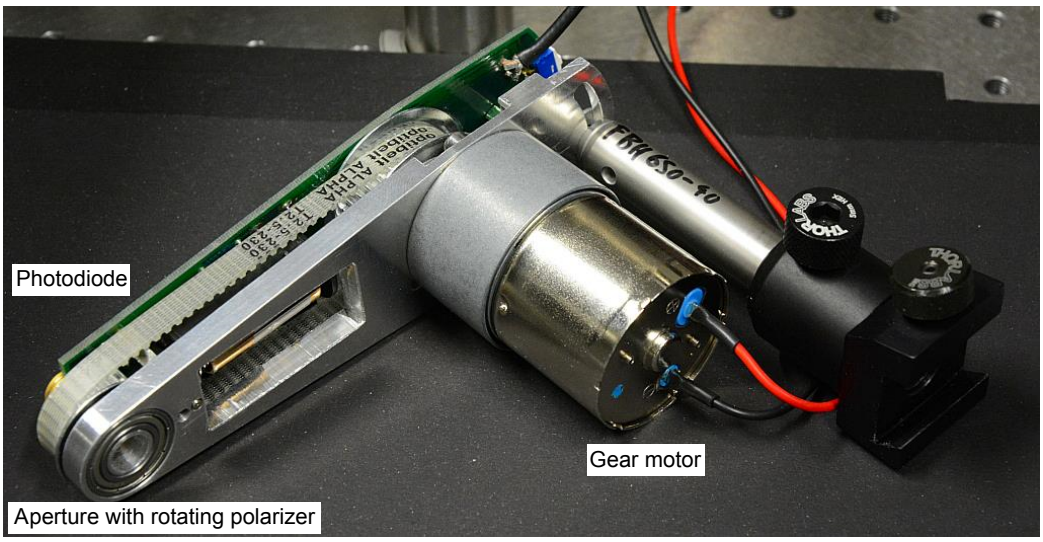

Figure C.1: Photograph of the compact polarization analyzer used to check for circular polarization of the depletion beams entering the objective. Due to its thin design it fits in between the 45° mirror and the objective lens defeating the need to unmount the objective lens for polarization measurements. The gear motor drives the ball bearing aperture with the polarizer through a belt. The photodiode is located above the aperture. The electronics are sandwiched onto the main frame to maintain the thin design.

C.2 Shutter controller

To switch beams on or off remotely from a computer a shutter controller was built. It consists of a microcontroller Z8encore Z8F6422 which controls the h-bridge drivers L298. It is interfaced through digital inputs for each of the eight shutter channels and a GUI was written to provide remote computer control of the shutters. To keep the thermal load in the microscope assembly as low as possible bistable shutters were chosen (04RDS501, CVI Melles Griot). The device was built by Bernhard Gruchmann (Uni Ulm, Germany).

C.3 Intensity controller

In order to be able to control the intensity of each beam individually an intensity controller was built. It controls eight servos which have a disc attached that acts as a blocking edge. The disc's shape resembles a spiral so

that the full rotation of the servo can be translated into a change in intensity. The servo devices are placed in front of each fiber coupler. Due to the nature of the single-mode fiber, a partially blocked beam will only exhibit a reduction in intensity while its shape is still Gaussian at the fiber output. The controller is based around a Z8encore Z8F6422 microcontroller which provides a RS-232 interface and allows 8-bit control of the servo's position. While this seems low for a modern microcontroller the analog servo's achievable resolution actually sets this limit (ESU 51804, www.onlinehobbyshop.de). The device was built by Bernhard Gruchmann (Ulm University, Ulm, Germany). A GUI was written to comfortably control the servo position with a computer. The program allows the user to store presets which is convenient when switching between tasks such as gold bead scanning and STED imaging.

C.4 Time gating device

As pointed out in section 4.2.3, a synchronized detection scheme is necessary to successfully discriminate between the signal of the two channels. To this end a time gating device was built which rejects detector pulses when outside a user-specified time window. In a first prototype the adjustment of the time windows was done by means of analog potentiometers. The current version is based on a Z8encore Z8F6421 microcontroller controlling digital potentiometers. This allows for a remote interface via RS-232. A GUI was written in LabView which provides convenient access to the controller parameters. The parameters set the delay of each time gate after an input pulse from the laser source and the time gate duration. The device runs very stable thus setting the correct parameters is a set-and-forget task.

The connections to the device are described in the following. The laser source pulse output is connected to the "Laser Pulse Input" jack. The "Laser Pulse Monitor Out" provides a buffered output to visualize the laser sync pulse using an oscilloscope. The "Detector Input" is connected to the output of the DSN 101 detector power supply (Picoquant) which provides the raw counts of the detector. The "Detector Monitor Out" allows the user to monitor the raw detector events while the device is working. The output

"Gate & Det Output" carries the detector pulses which occurred during the time gate and is fed to the counter on the data acquisition card. The "Gate Monitor Out" connector allows the user to monitor the user-defined time gate.

To set the correct time gate a concentrated dye solution is used as a sample. A fast oscilloscope is used to monitor the time gate and the arrival of the detector pulses. To this end, the "Gate Monitor Out" output is connected to the oscilloscope and used as the waveform trigger. The "Detector Monitor Out" connector is plugged in to the second oscilloscope channel. The excitation intensity is chosen relatively high so that for every laser pulse a detector event can be seen. The time gate is then positioned so that it encloses the detector events which give a stable trace. This process is then repeated for the remaining channel. Please refer to the sample recordings in Fig. 4.7 and 4.8 to see a correctly set-up time gate. The device was built by Bernhard Gruchmann (Uni Ulm, Germany).

C.5 Microscope control software

All software which is involved in providing control of the microscope was written in LabView. In this section I will give a short overview of the main concepts used in programming the application so that future users are able to quickly add their own code.

C.5.1 Programming approach

The whole application is implemented as an event-driven state machine. Each particular function of the program such as loading an image file, performing a scan or initializing the coarse stage is represented as an individual state. Depending on user action e.g. pressing the button labeled "Scan", the program executes the particular state associated with the button. This approach allows a relatively clean layout. It also allows to programmatically string together states which should occur in a particular order. An example is the activation of the "Save Scan" radio button. When it is activated and the user

presses “Scan”, the application scans an image (state: scan) and then instead of returning to the wait-state (to wait for further user input) it executes the state “save image as .tiff and associated data as .xml”. After successful completion the program resides in the wait-state. This programming approach is used throughout the program and allows for the fast implementation of new features; simply add a new state and an action which will trigger that state to be executed. Since the whole program is event-driven no resources are lost due to constant polling for user input.

In the application, several sub-programs have to run in parallel at all times to provide real-time control even when in a time-consuming state (such as scanning an image). This includes the shutter controller GUI, the camera GUI, the coarse positioning stage GUI, the intensity controller GUI, the piezo mirror control GUI and also the polarization analyzer GUI. These programs run as separate processes and can be started from within the main application. These parallel processes exchange data with the main application instance through the use of queues. All references to the queues are obtained in the initialize-state which is always the first state executed upon the start of the program. The image data and all associated parameters are passed throughout the program as a cluster labeled “Master Data Cluster”. The cluster is further divided into clusters associated with specific data such as “Shutter Controller Parameters” and “Scanning Stage Parameters”. This keeps all relevant data neatly ordered in one place while sub-programs can access the parameters through the use of a single queue.

C.5.2 Main application tabs

The main application is made up of 11 tabs which provide access to particular functions of the application.

Scan tab: The Scan tab is the most important tab in the software. From here, images can be scanned and are displayed when acquired. Additionally, previously acquired images can be loaded and displayed. Furthermore, parallel running GUI instances can be started from within this tab.

Scan Parameters tab: This tab opens the view on all parameters which

are processed and used to set up the scan when the scan button is pressed. All those parameters are saved along with the image (a .tiff file) as a separate .xml file. The most important and most often adjusted parameters are the pixel dwell time, which beams are to be active during the scan and whether only one or more images are to be acquired. Additionally, transition parameters can be set. These parameters determine which action the scanning stage takes after the acquisition of an image. The default mode is "No Transition" meaning that no action is taken. In the case of "Image Stack" the parameters determine which axis to increment how many times by a set amount after an image was scanned. This allows the convenient scanning of z image stacks for three-dimensional reconstruction but is not limited to incrementing the z-axis. In the mode "Drift Measurement" the beams previously selected in the "Shutter Controller Parameters" are individually scanned one after each other for a user-set number of cycles. Additionally, a delay can be introduced in between individual images or cycles.

Main Data Cluster tab: This tab lists all parameters used to record the currently displayed image.

Cursor Statistic tab: This tab is very useful for assessing the quality of the residual intensity in the minimum of the depletion beams. Three modifiable boxes (labeled "Minimum", "Maximum" and "Background") appear on the displayed image which can be dragged onto the respective regions of the intensity pattern. The program then displays the calculated minimum intensity in the center of the PSF in percent of the maximum and corrected for background. As a rule of thumb, the minimum of the PSF should be on the order of 1 %. Additionally, the image look-up-table can be modified on the fly to better visualize interesting regions of the image by stretching the contrast.

Line Plot tab: This view allows the user to extract a line plot from an arbitrary straight line of the image. It is helpful to obtain a first measure of resolution from fluorescence images when dragged over small features in the image.

Cross-correlation tab: This tab allows the user to calculate the cross-correlation between image channel 1 and channel 2 and indicates the maxi-

mum of the correlation function.

Line Shift tab: This tab allows the user to shift every other line of an image by a set amount of pixels. It was necessary for correcting line shift while using an old piezo scanning stage in the first version of the microscope. Since an improved scanning stage is used in the current version, this feature is outdated.

Read Stage Values tab: The scanning stage is able to record its positional data during a scan. The tab gives the user access to this data to check scan integrity or oscillating stage problems. Which data (recording rate, positional error or actual position) is to be recorded is specified by the user in the aforementioned "Scan Parameters" tab.

Controller Commands tab: This tab provides controls to initialize the coarse positioning stage and reboot the stage controllers after failure. It also provides access to set scanning stage hardware parameters such as the proportional-integral-derivative (PID) controller parameters. This allows optimization of the scanning behavior should the stage have been altered significantly (such as added weight).

Waveform Editor tab: In this tab the user can upload preset scans to the scanning stage controller.

Debug tab: This tab displays error codes in case of a problem.

C.5.3 Stage scanning and software synchronization

In a scanning laser microscope, tight synchronization between the stage/beam scanner and the recording software is needed in order to assign detector counts to the correct pixel. Arguably, the best approach is to synchronize each pixel instead of just once per start of a new line or even image. The scanning stage controller used (E-712, Physik Instrumente) features a digital output which sends a pulse whenever the position of the stage is updated. This update rate is fixed at 50 kHz for the three channel controller thus a pulse every 20 μs is recorded at the controller output just mentioned. The actual pixel dwell time is set by the Wave Table Rate (WTR) parameter and is an integer multiple of the mentioned update rate (termed Servo Update

Rate). Synchronization is obtained by keeping track of the servo update pulse put out by the controller in the recording software. To give a practical example, let's assume a pixel dwell time of 200 μs set by a WTR of 10. For every pixel, 10 pulses are expected to be emitted at the controller servo update output. Counting these pulses allows the software to determine the current location of the scanning stage which in turn allows a tight synchronization scheme per pixel. Unfortunately, the data acquisition card used (PCIe-6259, National Instruments) only features two counters which are used for counting the detector pulses. Thus, a different route to count the servo update pulses is needed. To this end, an analog-in dummy task is created in LabView and configured such that the controller's servo update pulse is used as its timebase source (parameter SampClk.Timebase.Src). The dummy task serves the sole purpose of generating a timebase for the detector counters (no voltage is recorded). The WTR parameter is fed to the parameter SampClk.TimebaseDiv. in the dummy task. Following, the dummy task is configured such that it starts working when a digital trigger is received from the stage controller (a second output on the controller can be configured to give this "start synchronization pulse"). Thus, when the stage starts a new scan, the start time point is synchronized with the recording software. To achieve the per-pixel synchronization scheme for the whole scan, the dummy task's timebase (given by the controller servo update pulse explained above) is now used as a trigger to read the detector counters. Thus, the detector counters are tightly synchronized with the current position of the stage on a per-pixel basis for the whole scan. This synchronization scheme, albeit somewhat complex, removes the necessity of a third counter on the data acquisition card.

C.5.4 A sample session

Following the start of the main application the user needs to manually initialize the coarse stage in the "controller commands" tab. Subsequently, the user can load preset scan parameters into the scanning stage controller if the controller was power cycled (it looses all wave-tables upon reset). Loading

the presets into the controller takes a little time which is why I resorted to using presets in the first place. Defining scans on the fly takes time as the wave-table (which determines the scan dimension/resolution) has to be loaded into the controller prior to each individual scan.

When the preset upload is finished the user can close the pop-up dialog. Note that the user only has to upload the presets if the scanning stage controller was reset. The parallel running GUIs are started by pressing the appropriate buttons in the "Scan" tab.

In order to take an image one now sets the pixel dwell time, the scan type (single or continuous) and the beams to be active in the "Scan Parameters" tab. Subsequently, the user now decides which detector is active (CPM or APDs), whether the scan is to be saved and the preset determining the scan area and pixel size in the "Scan" tab. Furthermore, the user is encouraged to give a meaningful name to the image. Finally, the user needs to specify around which coordinates (x, y and z) the scan is to be centered. The maximal scan dimensions are set by the scanning stage and the z-objective piezo stage to 30 μm x 30 μm x 12 μm in x, y and z, respectively. The center positions are either entered numerically by the user in units of μm or taken from the cursor on the image (if the radio button "Use Cursor" is active). After pressing the "Scan" button the scan starts and the data is displayed in a pop-up window while it is being acquired. The user has the option to stop the scan when finished (in case the scan type "continuous" was set) or abort it immediately only saving the data recorded up to that point. After scanning, the acquired image is displayed in the "Scan" tab and a link to the file is added to the list "Images in current directory". Note that the image is stored in a folder named after the current date which is automatically created if it does not exist already.

C.5.5 Additional software

Camera GUI: To help with the alignment of the setup a camera application was developed. The GUI displays the image and finds the center of a Gaussian beam by least-squares fitting. This comes to use when aligning the

objective with the aforementioned alignment tube or in any case in which the beam to be aligned is too dim for the human eye to see (Appendix B.2).

Image browser application: In order to comfortably browse through recorded images when not located at the microscope a stripped down version of the main application (Appendix C.5) was created. It offers similar functionality with the exception of scanning. Therefore no hardware drivers for the controllers and the additional hardware are necessary.

Spectr-o-mat application: In order to check the usability of filters a standalone application was developed which allows the user to import spectral data of filter or dyes. Various operations can be applied to the loaded spectra. This software was used to calculate the transmission of the beam paths presented in Fig. 4.6.

Abbreviations

APD	Avalanche photo diode
AU	Airy unit
BP	Bandpass filter
BSA	bovine serum albumine
C2C12	Mouse myoblast cell line
CPM	Channel photomultiplier
CPP	Circular phase plate
CsA	Cyclosporine A
CW	Continuous wave
Cyp	Cyclophilin
D	Dichroic mirror
DABCO	1,4-Diazabicyclo[2.2.2]octan
DAPI	4',6-Diamidino-2-phenylindole
EdU	5-Ethynyl-2'-deoxyuridine
EEA1	Early endosome antigen 1
EF	Emission filter
Exc	Excitation
FG-repeat	phenylalanine-glycine repeat
FWHM	Full-width-at-half-maximum
FWQM	Full-width-at-quarter-maximum
GFP	Green fluorescent protein
GSD	Ground state depletion
GUI	Graphical user interface
HeLa	Henrietta Lacks
LSM	Laser scanning microscope

MDCK	Madin Darby canine kidney
MMF	Multi-mode fiber
NA	Numerical aperture
NPC	Nuclear pore complex
Nup	Nucleoporin
PALM	Photoactivated localization microscopy
PBS	Polarizing beam splitter (optics) or phosphate buffered saline (chemicals)
PCNA	proliferating cell nuclear antigen
PID	Proportional-integral-derivative
PSD	Postsynaptic density
PSF	Point spread function
PVA	Polyvinylalcohol
ROXS	Reducing and oxidizing system
SIM	Structured illumination microscope
SMF	Single-mode fiber
SNR	Signal-to-noise ratio
SPEM	Saturated patterned excitation microscopy
SSIM	Saturated structured illumination microscopy
STED	Stimulated emission depletion
STORM	Stochastic optical reconstruction microscopy
T-STED	Time-gated stimulated emission depletion
TDE	2,2'-Thiodiethanol
Tpr	Translocated promoter region
Tris-HCL	2-Amino-2-(hydroxymethyl)-1,3-propanediol hydrochloride
U2OS	Human bone osteosarcoma
VPP	Vortex phase plate
WTR	Wavetable rate

List of Figures

List of Tables

List of Publications

Publications in peer reviewed journals

Jeffrey R. Moffitt, Christian Osseforth, and Jens Michaelis. Time-gating improves the spatial resolution of STED microscopy. *Optics Express*, 19:4242, 2011

Adriano A. Torrano, Julia Blechinger, Christian Osseforth, Christian Argyo, Armin Reller, Thomas Bein, Jens Michaelis, and Christoph Bräuchle. A fast analysis method to quantify nanoparticle uptake on a single cell level. *Nanomedicine*, 8:1815, 2013

Christian Osseforth, Jeffrey R. Moffitt, Lothar Schermelleh, and Jens Michaelis. Simultaneous dual-color 3D STED microscopy. *Optics Express*, 22(6):7039, 2014

Katharina Ernst, Simon Langer, Christian Osseforth, Jens Michaelis, Michel R. Popoff, Carsten Schwan, Klaus Aktories, Viktoria Kahlert, Miroslav Malesevic, Cordelia Schiene-Fischer, and Holger Barth. Cyclophilin-facilitated membrane translocation as pharmacological target to prevent intoxication of mammalian cells by binary clostridial actin ADP-ribosylated toxins. *Journal of Molecular Biology* 2014

Invited paper

Christian Osseforth, Jeffrey R. Moffitt, and Jens Michaelis. Time-gated STED microscopy. *G.I.T. Imaging & Microscopy*, 4:34, 2011

Bibliography

G. B. Airy. On the diffraction of an object-glass with circular aperture. *Transactions of the Cambridge Philosophical Society*, 5:283–291, 1835.

Frank Alber, Svetlana Dokudovskaya, Liesbeth M. Veenhoff, Wenzhu Zhang, Julia Kipper, Damien Devos, Adisetyantari Suprapto, Orit Karni-Schmidt, Rosemary Williams, Brian T. Chait, Andrej Sali, and Michael P. Rout. The molecular architecture of the nuclear pore complex. *Nature*, 450(7170): 695–701, 2007. ISSN 1476-4687. doi: 10.1038/nature06405.

W. B. Amos and J. G. White. How the Confocal Laser Scanning Microscope entered Biological Research. *Biology of the Cell*, 95(6):335–342, 2003. ISSN 02484900. doi: 10.1016/S0248-4900(03)00078-9.

Per Ola Andersson, Christian Lejon, Barbro Ekstrand-Hammarström, Christine Akfur, Linnéa Ahlinder, Anders Bucht, and Lars Osterlund. Polymorph- and size-dependent uptake and toxicity of TiO_2 nanoparticles in living lung epithelial cells. *Small*, 7(4):514–523, 2011. ISSN 1613-6829. doi: 10.1002/smll.201001832.

Silvia Arroyo-Camejo, Marie-Pierre Adam, Mondher Besbes, Jean-Paul Hugonin, Vincent Jacques, Jean-Jacques Greffet, Jean-François Roch, Stefan W. Hell, and François Treussart. Stimulated emission depletion microscopy resolves individual nitrogen vacancy centers in diamond nanocrystals. *ACS Nano*, 7(12):10912–10919, 2013. ISSN 1936-086X. doi: 10.1021/nn404421b.

D. Baddeley, V. O. Chagin, L. Schermelleh, S. Martin, A. Pombo, P. M.

Carlton, A. Gahl, P. Domaing, U. Birk, H. Leonhardt, C. Cremer, and M. C. Cardoso. Measurement of replication structures at the nanometer scale using super-resolution light microscopy. *Nucleic Acids Research*, 38 (2):e8, 2010. ISSN 1362-4962. doi: 10.1093/nar/gkp901.

H. Barth, D. Blocker, J. Behlke, W. Bergsma-Schutter, A. Brisson, R. Benz, and K. Aktories. Cellular uptake of Clostridium botulinum C2 toxin requires oligomerization and acidification. *The Journal of Biological Chemistry*, 275(25):18704–18711, 2000. ISSN 0021-9258. doi: 10.1074/jbc.M000596200.

Holger Barth, Klaus Aktories, Michel R. Popoff, and Bradley G. Stiles. Binary bacterial toxins: biochemistry, biology, and applications of common Clostridium and Bacillus proteins. *Microbiology and Molecular Biology Reviews : MMBR*, 68(3):373–402, table of contents, 2004. ISSN 1092-2172. doi: 10.1128/MMBR.68.3.373-402.2004.

J. E. Berlier, A. Rothe, G. Buller, J. Bradford, D. R. Gray, B. J. Filanoski, W. G. Telford, S. Yue, J. Liu, C.-Y. Cheung, W. Chang, J. D. Hirsch, Beechem Rosaria P. Haugland, J. M., and R. P. Haugland. Quantitative Comparison of Long-wavelength Alexa Fluor Dyes to Cy Dyes: Fluorescence of the Dyes and Their Bioconjugates. *Journal of Histochemistry & Cytochemistry*, 51(12):1699–1712, 2003. ISSN 0022-1554. doi: 10.1177/002215540305101214.

Eric Betzig, George H. Patterson, Rachid Sougrat, O. Wolf Lindwasser, Scott Olenych, Juan S. Bonifacino, Michael W. Davidson, Jennifer Lippincott-Schwartz, and Harald F. Hess. Imaging intracellular fluorescent proteins at nanometer resolution. *Science (New York, N.Y.)*, 313(5793):1642–1645, 2006. ISSN 1095-9203. doi: 10.1126/science.1127344.

Pit Bingen, Matthias Reuss, Johann Engelhardt, and Stefan W. Hell. Parallelized STED fluorescence nanoscopy. *Optics Express*, 19(24):23716–23726, 2011. ISSN 1094-4087.

Julia Blechinger, Alexander T. Bauer, Adriano A. Torrano, Christian Gorzelanny, Christoph Bräuchle, and Stefan W. Schneider. Uptake kinetics and nanotoxicity of silica nanoparticles are cell type dependent. *Small*, 9(23): 3970–80, 3906, 2013. ISSN 1613-6829. doi: 10.1002/smll.201301004.

Max Born and Emil Wolf. *Principles of optics: Electromagnetic theory of propagation, interference and diffraction of light*. Cambridge University Press, Cambridge and New York, 7th expanded ed. edition, 1999. ISBN 9780521639217.

Christina Brandenberger, Christian Mühlfeld, Zulqurnain Ali, Anke-Gabriele Lenz, Otmar Schmid, Wolfgang J. Parak, Peter Gehr, and Barbara Rothen-Rutishauser. Quantitative evaluation of cellular uptake and trafficking of plain and polyethylene glycol-coated gold nanoparticles. *Small*, 6(15): 1669–1678, 2010. ISSN 1613-6829. doi: 10.1002/smll.201000528.

Johanna Bückers, Dominik Wildanger, Giuseppe Vicidomini, Lars Kastrup, and Stefan W. Hell. Simultaneous multi-lifetime multi-color STED imaging for colocalization analyses. *Optics Express*, 19(4):3130–3143, 2011. ISSN 1094-4087.

Andriy Chmyrov, Jan Keller, Tim Grotjohann, Michael Ratz, Elisa d'Este, Stefan Jakobs, Christian Eggeling, and Stefan W. Hell. Nanoscopy with more than 100,000 'doughnuts'. *Nature Methods*, 10(8):737–740, 2013. ISSN 1548-7091. doi: 10.1038/nmeth.2556.

A. H. Coons. Studies on antibody production: I. A method for the histochemical demonstration of specific antibody and its application to a study of the hyperimmune Rabbit. *Journal of Experimental Medicine*, 102(1): 49–60, 1955. ISSN 0022-1007. doi: 10.1084/jem.102.1.49.

Thorben Cordes, Jan Vogelsang, and Philip Tinnefeld. On the mechanism of Trolox as antiblinking and antibleaching reagent. *Journal of the American Chemical Society*, 131(14):5018–5019, 2009. ISSN 1520-5126. doi: 10.1021/ja809117z.

Zoltan Cseresnyes, Ulf Schwarz, and Catherine M. Green. Analysis of replication factories in human cells by super-resolution light microscopy. *BMC Cell Biology*, 10:88, 2009. ISSN 1471-2121. doi: 10.1186/1471-2121-10-88.

Adish Dani, Bo Huang, Joseph Bergan, Catherine Dulac, and Xiaowei Zhuang. Superresolution imaging of chemical synapses in the brain. *Neuron*, 68(5):843–856, 2010. ISSN 1097-4199. doi: 10.1016/j.neuron.2010.11.021.

den Dekker, A. J. and van den Bos, A. Resolution: a survey. *Journal of the Optical Society of America A*, 14(3):547, 1997. ISSN 1084-7529. doi: 10.1364/JOSAA.14.000547.

Winfried Denk, David W. Piston, Watt W. Webb. Multi-Photon Molecular Excitation in Laser-Scanning Microscopy. In James B. Pawley, editor, *Handbook of Biological Confocal Microscopy*, pages 535–549. Springer US, 2006.

Hendrik Deschout, Francesca Cella Zanacchi, Michael Mlodzianoski, Alberto Diaspro, Joerg Bewersdorf, Samuel T. Hess, and Kevin Braeckmans. Precisely and accurately localizing single emitters in fluorescence microscopy. *Nature Methods*, 11(3):253–266, 2014. ISSN 1548-7091. doi: 10.1038/nmeth.2843.

Nicholas E. Dickenson, Kevin P. Armendariz, Heath A. Huckabay, Philip W. Livanec, and Robert C. Dunn. Near-field scanning optical microscopy: a tool for nanometric exploration of biological membranes. *Analytical and Bioanalytical Chemistry*, 396(1):31–43, 2010. ISSN 1618-2650. doi: 10.1007/s00216-009-3040-1.

Gerald Donnert, Jan Keller, Rebecca Medda, M. Alexandra Andrei, Silvio O. Rizzoli, Reinhard Lührmann, Reinhard Jahn, Christian Eggeling, and Stefan W. Hell. Macromolecular-scale resolution in biological fluorescence microscopy. *Proceedings of the National Academy of Sciences of the United States of America*, 103(31):11440–11445, 2006. ISSN 1091-6490. doi: 10.1073/pnas.0604965103.

Marcus Dyba and Stefan Hell. Focal Spots of Size $\lambda/23$ Open Up Far-Field Florescence Microscopy at 33 nm Axial Resolution. *Physical Review Letters*, 88(16), 2002. ISSN 0031-9007. doi: 10.1103/PhysRevLett.88.163901.

Marcus Dyba and Stefan W. Hell. Photostability of a Fluorescent Marker Under Pulsed Excited-State Depletion through Stimulated Emission. *Applied Optics*, 42(25):5123, 2003. ISSN 0003-6935. doi: 10.1364/AO.42.005123.

M. Eckhardt, H. Barth, D. Blöcker, and K. Aktories. Binding of Clostridium botulinum C2 toxin to asparagine-linked complex and hybrid carbohydrates. *The Journal of Biological Chemistry*, 275(4):2328–2334, 2000. ISSN 0021-9258.

Andreas Elsaesser, Ashley Taylor, de Yanés, Gesa Staats, George McKerr, Eun-Mee Kim, Eugene O'Hare, and C. Vyvyan Howard. Quantification of nanoparticle uptake by cells using microscopical and analytical techniques. *Nanomedicine (London, England)*, 5(9):1447–1457, 2010. ISSN 1748-6963. doi: 10.2217/nnm.10.118.

Katharina Ernst, Simon Langer, Eva Kaiser, Christian Osseforth, Jens Michaelis, Michel R. Popoff, Carsten Schwan, Klaus Aktories, Viktoria Kahlert, Miroslav Malesevic, Cordelia Schiene-Fischer, and Holger Barth. Cyclophilin-Facilitated Membrane Translocation as Pharmacological Target to Prevent Intoxication of Mammalian Cells by Binary Clostridial Actin ADP-Ribosylated Toxins. *Journal of Molecular Biology*, 2014. ISSN 1089-8638. doi: 10.1016/j.jmb.2014.07.013.

Ernst Abbe. *Beiträge zur Theorie des Mikroskops und der mikroskopischen Wahrnehmung*. Johann Wolfgang Goethe-Universität Frankfurt am Main and keine Angabe Fachbereich. keine Angabe Institut, 1873.

F. Görlitz, P. Hoyer, H. Falk, L. Kastrup, J. Engelhardt, and S. W. Hell. A STED Microscope designed for routine biomedical applications. *Progress in Electromagnetics Research*, 147:57–68, 2014.

Lisa Foa and Robert Gasperini. Developmental roles for Homer: more than just a pretty scaffold. *Journal of Neurochemistry*, 108(1):1–10, 2009. ISSN 1471-4159. doi: 10.1111/j.1471-4159.2008.05726.x.

Silvia Galiani, Benjamin Harke, Giuseppe Vicidomini, Gabriele Lignani, Fabio Benfenati, Alberto Diaspro, and Paolo Bianchini. Strategies to maximize the performance of a STED microscope. *Optics Express*, 20 (7):7362–7374, 2012. ISSN 1094-4087.

H. Gest. The discovery of microorganisms by Robert Hooke and Antoni van Leeuwenhoek, Fellows of The Royal Society. *Notes and Records of the Royal Society*, 58(2):187–201, 2004. ISSN 0035-9149. doi: 10.1098/rsnr.2004.0055.

Fabian Göttfert, Christian A. Wurm, Veronika Mueller, Sebastian Berning, Volker C. Cordes, Alf Honigmann, and Stefan W. Hell. Coaligned Dual-Channel STED Nanoscopy and Molecular Diffusion Analysis at 20 nm Resolution. *Biophysical Journal*, 105(1):L01–3, 2013. ISSN 0006-3495. doi: 10.1016/j.bpj.2013.05.029.

Tim Grotjohann, Ilaria Testa, Matthias Reuss, Tanja Brakemann, Christian Eggeling, Stefan W. Hell, and Stefan Jakobs. rsEGFP2 enables fast RESOLFT nanoscopy of living cells. *eLife*, 1:e00248, 2012. ISSN 2050-084X. doi: 10.7554/eLife.00248.

David Grünwald and Robert H. Singer. Multiscale dynamics in nucleocytoplasmic transport. *Current Opinion in Cell Biology*, 24(1):100–106, 2012. ISSN 0955-0674. doi: 10.1016/j.ceb.2011.11.011.

Gustafsson, Mats G L. Nonlinear structured-illumination microscopy: wide-field fluorescence imaging with theoretically unlimited resolution. *Proceedings of the National Academy of Sciences of the United States of America*, 102(37):13081–13086, 2005. ISSN 1091-6490. doi: 10.1073/pnas.0406877102.

Kyu Young Han, Katrin I. Willig, Eva Rittweger, Fedor Jelezko, Christian Eggeling, and Stefan W. Hell. Three-dimensional stimulated emission depletion microscopy of nitrogen-vacancy centers in diamond using continuous-wave light. *Nano Letters*, 9(9):3323–3329, 2009. ISSN 1530-6992. doi: 10.1021/nl901597v.

Benjamin Harke, Jan Keller, Chaitanya K. Ullal, Volker Westphal, Andreas Schönle, and Stefan W. Hell. Resolution scaling in STED microscopy. *Optics Express*, 16(6):4154, 2008. ISSN 1094-4087. doi: 10.1364/OE.16.004154.

Kristen M. Harris and Richard J. Weinberg. Ultrastructure of synapses in the mammalian brain. *Cold Spring Harbor Perspectives in Biology*, 4(5), 2012. ISSN 1943-0264. doi: 10.1101/cshperspect.a005587.

Gerd Haug, Jost Leemhuis, Dirk Tiemann, Dieter K. Meyer, Klaus Aktories, and Holger Barth. The host cell chaperone Hsp90 is essential for translocation of the binary Clostridium botulinum C2 toxin into the cytosol. *The Journal of Biological Chemistry*, 278(34):32266–32274, 2003. ISSN 0021-9258. doi: 10.1074/jbc.M303980200.

Eugene Hecht. *Optics*. Addison-Wesley, Reading, Mass., 4th ed. edition, 2002. ISBN 9780321188786.

Rainer Heintzmann, Thomas M. Jovin, and Christoph Cremer. Saturated patterned excitation microscopy—a concept for optical resolution improvement. *Journal of the Optical Society of America A*, 19(8):1599, 2002. ISSN 1084-7529. doi: 10.1364/JOSAA.19.001599.

S. Hell and H. K. Stelzer. Fundamental improvement of resolution with a 4Pi-confocal fluorescence microscope using two-photon excitation. *Optics Communications*, 93:277–282, 1992. ISSN 00304018.

S. W. Hell and M. Kroug. Ground-state-depletion fluorscence microscopy: A concept for breaking the diffraction resolution limit. *Applied Physics B Lasers and Optics*, 60(5):495–497, 1995. ISSN 0946-2171. doi: 10.1007/BF01081333.

S. W. Hell and J. Wichmann. Breaking the diffraction resolution limit by stimulated emission: stimulated-emission-depletion fluorescence microscopy. *Optics Letters*, 19(11):780–782, 1994. ISSN 0146-9592.

S. W. Hell, K. I. Willig, M. Dyba, S. Jakobs, L. Kastrup, V. Westphal. Nanoscale Resolution with Focused Light: Stimulated Emission Depletion and Other Reversible Saturable Optical Fluorescence Transitions Microscopy Concepts. In James B. Pawley, editor, *Handbook of Biological Confocal Microscopy*, pages 571–579. Springer US, 2006.

Stefan W. Hell. Far-field optical nanoscopy. *Science (New York, N.Y.)*, 316 (5828):1153–1158, 2007. ISSN 1095-9203. doi: 10.1126/science.1137395.

Stefan W. Hell. Microscopy and its focal switch. *Nature Methods*, 6(1):24–32, 2009. ISSN 1548-7091. doi: 10.1038/nmeth.1291.

Stefan W. Hell, Roman Schmidt, and Alexander Egner. Diffraction-unlimited three-dimensional optical nanoscopy with opposing lenses. *Nature Photonics*, 3(7):381–387, 2009. ISSN 1749-4885. doi: 10.1038/nphoton.2009.112.

Iddo Heller, Gerrit Sitters, Onno D. Broekmans, Géraldine Farge, Carolin Menges, Wolfgang Wende, Stefan W. Hell, Peterman, Erwin J G, and Wuite, Gijs J L. STED nanoscopy combined with optical tweezers reveals protein dynamics on densely covered DNA. *Nature Methods*, 2013. ISSN 1548-7091. doi: 10.1038/nmeth.2599.

Samuel T. Hess, Girirajan, Thanu P K, and Michael D. Mason. Ultra-high resolution imaging by fluorescence photoactivation localization microscopy. *Biophysical Journal*, 91(11):4258–4272, 2006. ISSN 0006-3495. doi: 10.1529/biophysj.106.091116.

Michael Hofmann, Christian Eggeling, Stefan Jakobs, and Stefan W. Hell. Breaking the diffraction barrier in fluorescence microscopy at low light intensities by using reversibly photoswitchable proteins. *Proceedings of the National Academy of Sciences of the United States of America*, 102(49): 17565–17569, 2005. ISSN 1091-6490. doi: 10.1073/pnas.0506010102.

Robert Hooke. *Micrographia, or some physiological descriptions of minute bodies made by magnifying glasses, with observations and inquiries thereupon. By R. Hooke*. Printed by Jo. Martyn, London, 1665.

Jun-Ichi Hotta, Eduard Fron, Peter Dedecker, Janssen, Kris P F, Chen Li, Klaus Müllen, Benjamin Harke, Johanna Bückers, Stefan W. Hell, and Johan Hofkens. Spectroscopic rationale for efficient stimulated-emission depletion microscopy fluorophores. *Journal of the American Chemical Society*, 132(14):5021–5023, 2010. ISSN 1520-5126. doi: 10.1021/ja100079w.

Bo Huang, Mark Bates, and Xiaowei Zhuang. Super-resolution fluorescence microscopy. *Annual Review of Biochemistry*, 78:993–1016, 2009. ISSN 1545-4509. doi: 10.1146/annurev.biochem.77.061906.092014.

Jatta Huotari and Ari Helenius. Endosome maturation. *The EMBO Journal*, 30(17):3481–3500, 2011. ISSN 1460-2075. doi: 10.1038/emboj.2011.286.

ImageJ Documentation Wiki. Particle_in_Cell-3D, 2013. URL `http://imagejdocu.tudor.lu/doku.php?id=macro:particle_in_cell-3d`.

Nickels A. Jensen, Johann G. Danzl, Katrin I. Willig, Flavie Lavoie-Cardinal, Tanja Brakemann, Stefan W. Hell, and Stefan Jakobs. Coordinate-targeted and coordinate-stochastic super-resolution microscopy with the reversibly switchable fluorescent protein dreiklang. *ChemPhysChem : a European Journal of Chemical Physics and Physical Chemistry*, 15(4):756–762, 2014. ISSN 1439-7641. doi: 10.1002/cphc.201301034.

Robert Kasper, Benjamin Harke, Carsten Forthmann, Philip Tinnefeld, Stefan W. Hell, and Markus Sauer. Single-molecule STED microscopy with photostable organic fluorophores. *Small*, 6(13):1379–1384, 2010. ISSN 1613-6829. doi: 10.1002/smll.201000203.

T. A. Klar, S. Jakobs, M. Dyba, A. Egner, and S. W. Hell. Fluorescence microscopy with diffraction resolution barrier broken by stimulated emission. *Proceedings of the National Academy of Sciences of the United States of America*, 97(15):8206–8210, 2000. ISSN 1091-6490.

T. A. Klar, E. Engel, and S. W. Hell. Breaking Abbe's diffraction resolution limit in fluorescence microscopy with stimulated emission depletion beams of various shapes. *Physical Review. E, Statistical, Nonlinear, and Soft Matter Physics*, 64(6 Pt 2):066613, 2001. ISSN 1539-3755.

Thomas A. Klar and Stefan W. Hell. Subdiffraction resolution in far-field fluorescence microscopy. *Optics Letters*, 24(14):954, 1999. ISSN 0146-9592. doi: 10.1364/OL.24.000954.

M. Knoll and E. Ruska. Das Elektronenmikroskop. *Z. Physik (Zeitschrift für Physik)*, 78(5-6):318–339, 1932. doi: 10.1007/BF01342199.

Graham Knott and Christel Genoud. Is EM dead? *Journal of Cell Science*, 126(Pt 20):4545–4552, 2013. ISSN 1477-9137. doi: 10.1242/jcs.124123.

Harald F. Krug and Peter Wick. Nanotoxicology: an interdisciplinary challenge. *Angewandte Chemie (International ed. in English)*, 50(6):1260–1278, 2011. ISSN 1521-3773. doi: 10.1002/anie.201001037.

Ulrich Kubitscheck. *Fluorescence Microscopy: From principles to biological applications*. Wiley, Weinheim, 2013. ISBN 1299464653.

Joseph R. Lakowicz. *Principles of Fluorescence Spectroscopy*. Springer ebook Collection / Chemistry and Materials Science 2005-2008. Springer Science+Business Media, LLC, Boston, MA, third edition edition, 2006. ISBN 0387463127.

Marcel A. Lauterbach. Finding, defining and breaking the diffraction barrier in microscopy – a historical perspective. *Optical Nanoscopy*, 1(1):8, 2012. ISSN 2192-2853. doi: 10.1186/2192-2853-1-8.

Flavie Lavoie-Cardinal, Nickels A. Jensen, Volker Westphal, Andre C. Stiel, Andriy Chmyrov, Jakob Bierwagen, Ilaria Testa, Stefan Jakobs, and Stefan W. Hell. Two-color RESOLFT nanoscopy with green and red fluorescent photochromic proteins. *ChemPhysChem : a European Journal of Chemical Physics and Physical Chemistry*, 15(4):655–663, 2014. ISSN 1439-7641. doi: 10.1002/cphc.201301016.

Jaesang Lee, Shaily Mahendra, and Alvarez, Pedro J J. Nanomaterials in the construction industry: a review of their applications and environmental health and safety considerations. *ACS Nano*, 4(7):3580–3590, 2010. ISSN 1936-086X. doi: 10.1021/nn100866w.

Leica Microsystems CMS GmbH. Dual Color STED Imaging. (37), 2011. URL `http://www.leica-microsystems.com/fileadmin/downloads/Leica\%20TCS%20STED/Application%20Notes/2C_STED_Imaging-AppLetter.EN.pdf`.

Marcel Leutenegger, Christian Eggeling, and Stefan W. Hell. Analytical description of STED microscopy performance. *Optics Express*, 18(25): 26417–26429, 2010. ISSN 1094-4087.

Roderick YH Lim and Birthe Fahrenkrog. The nuclear pore complex up close. *Current Opinion in Cell Biology*, 18(3):342–347, 2006. ISSN 0955-0674. doi: 10.1016/j.ceb.2006.03.006.

Anna Löschberger, van de Linde, Sebastian, Marie-Christine Dabauvalle, Bernd Rieger, Mike Heilemann, Georg Krohne, and Markus Sauer. Super-resolution imaging visualizes the eightfold symmetry of gp210 proteins around the nuclear pore complex and resolves the central channel with nanometer resolution. *Journal of Cell Science*, 125(Pt 3):570–575, 2012. ISSN 1477-9137. doi: 10.1242/jcs.098822.

Fang Lu, Si-Han Wu, Yann Hung, and Chung-Yuan Mou. Size effect on cell uptake in well-suspended, uniform mesoporous silica nanoparticles. *Small*, 5(12):1408–1413, 2009. ISSN 1613-6829. doi: 10.1002/smll.200900005.

Rafal Luchowski, Evgenia G. Matveeva, Ignacy Gryczynski, Ewald A. Terpetschnig, Leonid Patsenker, Gabor Laczko, Julian Borejdo, and Zygmunt Gryczynski. Single molecule studies of multiple-fluorophore labeled antibodies. Effect of homo-FRET on the number of photons available before photobleaching. *Current Pharmaceutical Biotechnology*, 9(5):411–420, 2008. ISSN 1873-4316.

James R. Mansfield, Kirk W. Gossage, Clifford C. Hoyt, and Richard M. Levenson. Autofluorescence removal, multiplexing, and automated analysis methods for in-vivo fluorescence imaging. *Journal of Biomedical Optics*, 10(4):41207, 2005. ISSN 1083-3668. doi: 10.1117/1.2032458.

Marvin Lee Minsky. Microscopy Apparatus, 1961.

Barry R. Masters. *The Development of Fluorescence Microscopy*. John Wiley & Sons, Ltd, Chichester, UK, 2001. ISBN 0470016175. doi: 10.1002/9780470015902.a0022093.

Lars Meyer, Dominik Wildanger, Rebecca Medda, Annedore Punge, Silvio O. Rizzoli, Gerald Donnert, and Stefan W. Hell. Dual-color STED microscopy at 30-nm focal-plane resolution. *Small*, 4(8):1095–1100, 2008. ISSN 1613-6829. doi: 10.1002/smll.200800055.

M. Minsky. Memoir on inventing the confocal scanning microscope. *Scanning*, 10(4):128–138, 1988. ISSN 01610457. doi: 10.1002/sca.4950100403.

Jeffrey R. Moffitt, Christian Osseforth, and Jens Michaelis. Time-gating improves the spatial resolution of STED microscopy. *Optics Express*, 19 (5):4242–4254, 2011. ISSN 1094-4087.

Christian Mühlfeld, Terry M. Mayhew, Peter Gehr, and Barbara Rothen-Rutishauser. A novel quantitative method for analyzing the distributions of nanoparticles between different tissue and intracellular compartments. *Journal of Aerosol Medicine : The Official Journal of the International Society for Aerosols in Medicine*, 20(4):395–407, 2007. ISSN 0894-2684. doi: 10.1089/jam.2007.0624.

Masahiro Nagahama, Chihiro Takahashi, Kouhei Aoyanagi, Ryo Tashiro, Keiko Kobayashi, Yoshihiko Sakaguchi, Kazumi Ishidoh, and Jun Sakurai. Intracellular trafficking of Clostridium botulinum C2 toxin. *Toxicon : Official Journal of the International Society on Toxinology*, 82:76–82, 2014. ISSN 1879-3150. doi: 10.1016/j.toxicon.2014.02.009.

U. Valentin Nägerl, Katrin I. Willig, Birka Hein, Stefan W. Hell, and Tobias Bonhoeffer. Live-cell imaging of dendritic spines by STED microscopy. *Proceedings of the National Academy of Sciences of the United States of America*, 105(48):18982–18987, 2008. ISSN 1091-6490. doi: 10.1073/pnas.0810028105.

M. Nagorni and S. W. Hell. 4Pi-confocal microscopy provides three-dimensional images of the microtubule network with 100- to 150-nm resolution. *Journal of Structural Biology*, 123(3):236–247, 1998. ISSN 1047-8477. doi: 10.1006/jsbi.1998.4037.

Daniel Neumann, Johanna Bückers, Lars Kastrup, Stefan W. Hell, and Stefan Jakobs. Two-color STED microscopy reveals different degrees of colocalization between hexokinase-I and the three human VDAC isoforms. *PMC Biophysics*, 3(1):4, 2010. ISSN 1757-5036. doi: 10.1186/1757-5036-3-4.

Wan-Kyu Oh, Sojin Kim, Moonjung Choi, Chanhoi Kim, Yoon Seon Jeong, Bo-Ram Cho, Ji-Sook Hahn, and Jyongsik Jang. Cellular uptake, cytotoxicity, and innate immune response of silica-titania hollow nanoparticles based on size and surface functionality. *ACS Nano*, 4(9):5301–5313, 2010. ISSN 1936-086X. doi: 10.1021/nn100561e.

I. Ohishi, M. Iwasaki, and G. Sakaguchi. Purification and characterization of two components of botulinum C2 toxin. (30(3)):668–673, 1980.

Christian Osseforth, Jeffrey R. Moffitt, Lothar Schermelleh, and Jens Michaelis. Simultaneous dual-color 3D STED microscopy. *Optics Express*, 22(6):7028–7039, 2014. ISSN 1094-4087.

P. Raybaut and G. Nyo. Python(x,y) 2.7.5.1, 2014. URL `https://code.google.com/p/pythonxy/`.

George H. Patterson and David W. Piston. Photobleaching in Two-Photon Excitation Microscopy. *Biophysical Journal*, 78(4):2159–2162, 2000. ISSN 0006-3495. doi: 10.1016/S0006-3495(00)76762-2.

D. W. Pohl, W. Denk, and M. Lanz. Optical stethoscopy: Image recording with resolution $\lambda/20$. *Applied Physics Letters*, 44(7):651, 1984. ISSN 00036951. doi: 10.1063/1.94865.

Dale Purves, George J. Augustine, David Fritzpatrick, William C. Hall, Anthony-Samuel LaMantia, James O. McNamara, and Mark S. Williams. *Neuroscience*. Sinauer Associates, Publishers, Sunderland, Mass, 3rd ed edition, 2004. ISBN 9780878937509.

J. A. Ramos-Vara. Technical aspects of immunohistochemistry. *Veterinary Pathology*, 42(4):405–426, 2005. ISSN 0300-9858. doi: 10.1354/vp.42-4-405.

Brian R. Rankin, Robert R. Kellner, and Stefan W. Hell. Stimulated-emission-depletion microscopy with a multicolor stimulated-Raman-scattering light source. *Optics Letters*, 33(21):2491, 2008. ISSN 0146-9592. doi: 10.1364/OL.33.002491.

Rasband W.S. ImageJ, 1997-2014. URL `http://imagej.nih.gov/ij/`.

Jose Requejo-Isidro. Fluorescence nanoscopy. Methods and applications. *Journal of Chemical Biology*, 6(3):97–120, 2013. ISSN 1864-6158. doi: 10.1007/s12154-013-0096-3.

Jonas Ries, Charlotte Kaplan, Evgenia Platonova, Hadi Eghlidi, and Helge Ewers. A simple, versatile method for GFP-based super-resolution microscopy via nanobodies. *Nature Methods*, 9(6):582–584, 2012. ISSN 1548-7091. doi: 10.1038/nmeth.1991.

E. Rittweger, B. R. Rankin, V. Westphal, and S. W. Hell. Fluorescence depletion mechanisms in super-resolving STED microscopy. *Chemical Physics Letters*, 442(4-6):483–487, 2007. ISSN 00092614. doi: 10.1016/j.cplett.2007.06.017.

Eva Rittweger, Kyu Young Han, Scott E. Irvine, Christian Eggeling, and Stefan W. Hell. STED microscopy reveals crystal colour centres with nano-

metric resolution. *Nature Photonics*, 3(3):144–147, 2009. ISSN 1749-4885. doi: 10.1038/nphoton.2009.2.

Ulrich Rothbauer, Kourosh Zolghadr, Sergei Tillib, Danny Nowak, Lothar Schermelleh, Anja Gahl, Natalija Backmann, Katja Conrath, Serge Muyldermans, M. Cristina Cardoso, and Heinrich Leonhardt. Targeting and tracing antigens in live cells with fluorescent nanobodies. *Nature Methods*, 3(11):887–889, 2006. ISSN 1548-7091. doi: 10.1038/nmeth953.

M. P. Rout. The Yeast Nuclear Pore Complex: Composition, Architecture, and Transport Mechanism. *The Journal of Cell Biology*, 148(4):635–652, 2000. ISSN 00219525. doi: 10.1083/jcb.148.4.635.

Michael J. Rust, Mark Bates, and Xiaowei Zhuang. Sub-diffraction-limit imaging by stochastic optical reconstruction microscopy (STORM). *Nature Methods*, 3(10):793–795, 2006. ISSN 1548-7091. doi: 10.1038/nmeth929.

Markus Sauer. Localization microscopy coming of age: from concepts to biological impact. *Journal of Cell Science*, 126(Pt 16):3505–3513, 2013. ISSN 1477-9137. doi: 10.1242/jcs.123612.

Markus Sauer, Johan Hofkens, and J. Enderlein. *Handbook of fluorescence spectroscopy and imaging: From single molecules to ensembles*. Wiley-VCH, Weinheim, 2011. ISBN 3527633510.

Lothar Schermelleh, Peter M. Carlton, Sebastian Haase, Lin Shao, Lukman Winoto, Peter Kner, Brian Burke, M. Cristina Cardoso, David A. Agard, Gustafsson, Mats G L, Heinrich Leonhardt, and John W. Sedat. Subdiffraction multicolor imaging of the nuclear periphery with 3D structured illumination microscopy. *Science (New York, N.Y.)*, 320(5881):1332–1336, 2008. ISSN 1095-9203. doi: 10.1126/science.1156947.

Cordelia Schiene-Fischer and Chao Yu. Receptor accessory folding helper enzymes: the functional role of peptidyl prolyl cis/trans isomerases. *FEBS Letters*, 495(1-2):1–6, 2001. ISSN 00145793. doi: 10.1016/S0014-5793(01)02326-2.

Johannes Schindelin, Ignacio Arganda-Carreras, Erwin Frise, Verena Kaynig, Mark Longair, Tobias Pietzsch, Stephan Preibisch, Curtis Rueden, Stephan Saalfeld, Benjamin Schmid, Jean-Yves Tinevez, Daniel James White, Volker Hartenstein, Kevin Eliceiri, Pavel Tomancak, and Albert Cardona. Fiji: an open-source platform for biological-image analysis. *Nature Methods*, 9(7):676–682, 2012. ISSN 1548-7091. doi: 10.1038/nmeth.2019.

Roman Schmidt, Christian A. Wurm, Stefan Jakobs, Johann Engelhardt, Alexander Egner, and Stefan W. Hell. Spherical nanosized focal spot unravels the interior of cells. *Nature Methods*, 5(6):539–544, 2008. ISSN 1548-7091. doi: 10.1038/nmeth.1214.

Roman Schmidt, Christian A. Wurm, Annedore Punge, Alexander Egner, Stefan Jakobs, and Stefan W. Hell. Mitochondrial cristae revealed with focused light. *Nano Letters*, 9(6):2508–2510, 2009. ISSN 1530-6992. doi: 10.1021/nl901398t.

Susanne Schoch and Eckart D. Gundelfinger. Molecular organization of the presynaptic active zone. *Cell and Tissue Research*, 326(2):379–391, 2006. ISSN 0302-766X. doi: 10.1007/s00441-006-0244-y.

G. M. Shepherd and K. M. Harris. Three-dimensional structure and composition of CA3–CA1 axons in rat hippocampal slices: implications for presynaptic connectivity and compartmentalization. *The Journal of Neuroscience : the Official Journal of the Society for Neuroscience*, 18(20): 8300–8310, 1998. ISSN 0270-6474.

Gleb Shtengel, James A. Galbraith, Catherine G. Galbraith, Jennifer Lippincott-Schwartz, Jennifer M. Gillette, Suliana Manley, Rachid Sougrat, Clare M. Waterman, Pakorn Kanchanawong, Michael W. Davidson, Richard D. Fetter, and Harald F. Hess. Interferometric fluorescent super-resolution microscopy resolves 3D cellular ultrastructure. *Proceedings of the National Academy of Sciences of the United States of America*, 106(9):3125–3130, 2009. ISSN 1091-6490. doi: 10.1073/pnas.0813131106.

A. V. Sorokin, E. R. Kim, and L. P. Ovchinnikov. Nucleocytoplasmic transport of proteins. *Biochemistry (Moscow)*, 72(13):1439–1457, 2007. ISSN 0006-2979. doi: 10.1134/S0006297907130032.

Wendelin J. Stark. Nanoparticles in biological systems. *Angewandte Chemie (International ed. in English)*, 50(6):1242–1258, 2011. ISSN 1521-3773. doi: 10.1002/anie.200906684.

Thorsten Staudt, Marion C. Lang, Rebecca Medda, Johann Engelhardt, and Stefan W. Hell. 2,2'-thiodiethanol: a new water soluble mounting medium for high resolution optical microscopy. *Microscopy Research and Technique*, 70(1):1–9, 2007. ISSN 1097-0029. doi: 10.1002/jemt.20396.

Anthony S. Stender, Kyle Marchuk, Chang Liu, Suzanne Sander, Matthew W. Meyer, Emily A. Smith, Bhanu Neupane, Gufeng Wang, Junjie Li, Ji-Xin Cheng, Bo Huang, and Ning Fang. Single Cell Optical Imaging and Spectroscopy. *Chemical reviews*, 113(4):2469–2527, 2013. ISSN 1520-6890. doi: 10.1021/cr300336e.

Bradley G. Stiles, Darran J. Wigelsworth, Michel R. Popoff, and Holger Barth. Clostridial binary toxins: iota and C2 family portraits. *Frontiers in Cellular and Infection Microbiology*, 1:11, 2011. ISSN 2235-2988. doi: 10.3389/fcimb.2011.00011.

G. G. Stokes. On the Change of Refrangibility of Light. *Philosophical Transactions of the Royal Society of London*, 142(0):463–562, 1852. ISSN 0261-0523. doi: 10.1098/rstl.1852.0022.

J. W. Strutt. *Scientific Papers by John William Strutt, Baron Rayleigh*, volume Vol. 1, 1869-1881. Cambridge U. Press, 1899.

Hiroshi Suzuki, Tatsushi Toyooka, and Yuko Ibuki. Simple and Easy Method to Evaluate Uptake Potential of Nanoparticles in Mammalian Cells Using a Flow Cytometric Light Scatter Analysis. *Environmental Science & Technology*, 41(8):3018–3024, 2007. ISSN 0013-936X. doi: 10.1021/es0625632.

Anna Szymborska, Alex de Marco, Nathalie Daigle, Volker C. Cordes, Briggs, John A G, and Jan Ellenberg. Nuclear pore scaffold structure analyzed by super-resolution microscopy and particle averaging. *Science (New York, N.Y.)*, 341(6146):655–658, 2013. ISSN 1095-9203. doi: 10.1126/science.1240672.

Kevin T. Takasaki, Jun B. Ding, and Bernardo L. Sabatini. Live-cell superresolution imaging by pulsed STED two-photon excitation microscopy. *Biophysical Journal*, 104(4):770–777, 2013. ISSN 0006-3495. doi: 10.1016/j.bpj.2012.12.053.

Yoshikazu Tanaka, Yuka Sato, and Takashi Sasaki. Suppression of coronavirus replication by cyclophilin inhibitors. *Viruses*, 5(5):1250–1260, 2013. ISSN 1999-4915. doi: 10.3390/v5051250.

Michael A. Thompson, Matthew D. Lew, and W. E. Moerner. Extending microscopic resolution with single-molecule imaging and active control. *Annual Review of Biophysics*, 41:321–342, 2012. ISSN 1936-1238. doi: 10.1146/annurev-biophys-050511-102250.

Derek Toomre and Joerg Bewersdorf. A new wave of cellular imaging. *Annual Review of Cell and Developmental Biology*, 26:285–314, 2010. ISSN 1530-8995. doi: 10.1146/annurev-cellbio-100109-104048.

Adriano A. Torrano, Julia Blechinger, Christian Osseforth, Christian Argyo, Armin Reller, Thomas Bein, Jens Michaelis, and Christoph Bräuchle. A fast analysis method to quantify nanoparticle uptake on a single cell level. *Nanomedicine (London, England)*, 8(11):1815–1828, 2013. ISSN 1748-6963. doi: 10.2217/nnm.12.178.

Nicholas J. Turro, V. Ramamurthy, and J. C. Scaiano. *Modern Molecular Photochemistry of Organic Molecules*. University Science Books, Sausalito, Calif., 2010. ISBN 1891389254.

A.M van Oijen, J. Köhler, J. Schmidt, M. Müller, and G.J Brakenhoff. 3-Dimensional super-resolution by spectrally selective imaging. *Chemical*

Physics Letters, 292(1-2):183–187, 1998. ISSN 00092614. doi: 10.1016/S0009-2614(98)00673-3.

Giuseppe Vicidomini, Gael Moneron, Kyu Y. Han, Volker Westphal, Haisen Ta, Matthias Reuss, Johann Engelhardt, Christian Eggeling, and Stefan W. Hell. Sharper low-power STED nanoscopy by time gating. *Nature Methods*, 8(7):571–573, 2011. ISSN 1548-7091. doi: 10.1038/nmeth.1624.

Giuseppe Vicidomini, Ivan Coto Hernández, Marta d'Amora, Francesca Cella Zanacchi, Paolo Bianchini, and Alberto Diaspro. Gated CW-STED microscopy: A versatile tool for biological nanometer scale investigation. *Methods (San Diego, Calif.)*, 2013a. ISSN 1095-9130. doi: 10.1016/j.ymeth.2013.06.029.

Giuseppe Vicidomini, Andreas Schönle, Haisen Ta, Kyu Young Han, Gael Moneron, Christian Eggeling, and Stefan W. Hell. STED nanoscopy with time-gated detection: theoretical and experimental aspects. *PloS One*, 8 (1):e54421, 2013b. ISSN 1932-6203. doi: 10.1371/journal.pone.0054421.

Jan Vogelsang, Robert Kasper, Christian Steinhauer, Britta Person, Mike Heilemann, Markus Sauer, and Philip Tinnefeld. A reducing and oxidizing system minimizes photobleaching and blinking of fluorescent dyes. *Angewandte Chemie (International ed. in English)*, 47(29):5465–5469, 2008. ISSN 1521-3773. doi: 10.1002/anie.200801518.

Clarissa L. Waites, Sergio A. Leal-Ortiz, Nathan Okerlund, Hannah Dalke, Anna Fejtova, Wilko D. Altrock, Eckart D. Gundelfinger, and Craig C. Garner. Bassoon and Piccolo maintain synapse integrity by regulating protein ubiquitination and degradation. *The EMBO Journal*, 32(7):954–969, 2013. ISSN 1460-2075. doi: 10.1038/emboj.2013.27.

Volker Westphal and Stefan Hell. Nanoscale Resolution in the Focal Plane of an Optical Microscope. *Physical Review Letters*, 94(14), 2005. ISSN 0031-9007. doi: 10.1103/PhysRevLett.94.143903.

Volker Westphal, Silvio O. Rizzoli, Marcel A. Lauterbach, Dirk Kamin, Reinhard Jahn, and Stefan W. Hell. Video-rate far-field optical nanoscopy dissects synaptic vesicle movement. *Science (New York, N.Y.)*, 320(5873): 246–249, 2008. ISSN 1095-9203. doi: 10.1126/science.1154228.

Sonja M. Wiedemann, Silke N. Mildner, Clemens Bönisch, Lars Israel, Andreas Maiser, Sarah Matheisl, Tobias Straub, Rainer Merkl, Heinrich Leonhardt, Elisabeth Kremmer, Lothar Schermelleh, and Sandra B. Hake. Identification and characterization of two novel primate-specific histone H3 variants, H3.X and H3.Y. *The Journal of Cell Biology*, 190(5):777–791, 2010. ISSN 1540-8140. doi: 10.1083/jcb.201002043.

D. Wildanger, R. Medda, L. Kastrup, and S. W. Hell. A compact STED microscope providing 3D nanoscale resolution. *Journal of Microscopy*, 236 (1):35–43, 2009. ISSN 1365-2818. doi: 10.1111/j.1365-2818.2009.03188.x.

Dominik Wildanger, Eva Rittweger, Lars Kastrup, and Stefan W. Hell. STED microscopy with a supercontinuum laser source. *Optics Express*, 16(13):9614–9621, 2008. ISSN 1094-4087.

Katrin I. Willig, Benjamin Harke, Rebecca Medda, and Stefan W. Hell. STED microscopy with continuous wave beams. *Nature Methods*, 4(11): 915–918, 2007. ISSN 1548-7091. doi: 10.1038/nmeth1108.

Acknowledgements

I would like to thank Prof. Dr. Jens Michaelis for providing a friendly and exceptional scientific working atmosphere and accepting me as a PhD student in his lab. Building the STED nanoscope from the ground up and putting it to use was a dream come true.

Many thanks also go to Prof. Dr. Christof Gebhardt, Prof. Dr. Christoph Bräuchle and Prof. Dr. Don Lamb and their group members for invaluable discussions and the friendly and motivating working atmosphere due the close collaborations between our groups.

I would like to thank Prof. Dr. Holger Barth, Prof. Dr. Tobias Böckers and Prof. Dr. Heinrich Leonhardt for the exciting collaboration projects.

I am truly indebted to Dr. Jeffrey R. Moffitt for invaluable training and good times in the first months after I started my PhD. I wish you all the best for your future career in science and your family!

Thanks to Korbi and Michi for being great office members and friends. Many thanks go to Adriano Torrano, Heinrich Grabmayr, Robert Lewis, Michi Schön, Katharina Ernst, Andreas Maiser and Lothar Schermelleh for their invaluable collaborative work.

Many thanks go to Dr. Carl-Heinz Röcker and Bernhard Gruchmann of the University of Ulm for the friendly and welcoming atmosphere after our move to the Faculty of Biophysics at Uni Ulm.

Many thanks to Lars Kastrup for providing the custom-made circular phase plates for the microscope as well as the developers of the Python distribution *Python(x,y)* and the numerous Python packages such as matplotlib and sympy.

I wish to thank the Center for NanoScience Munich for the opportunity to visit the University of Illinois at Urbana-Champaign as part of the Junior Nanotech Network 2010.

Furthermore, I would like to thank all members of our group for the friendly atmosphere and excellent scientific discussions.

Last but not least I would like to thank my mom for continuously supporting my interests while putting hers aside as well as my brother for being turbo. I would like to thank my wife for always being there for me for the last 11 years as well as our little son for allowing me to work on this thesis at least at night.